Advanced Nanoscale Approaches for Electrochemical Imaging and Sensing

by

Ryan J. Balla

Bachelor of Science, The Pennsylvania State University, 2014

Submitted to the Graduate Faculty of the

Dietrich School of Arts and Sciences in partial fulfillment

of the requirements for the degree of

Doctor of Philosophy

University of Pittsburgh

2021

UNIVERSITY OF PITTSBURGH

DIETRICH SCHOOL OF ARTS AND SCIENCES

This dissertation was presented

by

Ryan J. Balla

It was defended on

February 16, 2021

and approved by

Steve G. Weber, Professor, Department of Chemistry, University of Pittsburgh

Adrian C. Michael, Professor, Department of Chemistry, University of Pittsburgh

Kevin C. Leonard, Professor, Department of Chemical & Petroleum Engineering, University of Kansas

Thesis Advisor/Dissertation Director: Shigeru Amemiya, Professor, Department of Chemistry, University of Pittsburgh

Advanced Nanoscale Approaches for Electrochemical Imaging and Sensing

Ryan J. Balla, Ph.D.

University of Pittsburgh, 2021

Electrochemical imaging and sensing are powerful techniques that enable quantitative studies of chemical reactions with high spatial and temporal resolution. Introduced in this thesis are novel approaches to advance the spatial resolution of electrochemical imaging and the time resolution of electrochemical sensing. To achieve these goals, nanometer-wide gaps are produced and controlled between two electrodes. In the first part of this thesis, a nanometer wide gap is produced between a tip nanoelectrode and a target substrate electrode in an intelligent manner to improve the spatial resolution of scanning electrochemical microscopy (SECM). Target substrates have variable redox reactivity and nanoscale topographical changes including step edges and grooves. New imaging software and algorithms are developed to separately obtain non-contact topography and reactivity images, which can not be resolved by a widely used SECM approach. The intelligent mode of SECM will be useful for imaging of non-flat substrates with heterogeneous reactivities such as the nuclear pore complexes of biological cells as medically important targets for drug delivery into the nucleus. In the second part of this thesis, a nanometer-wide gap is produced between two carbon fiber ultramicroelectrodes for fast electrochemical sensing. In the dual electrode system, an analyte is electrolyzed at one electrode voltammetrically. The product can diffuse across the nanometer wide gap during the fast scan of the generator electrode potential, thereby enabling fast temporal electrochemical detection of the analyte at low concentrations owing to the suppressed background response of the collector electrode. This is advantageous over fast scan cyclic voltammetry with a single electrode, which requires accurate background

measurement and subtraction to qualitatively determine the analyte concentration. Fast-scan cyclic voltammetry with double carbon fiber electrodes will be useful for the in-vivo detection of neurotransmitters such as dopamine at low basal concentration levels.

Table of Contents

Preface xxii

1.0 Introduction 1

1.1 References 3

2.0 Nanoscale Intelligent Imaging Based on Real-Time Analysis of Approach Curve by Scanning Electrochemical Microscopy 4

2.1 Introduction 4

2.2 Experimental Section 7

2.2.1 Chemicals and Materials 7

2.2.2 SECM Imaging 7

2.3 Results and Discussion 8

2.3.1 Simulations of Approach Curves at Step Edge 8

2.3.2 Imaging Algorithm 10

2.3.3 Line Scan of Step Edge 12

2.3.4 Characteristic Approach Curves 15

2.3.5 Non-Contact Intelligent Imaging 19

2.3.6 Imaging Time 23

2.3.7 General Applicability 25

2.4 Conclusions 26

2.5 Supporting Information 27

2.5.1 SEM of FIB-Milled Tips 27

2.5.2 Finite Element Simulation of Characteristic Approach Curves 28

2.5.3 Constant-Height Images 33

2.5.4 Approach Curves with Multistep Tip-Substrate Contact 34

2.5.5 Analytical Expressions of Approach Curves at Reactive Substrates 35

2.6 Acknowledgements 36

2.7 References 37

3.0 Simultaneous Imaging of Nanoscale Reactivity and Topography by Intelligent Scanning Electrochemical Microscopy 40

3.1 Introduction 40

3.2 Experimental 43

3.2.1 Chemicals and Materials 43

3.2.2 SECM Imaging 43

3.2.3 Characterization of Interdigitated Au Electrodes 44

3.3 Results and Discussion 45

3.3.1 Theoretical Approach Curves 45

3.3.2 Imaging Algorithm 47

3.3.3 Intelligent Line Scan Over Interdigitated Au Electrodes 49

3.3.4 Characteristic Approach Curve 52

3.3.5 Intelligent Reactivity and Topography Imaging 54

3.3.6 Tip Damage 57

3.3.7 Imaging Time 58

3.4 Conclusions 59

3.5 Supporting Information 60

3.5.1 Theorical Approach Curves 60

3.5.2 Finite Element Simulation 61

3.5.3 Prevention of Electrostatic Tip Damage 64

3.6 Acknowledgements 66

3.7 References 66

4.0 Simulation of Fast-Scan Nanogap Voltammetry at Double-Cylinder Ultramicroelectrodes 69

4.1 Introduction 69

4.2 Model 72

4.3 Results and Discussion 74

4.3.1 Scan Rates and Geometric Parameters 74

4.3.2 FSNV at Double-Cylinder UMEs with Narrow Gaps (G=0.1) 76

4.3.3 Current Distributions at Generator and Collector Electrodes with Narrow Gaps (G=0.1) 78

4.3.4 FSNV at Double-Cylinder UMEs with Wide Gaps (G=1) 82

4.3.5 Current Distributions at Generator and Collector Electrodes with Wide Gaps (G=1) 84

4.3.6 Effects of Cylinder Radius of FSNV 86

4.3.7 Comparison Between FSNV and FSCV 88

4.4 Conclusions 88

4.5 Supporting Information 90

4.5.1 Dimensionless Model 90

4.5.2 Insulation of the Solution Side of Generator Electrode 93

4.5.3 Kinetic Effects 94

4.5.4 Sensitivity of FSNV and FSCV 97

4.6 Acknowledgments 99

4.7 References 99

5.0 Nanogap-based Electrochemical Measurements at Double-Carbon-Fiber Ultramicroelectrodes 104

5.1 Introduction 104

5.2 Double-Carbon Fiber Ultramicroelectrodes 106

5.3 Results and Discussion 108

5.3.1 Ruthenium Hexamine Couple 108

5.3.2 Preliminary Dopamine Volumetric Measurement 111

5.3.3 Dopamine with Ascorbic Acid 113

5.4 Conclusions 115

5.5 Supporting Information 116

5.5.1 Chemicals 116

5.5.2 Fabrication of Double-CF UMEs 116

5.5.3 Bipotentiostat Modification 118

5.5.4 Finite Element Analysis 119

5.5.5 3D Simulation 123

5.5.6 Collection Efficiency of DA 126

5.5.7 Effect of Following Chemical Reaction on Collector Efficiency 126

5.5.8 Effect of Collector Potential on Collector Response with DA 129

5.5.9 Outer-Sphere and Inner-Sphere Electron Transfer (ET) of RuHex(NH_3)$_6^{3+}$ 130

5.6 Acknowledgements 136

5.7 References 137

List of Tables

Table 4-1 Geometric Parameters and Scan Rates for FSNV Simulation. 71

List of Figures

Figure 2-1 Scheme of SECM imaging based on real-time analysis of approach curve at an insulating substrate with step edges under a disk-shaped Pt tip with thin glass sheath. Dashed lines with arrows indicate the tip movement. Solid lines with arrows indicate diffusion of redox species, O, to the tip. 6

Figure 2-2 SEM images of (A) and (B) protrusions and (C) and (D) recessions of insulating substrate. 7

Figure 2-3 Characteristic approach curves (solid lines) simulated at various lateral tip positions over a step edge as depicted in the inset (top view) by using the same colors. The most negative approach curve (red line) was shifted laterally by the depth of step edge (2a) to obtain the approach curve of edge–edge contact (dashed line)..... 9

Figure 2-4 Flow chart of real-time analysis of approach curve. 11

Figure 2-5 The tip current during line scan based on tip approach to lower (red lines) or upper (blue lines) terraces of the substrate with step edges in 10 mM $Ru(NH_3)_6^{3+}$ and 1 M KCl. Arrows indicate characteristic approach curves shown in Figure 2-7..... 13

Figure 2-6 (A) The *z* positions of substrate determined by fitting approach curves with eq 2 (red and blue circles) and the final *z* positions of approach curves (black circles) with the corresponding tip current in part (B). 15

Figure 2-7 Experimental approach curves (circles) at (A) upper and lower terraces far from the step edge without contact, (B) lower terrace adjacent to the step edge without contact, (C) step edge in avoidable contact with the edge of tip, and (D) step edge in unavoidable contact with the edge of tip in 10 mM $Ru(NH_3)_6^{3+}$ and 1 M KCl. Each

curve is indicated by an arrow in Figure 2-5. Theoretical curves (lines) were obtained by the best fit of eq 2. Crosses are Δi_T values defined by eq 3. Insets show the last part of the experimental and theoretical approach curves. 16

Figure 2-8 11 µm x 11 µm images based on (A) topography and (B) current at a protrusion and (C) topography and (D) current at a recession on insulating substrates in 10 mM $Ru(NH_3)_6^{3+}$ and 1 M KCl. Each pixel is equivalent to 1 µm x 1 µm. The position of step edges is represented by 6 µm x 6 µm dashed boxes. The tip was scanned laterally from the left bottom corner and stepped upward after each line scan. 22

Figure 2-9 SEM images of (A) and (B) undamaged and (C) and (D) damaged Pt nanotips after SECM imaging with low and high threshold values of –0.1 and –0.5 pA/nm for Δslope, respectively. Figure 2-10 shows SEM images of these tips just after FIB milling..... 23

Figure 2-10 SEM images of Pt tips immediately after FIB milling. Their SEM images after SECM imaging are shown in the corresponding parts of Figure 2-9..... 27

Figure 2-11 Scheme for the finite element simulation of SECM diffusion problems with a disk tip positioned over an insulating substrate with an array of squared-protrusions (or recessions). 29

Figure 2-12 Characteristic approach curves (solid lines) simulated at various lateral tip positions over the corner of (A) protrusion and (B) recession as depicted in the inset (top view) by using the same colors. 31

Figure 2-13 Experimental approach curves at step edges from Figures (A) 2-7 B, (B) 2-7 C, and (C) 2-7 D fitted with simulated curves at step edges. The best fits were obtained by using a = 0.20 µm and RG = 1.6. 32

Figure 2-14 11 µm × 11 µm constant-height images at (A) a protrusion and (B) a recession on insulating substrates in 10 mM $Ru(NH_3)_6^{3+}$ and 1 M KCl. Each pixel is equivalent to 1 µm × 1 µm. The position of step edges is represented by 6 µm × 6 µm dashed boxes. The tip was scanned laterally from the left top corner and stepped downward after each line scan..... 33

Figure 2-15 Experimental approach curves (circles) with the tip–substrate contact. Curves 1 and 2 are indicated by arrows in Figure 2-16. Theoretical curves (lines) were obtained by the best fit of eq 2. Crosses are Δi_T values defined by eq 3. Insets show the last part of approach curves..... 34

Figure 2-16 Current of Pt tips damaged during SECM imaging. SEM images of damaged tips used for parts (A) and (B) are shown in Figures 2-9 C and 2-9 D, respectively. Arrows indicate approach curves with the multi-step tip–substrate contact shown in Figure 2-15..... 35

Figure 3-1 Scheme of tip approach for (A) negative, (B) positive, and (c) mixed feedback effects for intelligent SECM imaging of a gold band on a grooved glass substrate under a disk-shaped Pt nanotip with a thin glass sheath. Dashed lines with arrows indicate the tip movement. O and R are the oxidized and reduced forms of a redox mediator, respectively..... 42

Figure 3-2 (A) and (B) SEM images of Au bands embedded in a glass substrate. A Au band was milled by FIB to expose the cross-section. (C) AFM image of unmilled Au band and (D) plot of its surface profile. Bars represent the outer diameter of the SECM tip (0.66 µm) and locate its penetration depths..... 44

Figure 3-3 Characteristic approach curves (solid lines) simulated at various lateral tip positions over a Au band as depicted in the inset (top view) by using the same colors. Dotted and dashed lines represent diffusion-limited negative and positive curves, respectively. 45

Figure 3-4 Flow chart of real-time assessment of approach curve. * See text for the algorithm when the tip approaches the inert region. 49

Figure 3-5 The tip current during line scan based on tip approach to Au and glass regions in 10 mM $Ru(NH_3)_6^{3+}$ and 1 M KCl. Arrows indicate characteristic approach curves shown in Figure 3-7..... 50

Figure 3-6 (A) The final *z* positions of approach curves (black circles) and the *z* positions of substrate determined by fitting approach curves with eq S-1 or simulated approach curves (red circles). (B) The tip current at the final *z* positions of approach curves (red circles) except for x = 1.5 μm and curves 3–5 (black circles), where the tip current was calculated at d/a = 0.3 from fitted approach curves (red circles). 51

Figure 3-7 Experimental approach curves (circles) at (A) glass (blue) and Au (red) surfaces, at the insulating groove (B) far and (C) near the Au/glass boundary, and (D) the edge of the Au band in 10 mM $Ru(NH_3)_6^{3+}$ and 1 M KCl. Solid lines are simulated approach curves. Dotted and dashed lines represent diffusion-limited negative and positive approach curves. 54

Figure 3-8 Intelligent (A) reactivity and (B) topography images of a 2.8 μm-wide Au band embedded in a glass substrate in 10 mM $Ru(NH_3)_6^{3+}$ and 1 M KCl. Each pixel is equivalent to 1 μm × 1 μm. The tip was scanned laterally from the left bottom corner and stepped upward after each line scan. The cross-sections of intelligent

(C)reactivity and (D) topography images are shown in parts (A) and (B), respectively. Open and closed circles represent Au or glass surfaces and grooves, respectively. The solid line in part (C) represents the line scan of a constant-height image in part (E). 56

Figure 3-9 SEM images of Pt tips used for intelligent SECM imaging without (A) and (B) and with (C) and (D) tip–substrate contact. Tips immediately after FIB milling are shown in parts (A) and (C). The respective tips after intelligent imaging are shown in parts (B) and (D). 57

Figure 3-10 Scheme for the finite element simulation of an SECM diffusion problem with a disk tip positioned over an array of microband electrodes embedded in the insulating substrate. 62

Figure 3-11 Simulated concentration profile around a Pt tip positioned over the boundary between Au band and grooved glass. 64

Figure 3-12 Photos of (A) and (B) ultrasonic and (C) and (D) cool-mist humidifiers in a plexiglass box, where Pt tips were handled. The low humidity of 16 % in (A) and (C) increased to 70% in (B) and (D) when the humidifiers were turned on. SEM images of the tip (E) before and (F) after handled in the plexiglass box with the cool-mist humidifier. 65

Figure 3-13 Photos of (A) a metal box for tip storage and (B) dissipative fingercots for handling electrode leads. 66

Figure 4-1 (A) Orthogonal cross-section of a parallel pair of cylindrical UMEs with the identical radius and length as voltammetric generator and amperometric collector electrodes in a solution containing a redox species, O. Dotted lines separate nanogap

and solution sides of each electrode. Blue and red arrows indicate redox cycling between nanogap sides of the double-cylinder UMEs. Black arrows indicate the electrolysis of the original redox species at the solution side of the generator electrode. (B) Potentials of generator and collector electrodes, *Eg* and *Ec*, respectively, during FSNV. 71

Figure 4-2 Voltammetric responses of generator (blue) and collector (red) electrodes with narrow gaps (G = 0.1) during forward (solid) and reverse (dashed) scans of generator potential. 78

Figure 4-3 (A, C, E) Voltammetric responses at nanogap (blue and red) and solution (black and magenta) sides of generator and collector electrodes, respectively, with narrow gaps (G = 0.1) during forward (solid) and reverse (dashed) scans of generator potential. (B, D, F) Concentration profiles of the reactant, O, at the switching potential. 79

Figure 4-4 Voltammetric responses of generator (blue) and collector (red) electrodes with wide gaps (G = 1) during forward (solid) and reverse (dashed) scans of generator potential. 83

Figure 4-5 (A, C, E) Voltammetric responses at nanogap (blue and red) and solution (black and magenta) sides of generator and collector electrodes, respectively, with narrow gaps (G = 1) during forward (solid) and reverse (dashed) scans of generator potential. (B, D, F) Concentration profiles of the reactant, O, at the switching potential. 86

Figure 4-6 A model for double-cylinder electrodes with nanogaps. Boundary conditions for generator and collector electrodes are given by eqs 3 and 5, respectively. Blue and red boundaries represent nanogap and solution sides of the respective electrodes. Black

and magenta boundaries represent solution sides of the respective electrodes. Green boundaries are simulation limits. The *x*-axis is the symmetry axis. 91

Figure 4-7 (A) Short-, (B) intermediate- and (C) long-time chronoamperometric responses (dots) of the generator electrode with *G* = 100. Solid lines represent eq S-10. 92

Figure 4-8 Voltammetric responses of generator (blue) and collector (red) electrodes with narrow gaps of *G* = 0.1 with (dots) and without (lines) the insulation of the solution side of the generator electrode. 93

Figure 4-9 Voltammetric responses of generator (blue) and collector (red) electrodes with narrow gaps of *G* = 1 with (dots) and without (lines) the insulation of the solution side of the generator electrode. 94

Figure 4-10 Voltammetric responses of generator (blue) and collector (red) electrodes with narrow gaps (*G* = 0.1) with λ = (dotted) 1000, (solid) 100, and (dashed) 10. 96

Figure 4-11 Voltammetric responses of generator (blue) and collector (red) electrodes with wide gaps (*G* = 1) with λ = (solid) 100, (dotted) 10, and (dashed) 1. 97

Figure 5-1 Scheme of (A) a double-CF UME and (B) waveforms for nanogap voltammetry. E_g and E_c are potentials of generator and collector electrodes, respectively. Red dotted line in part A corresponds to the cross section shown in part C for redox cycling of the $Ru(NH_3)_6^{3+/2+}$ couple across the nanogap (red and blue arrows) as well as the reduction of $Ru(NH_3)_6^{3+}$ at the side of the generator electrode far from the nanogap (black arrows). 106

Figure 5-2 Scanning electron microscopy of (A) a double-CF UME sealed in a glass capillary and (B) a nanogap between CFs. 107

Figure 5-3 Generator (top panel) and collector (bottom panel) current responses of double-CF UMEs at (A) 2–100 and (B) 0.02–1 V/s in 10 mM $Ru(NH_3)_6^{3+}$ and 1 M KCl. Solid and dashed lines represent forward and reverse scans, respectively. Collector potential at –0.05 V. 109

Figure 5-4 Experimental (lines) and simulated (circles) current responses of generator (blue) and collector (red) electrodes in 10 mM $Ru(NH_3)_6^{3+}$ and 1 M KCl at (A) 100 and (B) 0.1 V/s. Only experimental generator responses were background-subtracted. Solid lines and closed circles represent forward scans. Dashed lines and open circles correspond to reverse scans. Simulation employed k^0 = 0.9 cm/s, formal potential of –0.185 V, diffusion coefficient of 7.0×10^{-6} cm^2/s, CF length of 51.1 µm, and gap widths of 0.15 ± 0.02 µm. 110

Figure 5-5 Generator and collector current responses of double-CF UMEs at (A) 0.1 and (B) 100 V/s in Tris buffer containing 0 (black), 50 (blue), and 100 (red and green for first and second cycles, respectively) µM DA. Collector potential at –0.3 V. 112

Figure 5-6 Generator and collector current responses of double-CF UMEs at (A) 0.1 and (B) 100 V/s in Tris buffer containing 500 µM AA with (red and green for first and second cycles, respectively) and without (blue) 100 µM DA. Black lines represent background responses in the buffer. Collector potential at –0.3 V..... 114

Figure 5-7 SEM images of double-CF UMEs with a ~0.18 µm-wide gap (A) before and (B) after FIB milling or (C) and (D) double-CF UMEs with a ~0.8 µm-wide gap. 117

Figure 5-8 Current responses of contacted generator (blue) and collector (red) electrodes in 1 M KCl at 0.02 V/s. Solid and dashed lines represent forward and reverse scans, respectively. The collector potential was set at –0.05 V..... 119

Figure 5-9 Experimental (lines) and simulated (circles) current responses of generator (blue) and collector (red) electrodes in 10 mM $Ru(NH_3)_6^{3+}$ and 1 M KCl at (A) 10 and (B) 1 V/s. Experimental generator responses are background-subtracted. (C) Generator (blue) and collector (red) responses simulated for quasi-reversible (circles) and reversible (lines) ET reactions at 100 V/s. Simulation employed parameters used in Figure 5-4 with the exception of k^0 = 10 cm/s for the reversible case. Solid lines and closed circles represent forward scans. Dashed lines and open circles correspond to reverse scans. The collector potential was set at 0.05 V. 120

Figure 5-10 (A) Generator and (B) collector responses of double-CF UMEs at 2–100 V/s in 1 M KCl. Solid and dotted lines represent forward and reverse scans, respectively. The collector potential was set at 0.05 V. 121

Figure 5-11 Simulated responses of generator (blue) and collector (red) electrodes in 10 mM $Ru(NH_3)_6^{3+}$ and 1 M KCl at 1000 V/s. Simulation employed the parameters determined in part A of Figure 5-4. Solid and dashed lines represent forward and reverse scans, respectively. 123

Figure 5- 12 3D geometry of double-CF UMEs simulated for nanogap voltammetry. The CF radius is given by r_0. 124

Figure 5-13 Generator (blue) and collector (red) responses based on 2D (circles) and 3D (lines) simulations at (A) 100 and (B) 0.1 V/s. Parameters for the respective scan rates are identical to those used in parts A and B of Figure 5-4. Solid and dashed lines are forward and reverse scans, respectively. Closed and open circles are forward and reverse responses, respectively. Black lines are responses of the corresponding single CF electrode without a collector electrode. 124

Figure 5-14 Background-subtracted generator response to 50 µM DA at 0.1 V/s as obtained from the corresponding generator voltammograms in Figure 5-5 A. The collector response is not background-subtracted and is identical to that in Figure 5-5 A. ... 126

Figure 5-15 Oxidation of DA (top) and cyclization of DOQ (bottom).[42] 128

Figure 5-16 Oxidation of AA (top) and hydration of dehydroascorbic acid (bottom).[44,45] 128

Figure 5-17 Reduction of DOQ by AA.[48] 129

Figure 5-18 Generator and collector responses of double-CF UMEs in Tris buffer containing 100 µM DA at 100 V/s when the collector potential was set at –0.3 (blue) or 0.25 V (red). Black lines are background voltammograms in Tris buffer at the collector potential of 0.25 V. 130

Figure 5-19 Outer-sphere and inner-sphere ET of the $Ru(NH_6)_3^{3+/2+}$ couple at outer and inner Helmholtz planes (OHP and IHP), respectively.[52] 131

Preface

To begin, I would like to graciously thank Professor Shigeru Amemiya for his unique ability to train the minds of ambitious researchers. My ability to understand and frame a scientific obstacle in an objective manner is an invaluable skill that I will surely use in my future career pursuits and personal endeavors.

Additionally, I would like to thank Professor Stephen Weber, Professor Adrian Michael, and Professor Kevin Leonard for challenging me to become a proficient scientific writer and for taking part in the evaluation of my progress during my graduate experience. In addition, I would like to, again, thank Professor Kevin Leonard and Dr. Dylan Jantz for their expert programming skills and insight in our scientific collaborations.

Furthermore, I would like to thank Dr. Ran Chen for training me in the meticulous practice of learning SECM and always being available to share his experience and expertise when a relevant learning opportunity presented itself. Additionally, I would like to thank all the other current and former Amemiya group members for their help and assistance: Dr. Pavithra Pathirathna, Niraja Kurapati, Dr. Jiyeon Kim, Dr. Rafael Martos Buoro, Erin Gramm, Siao-Han (Phoebe), Huang Guanqun Meng, Jacob Ross, and Zemeng Wei.

Importantly, I would like to thank Dr. Peixin He of CH Instruments Inc. for his willingness to assist in the special alterations and modifications requested pertaining to their useful software and hardware to meet our specific research needs.

I wish to thank the following individuals for their invaluable time and assistance in helping me pursue new and interesting research: Tom Gasmire, Jeff Tomaszewski, Jeff Sicher, and Shawn

Artman (Machine Shop), Lori Neu (Glass Shop), David Emala, James McNerney, Dr. Lin Yao and Charles Fleishaker (Electronics Shop), Dr. Susheng Tan, Dr. Daniel Lamont, Dr. Jun Chen, and Mike McDonald (Nanoscale Fabrication and Characterization Facility).

Lastly, I would like to thank my wife, Chelsea Balla, for her patience and support through this trying experience. Her sacrifices will be forever appreciated and remembered. I would also like to thank my mother, Melinda Balla, who always had time to proof my various documents no matter the complexity of the content. Finally, I would like to thank my father, Glenn Balla, and brother, Parker Balla, and the crew. Without them, none of this would be possible.

1.0 Introduction

Electrochemical imaging and sensing are powerful ways to study chemical reactions with high spatial and temporal resolution. For instance, nanoscale scanning electrochemical microscopy employs nanometer-sized electrodes as amperometric sensors to image the reactivity of single nanostructures such as molecular transport through single nanopores and electrocatalysis at single nanoparticles. Moreover, ultrafast voltammetry utilizes ultramicroelectrodes to enable electrochemical sensing with time resolutions from microsecond for in-vivo neuroanalysis to nanoseconds for fundamental electrochemical research. Purposed in this thesis are new approaches to control nanoscale distances between two electrodes and, subsequently, maximize the spatial resolution of electrochemical imaging and the time resolution of electrochemical sensing.

The second chapter of this thesis develops the intelligent mode of nanoscale SECM as a new methodology to electrochemically image the topography of non-flat inert substrates.[1] Novel software is developed to precisely control a short distance of the nanometer-sized probe tip from the substrate by using a conventional SECM setup, thereby improving the spatial resolution that is determined by the tip size and the tip–substrate distance. This new approach allows not only the topography imaging of 500 nm-height step edges of protrusions and recessions but also the confirmation of no redox reactivity of the glass substrate surface. Such an abrupt change in the topography can not be imaged by other modes of SECM, where the topography and reactivity of the substrate are convoluted or the substrate must be relatively flat or uniformly reactive.

The third chapter of this thesis further develops the intelligent mode to separately image the reactivity and topography of heterogeneously reactive, non-flat substrates. This new capability of nanoscale SECM imaging is highly significant because variable chemical compositions and

topographies of substrate materials are intrinsically connected with their applications. Experimentally, this unprecedented capability is demonstrated by studying an array of gold bands coated on the glass surface. The resultant reactivity images display the contrast between the reactive gold sites and the insulating glass sites. Additionally, topography images reveal nanoscale groove defects made at the compositional material boundary.

The second half of this thesis is built upon my finding that a nanometer-wide gap can be formed between two carbon fibers sealed in a glass capillary. Significantly, this finding lead to the development of double carbon fiber ultramicroelectrodes with a nanogap for fast scan cyclic voltammetry (FSCV) to quantitatively study fast electron kinetics or detect neurotransmitters without the need for background subtraction. In the fourth chapter, double carbon fiber electrodes are modelled and simulated by the finite element method to predict that the fast voltammetric production of a redox species at one carbon fiber electrode and the amperometric collection of the product at the other electrode are feasible when the electrodes are separated by a nanometer-sized gap.[2] The simulation study from the fourth chapter is followed by the electrochemical study of dual carbon fiber ultramicroelectrodes in the final chapter of this thesis.[3] Experimentally, dual carbon fiber electrodes are prepared reproducibly by employing focus ion beam technology to establish experimental methodology for nanogap-mediated redox cycling during FSCV. The efficient redox cycling of the $Ru(NH_3)_6^{3+/2+}$ couple across ~200 nm-wide gap yields an amperometric collector response with ~100 times lower background in comparison with the voltammetric generator response at 100 V/s. The selective detection of dopamine in the presence of ascorbic acid as a major in-vivo interferent is demonstrated.

1.1 References

(1) Balla, R. J.; Jantz, D. T.; Kurapati, N.; Chen, R.; Leonard, K. C. and Amemiya, S. *Anal. Chem.* **2019**, 91, 10227-10235.

(2) Pathirathna, P.; Balla, R. J. and Amemiya, S. *J. Electrochem. Soc.* **2018**, 165, G3026–G3032.

(3) Pathirathna, P.; Balla, R. J. and Amemiya S. *Anal. Chem.* **2018**, 90, 11746–11750.

2.0 Nanoscale Intelligent Imaging Based on Real-Time Analysis of Approach Curve by Scanning Electrochemical Microscopy

This thesis author fabricated electrodes, collaborated with programmers to create novel software to address long-standing SECM problems, utilized COMSOL simulation and collected and analyzed experimental data. D. Jantz did all software coding in LabView.

2.1 Introduction

Accurate control of short distance between a tip and a substrate is crucial for high-resolution and non-contact imaging by scanning electrochemical microscopy[1-3] (SECM). The tip–substrate distance, d, limits the spatial resolution of SECM as represented by[4]

$$h^{\infty} = 1.5d + a \quad (1)$$

where h^{∞} is the radius of local substrate surface seen in the feedback mode and a is the radius of disk-shaped tip. It, however, is challenging to maintain short distances of $<a$ over non-flat substrates without the tip–substrate contact by using standard instrumentation[5] equipped with a tip positioner and a potentiostat.[6] This setup dominantly employs the constant-height imaging mode,[5] where a tip is scanned laterally at a fixed height to lose a feedback effect from a recession of

substrate or crash the tip into a protrusion.[7] The standard setup is also operated in the constant-current imaging mode, which is straightforward only when the substrate is relatively flat and uniformly reactive.[8] Alternatively, SECM is combined with other techniques, e.g., atomic force microscopy, to determine the tip–substrate distance by the second method.[9] Combined SECM techniques, however, are not widely adopted,[10] because sophisticated hardware and complicated multifunctional probes are required.

The tip–substrate distance can be determined accurately from the strong distance-dependence of tip current[11] as represented by SECM approach curves.[4] Approach curves were measured at different lateral tip positions and analyzed only afterward to deconvolute the topography and reactivity of substrate.[10,12,13] The depth scan mode,[12,14] however, obtains approach curves by repeatedly imaging a substrate at different tip heights, thereby resulting in the same limitations as the constant-height mode. The intermittent contact mode[10] requires the simultaneous measurement of shear force between a tip and a substrate to terminate tip approach upon contact, which can damage the substrate[15] to artificially alter its topography and reactivity. The hopping mode was implemented into standard instrumentation with nanometer-sized tips to image biological cells[16] and glass-supported platinum microbands.[13] Non-contact imaging of these non-flat substrates terminated the tip approach when the tip current, i_T, decreased to only ~95% of that in the bulk solution, $i_{T,\infty}$. The resultant long tip–substrate distance of ~5a at insulating substrates[17] largely compromises the spatial resolution.

Herein, we propose a new imaging mode of SECM based on real-time analysis of approach curve to actively control nanoscale tip–substrate distances without contact. In contrast to combined SECM techniques,[9] this imaging mode employs standard instrumentation equipped with a disk-shaped nanotip[18,19] and controlled by the advanced version of Labview-based software,[20,21] which

measures and analyzes the tip current after each step of tip approach to substrate. The power of this software-based method is demonstrated by high-resolution and non-contact imaging of an insulating substrate with step edges (Figure 2-1). Specifically, short distances of $\leq 0.3a$ are achieved without contact when a glass-sealed Pt nanotip approaches not only flat terraces (Figures 2-1 A and 2-1 B) to yield a good fit between experimental and theoretical approach curves, but also step edges (Figure 2-1 C), which are located by a deviation of the tip current from the theory as explained by the post-imaging analysis of the approach curve. The thin glass sheath with a small outer radius, rg, rarely contacts the step edge (Figure 2-1 D), which is unavoidable and instantaneously detected as an abrupt change in the slope of approach curve to prevent the damage of the fragile nanotip. The general applicability of this imaging mode to substrates with various topography and reactivity is also discussed.

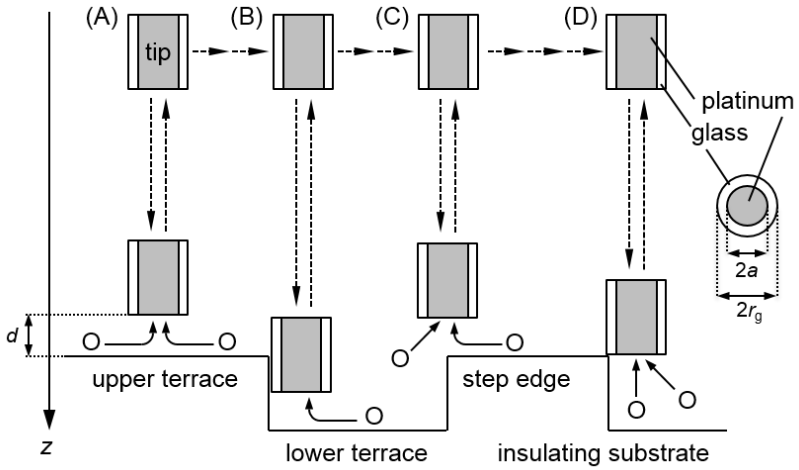

Figure 2-1 Scheme of SECM imaging based on real-time analysis of approach curve at an insulating substrate with step edges under a disk-shaped Pt tip with thin glass sheath. Dashed lines with arrows indicate the tip movement. Solid lines with arrows indicate diffusion of redox species, O, to the tip.

2.2 Experimental Section

2.2.1 Chemicals and Materials

$Ru(NH_3)_6Cl_3$ was obtained from Strem Chemicals (Newburyport, MA). KCl (≥99%) was purchased from Sigma Aldrich (Milwaukee, WI). Insulating SiO_2/Si substrates with step edges (HS-500MG-UM) were obtained from Ted Pella (Redding, CA) and characterized by SEM (Figure 2-2). A Milli-Q Advantage A10 system combined with Elix 3 Advantage (EMD Millipore, Billerica, MA) purified tap water to obtain the resistivity of 18.2 MΩ·cm and the total organic carbon of 2–3 ppb.[22]

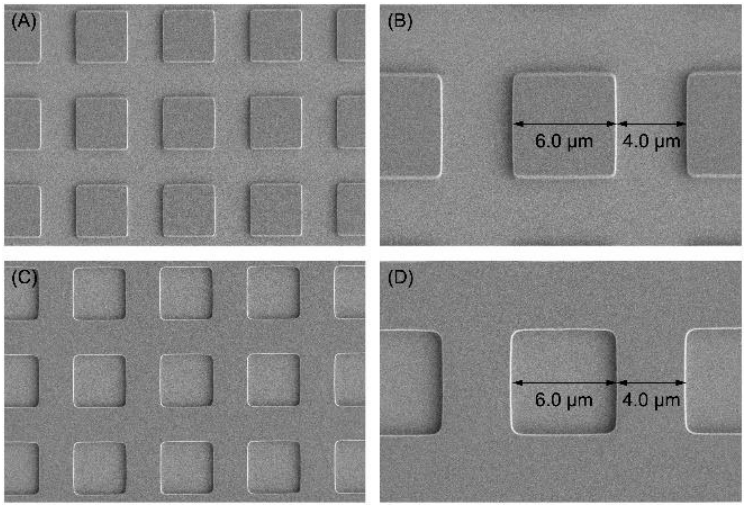

Figure 2-2 SEM images of (A) and (B) protrusions and (C) and (D) recessions of insulating substrate.

2.2.2 SECM Imaging

A home-built SECM instrument[21] was equipped with a potentiostat (CHI 802D, CH Instruments, Austin TX) and controlled by using the Labview program based on a custom fuzzy logic algorithm[20] (National Instruments, Austin, TX). An SECM stage was accommodated in a

faraday cage equipped with metallic heat sinks and surrounded by polystyrene foams[21] to maintain stable temperature and, subsequently, minimize thermal drift.[23] Pt tips with inner and outer radii of ~0.25 and ~0.4 μm, respectively, were fabricated by laser-assisted pulling, heat annealing, and focused-ion-beam (FIB) milling[24,25] and characterized by scanning electron microscopy (SEM; Figure 2-10). The tips were protected from electrostatic discharge[26] under sufficiently high humidity (>30%)[27] as well as from electrochemical damage by using the cell-on-between-run function of the modified potentiostat.[28] Pt wires served as counter and quasi-reference electrodes. The tip potential was set to obtain the steady-state current based on the diffusion-limited reduction of 10 mM $Ru(NH_3)_6^{3+}$ in 1 M KCl.

2.3 Results and Discussion

2.3.1 Simulations of Approach Curves at Step Edge

The development of imaging algorithm (see below) was facilitated by finite element simulation of approach curves at step edges of insulating substrate. Interestingly, simulated approach curves are unique and different from those simulated and observed experimentally at flat substrates that were vertical or slightly tilted against a tip.[29-31] Finite element simulation was performed by solving a 3D diffusion problem with a disk-shaped SECM tip with RG = 1.5 (= r_g/a) approaching a step edge with a height of tip diameter, 2a (Figure 2-11).

Figure 2-3 shows characteristic approach curves simulated at the step edge of insulating substrate. When a tip approaches to the upper terrace far from the step edge (Figure 2-1 A), the theoretical current based on the negative feedback effect, i_T^{NF} , is given by[17]

$$\frac{i_T^{NF}}{i_{T,\infty}} = \frac{\frac{2.08}{RG^{0.358}}\left(L - \frac{0.145}{RG}\right) + 1.585}{\frac{2.08}{RG^{0.358}}(L + 0.0023RG) + 1.57 + \frac{\ln RG}{L} + \frac{2}{\pi RG}\ln\left(1 + \frac{\pi RG}{2L}\right)} \quad (2)$$

where $L = d/a$. A higher tip current is expected when a larger part of Pt tip is positioned over the lower terrace (magenta, orange, and blue lines in Figure 2-3) until the edge of tip barely contacts the step edge (dashed line). Higher tip currents are attributed to less hindered diffusion of redox species from the solution above the lower terrace to the tip (Figures 2-1 C and 2-1 D). By contrast, the tip current is lower than eq 2 when the edge of tip just passes the step edge to approach the lower terrace (red line in Figure 2-3). The tip current is lowered by a negative feedback effect from the wall of step edge (Figure 2-1 B), which hinders the diffusion of redox species to the tip. The additional negative feedback effect becomes smaller over the lower terrace further from the step edge to eventually follow eq 2.

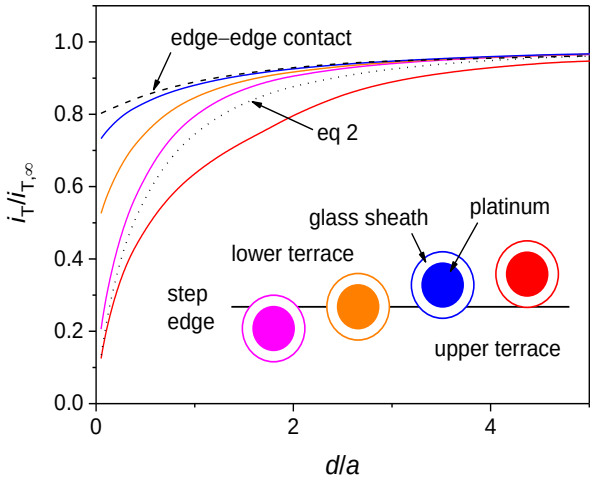

Figure 2-3 Characteristic approach curves (solid lines) simulated at various lateral tip positions over a step edge as depicted in the inset (top view) by using the same colors. The most negative approach curve (red line) was shifted laterally by the depth of step edge (2a) to obtain the approach curve of edge–edge contact (dashed line).

2.3.2 Imaging Algorithm

We implemented a new algorithm into Labview software[20,21] (Figure 2-4) to enable SECM imaging based on real-time analysis of approach curve. This algorithm aims at vertically bringing the tip to the proximity of a substrate to achieve high spatial resolution without tip–substrate contact. The current version of the software targets insulating substrates by employing eq 2 but will be applicable to reactive substrates by employing the corresponding equations as discussed later. Specifically, the stepwise tip approach to substrate is followed by the measurement of steady-state tip current. When the tip–substrate distance is short enough to yield $i_T < 0.90\ i_{T,\infty}$, the occurrence of tip–substrate contact is judged from a change in the slope of approach curve as detailed below. Without contact, the measured current is compared with a theoretical value predicted by eq 2, which is fitted to all previous data points by adjusting $i_{T,\infty}$ and z tip position at $L = 0$ using the Virtual Instrument of Labview for nonlinear curve fit. A difference between experimental and theoretical currents, Δi_T, is defined as

$$\Delta i_T = i_T - i_T^{NF} \quad (3)$$

When Δi_T exceeds a preset value, the tip approach is terminated to achieve the shortest non-contact distance, e.g., at step edges (Figure 2-1 C). Otherwise, the tip current is compared with a preset threshold value of $0.4 i_{T,\infty}$, which corresponds to $d = 0.3a$ with $RG = 1.5$ in eq 2. The threshold current is reached when the tip approaches an upper terrace far from the step edge (Figure 2-1 A) or a lower terrace (Figure 2-1 B). In these cases, the entire approach curve is fitted with eq 2 to determine the z tip position at $L = 0$ as the vertical position of substrate for topography imaging. If the tip current is still higher than the threshold value, the fuzzy logic algorithm of Labview[20] is used to move the tip closer to the substrate with a smaller step than the last step. This fuzzy logic

algorithm employs a non-Boolean control system that uses input variables (e.g., tip size, enhancement factor, and distance from target setpoint) to continuously change the step size of the approach smoothly, and automatically stop the tip at a given setpoint. A smaller step at a shorter tip–substrate distance not only records the steeper part of approach curve accurately, but also minimizes the damage of tip[32] and substrate[15] upon their contact.

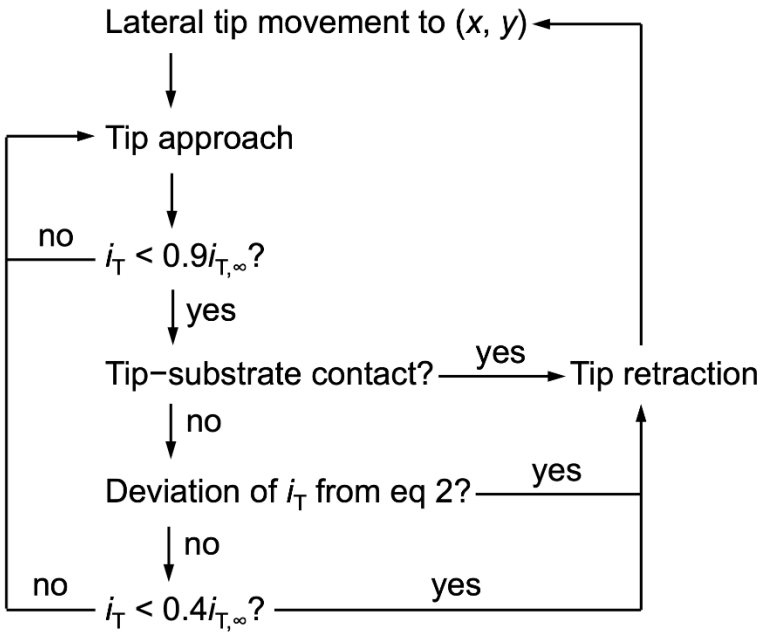

Figure 2-4 Flow chart of real-time analysis of approach curve.

Our algorithm evaluates a change in the slope of approach curve, Δslope, to detect the tip–substrate contact. Negative approach curves at an insulating substrate (Figure 2-3) become monotonically steeper at a shorter tip–substrate distance. By contrast, the slope of approach curve becomes smaller when the tip–substrate contact occurs to limit a change in the tip current, thereby yielding

$$\Delta\text{slope} = \left|\Delta i_{\text{n}}\right| / \Delta z_{\text{n}} - \left|\Delta i_{\text{n-1}}\right| / \Delta z_{\text{n-1}} < 0 \quad (4)$$

where Δi_n and Δz_n are changes in tip current and vertical tip position, respectively, after the *n*th step of tip approach. The tip–substrate contact results in Δslope more negative than an empirically preset value, which is not zero, because of the noise of tip current.

2.3.3 Line Scan of Step Edge

We tested the algorithm based on real-time analysis of approach curve by performing line scan over step edges. In this test, the entire profile of approach curves at step edges was obtained by bringing a tip to a substrate until the tip–substrate contact occurred at Δslope < –.1 pA/nm (see eq 4), thereby yielding detailed information about differences between experimental and theoretical currents, Δi_T (eq 3), as assessed below. Specifically, a 400 nm-diameter Pt tip with *RG* = 1.6 was used to obtain approach curves with a lateral interval of 100 nm over three edges of 500 nm-deep square-shaped recessions with a length of 6 μm and an interval of 4 μm as determined by SEM (Figure 2-2). The tip current was based on the diffusion-limited reduction of 10 mM $Ru(NH_3)_6^{3+}$, where $i_{T,\infty}$ is given by

$$i_{T,\infty} = 4xnFDc_0a \quad (5)$$

where *x* is a function of RG^{33}, *n* (= 1) is the number of transferred electrons, and *D* (= 7.8 x 10^{-6} cm^2/s) and c_0 are its diffusion coefficient and concentration of $Ru(NH_3)_6^{3+,}$ respectively. $Ru(NH_3)_6^{3+}$ yields a stable $i_{T,\infty}$ value to enable the quantitative analysis of approach curves, where non-ideal tip behaviors must be prevented, e.g., as demonstrated by programming the tip potential for O_2.[34]

Figure 2-5 shows the time profile of the tip current during the measurement of 151 approach curves at different lateral tip positions over three step edges. The tip initially approached

the lower terrace, where the tip current went below a threshold value of $0.40i_{T,\infty}$ (red line). The tip was closest to the step edge (Figure 2-1 B) when the last approach curve in red was obtained. The next approach curve (blue line) was obtained when the glass sheath of a tip approached the edge (Figure 2-1 D), where the tip current decreased only to ~80% of $i_{T,\infty}$ upon the tip–substrate contact as predicted theoretically (e.g., blue line in Figure 2-3). The next four approach curves also failed to reach a threshold current of $0.40i_{T,\infty}$, where a part of the tip approached to the edge (Figure 2-1 C) to yield higher tip currents even at $L = 0$ as predicted theoretically (e.g., orange line in Figure 2-3). Eventually, the threshold tip current was obtained to terminate the tip approach at the next lateral position, where the entire tip approached the upper terrace of the substrate (Figure 2-1 A). Two other edges also gave similar characteristic approach curves.

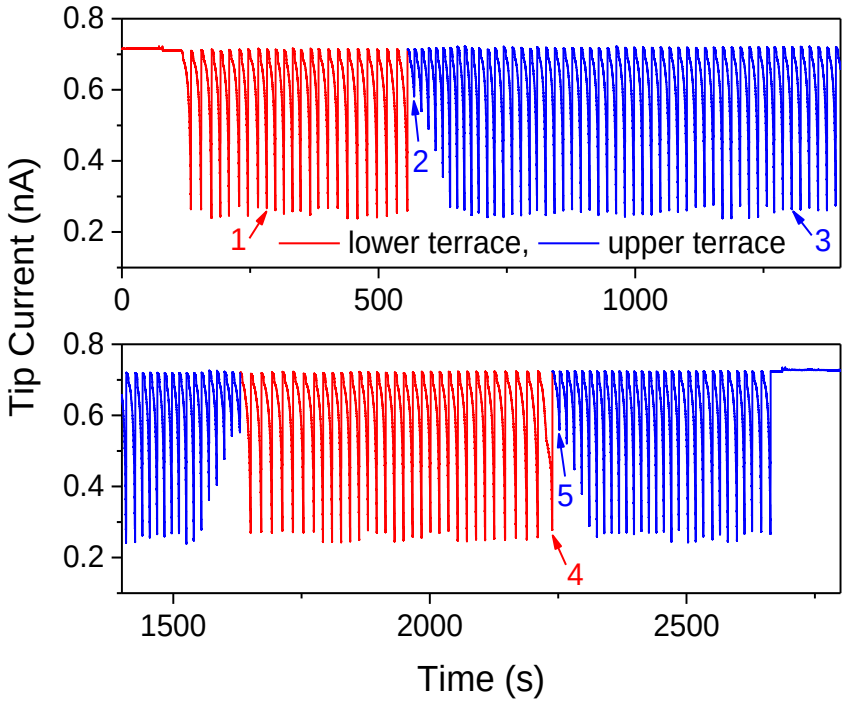

Figure 2-5 The tip current during line scan based on tip approach to lower (red lines) or upper (blue lines) terraces of the substrate with step edges in 10 mM $Ru(NH_3)_6^{3+}$ and 1 M KCl. Arrows indicate characteristic approach curves shown in Figure 2-7.

The line-scan experiment quantitatively revealed the topography of substrate including the location of step edges. Specifically, each approach curve was fitted with eq 2 to yield a z tip position at $L = 0$ (red and blue circles in Figure 2-6 A). This tip position corresponded to the actual position of the substrate surface when the tip current went below the threshold (Figure 2-6 B). The resultant profile represents the height of step edges (500 nm) and traces the tilt of the substrate. The gradual change of substrate position is not due to the thermal drift of initial vertical tip position,[21,23] which was minimized by an isothermal chamber.[21,23] Importantly, the vertical tip position at the last point of approach curve (black circles in Figure 2-6 A) was only ~50 nm away from terraces of the substrate. By contrast, the z tip position at $L = 0$ is not equivalent to the position of the substrate near step edges, where experimental approach curves did not fit well with eq 2 (see below). The tip current at the last point of each approach curve was much higher than the threshold value of $0.40i_{T,\infty}$ when the tip approached step edges (Figure 2-6 B). Nevertheless, we were able to accurately locate step edges (dotted lines in Figure 2-6), which were separated by ~r_g (= ~400 nm) from the lateral tip position when the tip approached the lower terrace to barely pass the step edge (Figure 2-1 B). The separation between step edges corresponds to 6.0 and 3.9 μm in the line scan (Figure 2-6) as expected from length and separation of recession (6.0 and 4.0 μm, respectively, in Figure 2-2).

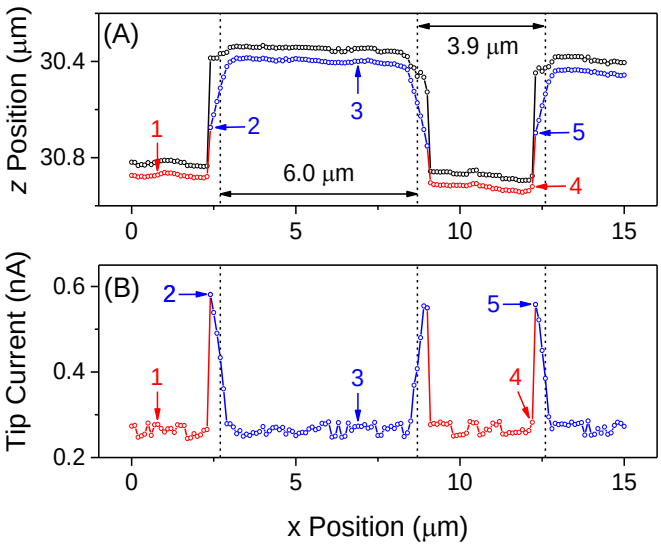

Figure 2-6 (A) The *z* positions of substrate determined by fitting approach curves with eq 2 (red and blue circles) and the final *z* positions of approach curves (black circles) with the corresponding tip current in part (B).

2.3.4 Characteristic Approach Curves

Here, we use characteristic approach curves from the line scan experiment (Figure 2-5) to assess differences between experimental and theoretical tip currents, Δi_T (eq 3), at various lateral tip positions. Specifically, Figure 2-7 shows characteristic experimental approach curves (circles) and best-fitted theoretical curves (lines) in addition to Δi_T values determined at each vertical tip position when $i_T < 0.90 i_{T,\infty}$. The line scan experiment employed a large threshold value for Δi_T of 10 nA, which was never exceeded. Accordingly, approach curves were measured until the tip–substrate contact occurred or when the tip current went below a threshold value.

The tip current followed eq 2 to go below a preset threshold of $0.40 i_{T,\infty}$ at lower and upper terraces far from the edge (red and blue lines, respectively, in Figure 2-7 A). The resultant Δi_T

values (crosses in Figure 2-7 A) were very small and ranged between ±3 pA (i.e., ±0.4% of $i_{T,\infty}$), which is attributed to the noise of tip current. The theoretical curves were fitted best by adjusting z positions at L = 0 to 30.876 and 30.399 μm for lower and upper terraces, respectively. The difference of z positions (477 nm) is close to but is slightly smaller than the height of step edge (500 nm), which is attributed to the tilt of substrate (Figure 2-6 A). The lateral positions of these two approach curves are separated by 6 μm to yield a tilt angle of 2.2° from the height difference of 23 nm.

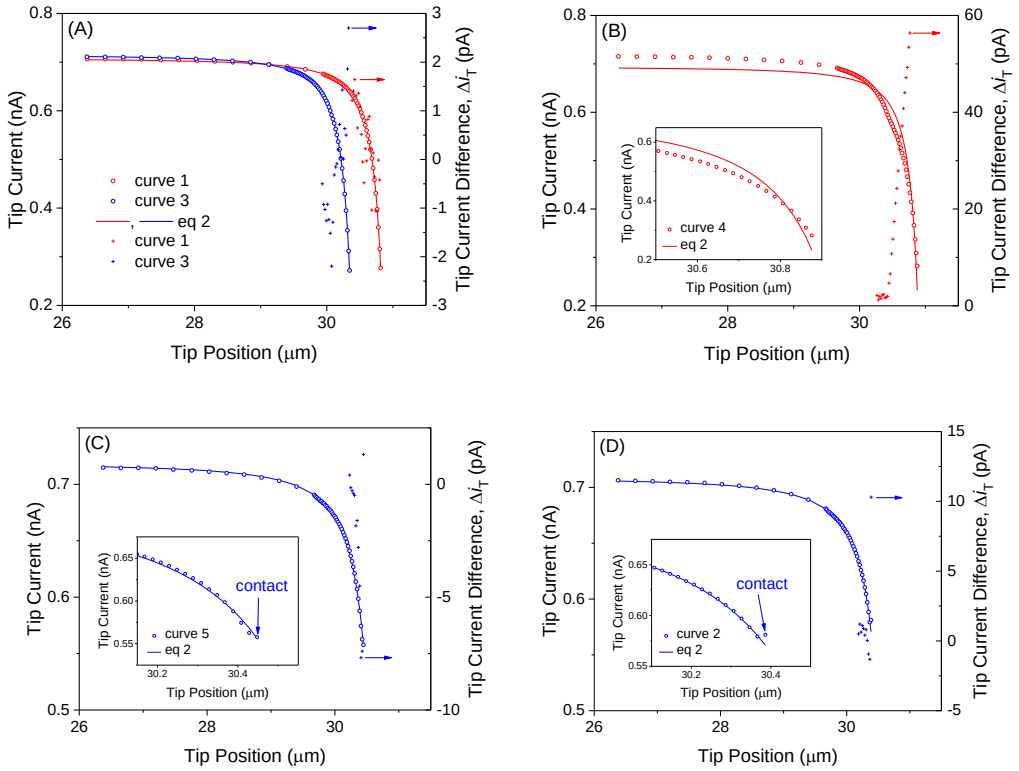

Figure 2-7 Experimental approach curves (circles) at (A) upper and lower terraces far from the step edge without contact, (B) lower terrace adjacent to the step edge without contact, (C) step edge in avoidable contact with the edge of tip, and (D) step edge in unavoidable contact with the edge of tip in 10 mM $Ru(NH_3)_6^{3+}$ and 1 M KCl. Each curve is indicated by an arrow in Figure 2-5. Theoretical curves (lines) were obtained by the best fit of eq 2. Crosses are Δi_T values defined by eq 3. Insets show the last part of the experimental and theoretical approach curves.

Figure 2-7 B shows a characteristic approach curve at the lower terrace adjacent to the step edge (Figure 2-1 B), which importantly features large positive Δi_T values. As expected from simulation (red line in Figure 2-3), the experimental approach curve showed a "dip" when the tip was positioned below the upper terrace, where the diffusional access of $Ru(NH_3)_6^{3+}$ to the Pt tip was partially hindered by the wall of step edge (Figure 2-1 B). Eventually, the tip current dropped to $0.40 i_{T,\infty}$ without the contact of the tip with the flat lower terrace. The approach curve, however, did not fit with eq 2 at relatively long distances, even when a lower $i_{T,\infty}$ value was used in the theoretical curve (solid line in Figure 2-7 B), thereby requiring a long time for fitting to broaden the corresponding part of current–time profile in Figure 2-5. Overall, the experimental tip current at the last data point was always higher than the theoretical value (see the inset) to yield a large positive Δi_T value. Nevertheless, the adjusted z position at $L = 0$ was consistent with the position of the lower terrace (Figure 2-6 A).

Negative Δi_T values were obtained before the tip–substrate contact (Figure 2-7 C) when the tip approached the step edge of the substrate as depicted in Figure 2-1 C. The tip current at this location is expected to be higher than eq 2 (Figure 2-3), because the Pt tip is only partially blocked by the upper terrace and is partially exposed to the lower terrace. Accordingly, the theoretical curve was shifted laterally to minimize the sum of least squares, thereby yielding negative Δi_T values except for the contact point, where $\Delta i_T > 0$ (see the inset). This result indicates that the tip–substrate contact was avoidable selectively at step edges by setting a relatively large and negative threshold for Δi_T, which is small at upper terraces (Figure 2-7 A) and positive at lower terraces (Figure 2-7 B).

We assessed 151 approach curves in the line scan to find that the tip–substrate contact was unavoidable for one approach curve (Figure 2-7 D), where the glass sheath of tip barely contacted the edge of the substrate (Figure 2-1 D). This approach curve fitted very well with eq 2 until the tip contacted the substrate to deviate the tip current positively from eq 2 (see the inset). Before the contact, Δi_T values were as small as observed at lower and upper terraces far from step edges (Figure 2-7 A). Therefore, any threshold value for Δi_T can not avoid the contact between very edges of tip and substrate. Remarkably, closest tip–substrate distances just before contact with step edges were only ~20 nm (see insets of Figures 2-7 C and 2-7 D), which corresponds to a small step size as adjusted by the fuzzy logic algorithm near the substrate[20] (Figure 2-7). This result indicates that a small negative Δslope value (see eq 4) can sensitively and immediately detect the tip–substrate contact to avoid the damage of fragile nanotips (see below).

It should be noted that the SECM line scan experiment not only obtained empirical threshold Δi_T values for non-contact imaging (see below) but also determined the topography and inert reactivity of step edges, where experimental approach curves that did not fit eq 2 (Figures 2-7 B, 2-7 C, and 2-7 D) agreed remarkably well with approach curves simulated by the finite element method (Figures 2-13 A, 2-13 B, and 2-13 C, respectively). The post-imaging analysis of approach curves proved that the negative feedback effect from the wall of step edge resulted in the dip of the approach curve (Figure 2-13 A). The numerical analysis also ensured that high tip currents at the contact between the tip and the edges (Figures 2-13 B and 2-13 C) are due to a topographic effect not the local reactivity of substrate.

2.3.5 Non-Contact Intelligent Imaging

We employed real-time analysis of the approach curve to enable high-resolution and non-contact imaging of 6 μm-long square-shaped protrusion and recession surrounded by 500 nm-high step edges. A lateral step size of 1 μm was large enough to minimize a chance of positioning the glass sheath of tip over the step edge of the substrate, where the tip–substrate contact is unavoidable. A threshold value of $0.40i_{T,\infty}$ was set to terminate the tip approach at the lower terrace and the upper terrace far from step edges. The tip approach at step edges was terminated when Δi_T became more negative than a small negative threshold of –11 pA (i.e., –1.5% of $i_{T,\infty}$) as determined empirically from line scans. This negative threshold was not exceeded when the tip approached the lower terrace near the step edge, where Δi_T was larger but positive (see Figure 2-7 B). Non-contact imaging was ensured, because Δslope did not exceed a threshold value of –0.1 pA/nm established above.

Non-contact images of 6 μm x 6 μm protrusion were obtained by using the position of substrate surface determined by fitting approach curves with eq 2 (Figure 2-8 A) as well as the tip current at the last point of approach curves (Figure 2-8 B). The former image represents the topography of protrusion to determine not only its length of 6 μm but also its height of ~0.5 μm. The latter represents a reactivity image, which ensures the inert reactivity of upper and lower terraces. In addition, tip currents at edges are higher to represent not the local reactivity of the substrate but the less hindered diffusion of $Ru(NH_3)_6^{3+}$ from the solution over the lower terrace to the Pt tip. Even higher tip currents were observed at corners of recession, where the tip is exposed more to the lower terrace (Figure 2-12 A). In the reactivity image, the tip current reached the threshold value at the right edge of protrusion, which is dislocated toward the right-hand side as

indicated by dashed lines to lower the tip current. Interestingly, the lateral asymmetry of image based on the tip current is more enhanced than that of topography image to enable the more accurate location of step edges.

Importantly, the intelligent mode provides complimentary topography and reactivity images to unambiguously determine the height of step edges and the inertness of terraces, respectively, in contrast to a constant-height image based on the convolution of topography and reactivity (Figure 2-14 A). The constant-height mode yielded a lower tip current over the insulating protrusion, which is closer to the tip than the surrounding insulating region to exert a larger negative feedback effect on the tip current. This interpretation, however, is based on our prior knowledge of substrate inertness and topography. Without this knowledge, the constant-height image can be interpreted in a variety of ways, for instance, as an image of a flat substrate with a more reactive surrounding. Similarly, the topography and reactivity of substrate will be convoluted in a constant-current image of the non-flat substrate with step edges, where the tip current drops only to $0.8i_{T,\infty}$. A constant tip current of $>0.8i_{T,\infty}$ must be set even over flat regions to prevent the unambiguous determination of their inertness and position.

Both topography and reactivity images of 6 μm x 6 μm recession were obtained without the tip–substrate contact (Figures 2-8 C and 2-8 D, respectively). The recessed region was located by bringing the tip to its central region with dimensions of 5 μm x 5 μm as clearly shown in both images. The tip approached step edges just outside of the central region to yield higher tip currents at 7 μm x 7 μm frame (Figure 2-8 D), where the diffusion of $Ru(NH_3)_6^{3+}$ to the tip was less hindered. Interestingly, the tip current was higher at edges than corners, where the Pt tip was less exposed to the solution over the lower terrace (Figure 2-12 B). Moreover, the tip current reached the threshold value at top corners, but not bottom corners, which indicates that the recession was

dislocated downward in the image as indicated by dashed lines. Again, step edges were located more accurately by the enhanced asymmetry of the image based on the tip current to demonstrate its utility. The topography image measures the depth of recession (~0.5 μm) and the tilt of the substrate along the vertical axis as emphasized at the upper terrace. Complimentarily, the reactivity image ensured the inertness of upper and lower terraces. By contrast, the corresponding constant-height image of a recession (Figure 2-14 B) can be misinterpreted without the prior knowledge of substrate topography or reactivity to assign the higher tip current over the recessed central region to higher reactivity.

It should be noted that unavoidable contact between the glass sheath of the tip and the step edge of substrate occurred occasionally but did not damage tips as shown by SEM after imaging (Figures 2-9 A and 2-9 B). The tips were not damaged, not only because small step sizes of 20 nm or less were used during the tip approach, but also because the tips were retracted as soon as the tip–substrate contact was indicated by an abrupt change in the slope of approach curve. Tips were seriously damaged when the tips were pushed further to a substrate after the initial tip–substrate contact during imaging of recession and protrusion (Figures 2-9 C and 2-9 D, respectively). In these cases, a high threshold value of –0.5 pA/nm was set for Δslope (see eq 4) to cause the multiple-step contact as demonstrated by the corresponding approach curves (Figure 2-15). The time profile of tip current (Figure 2-16) showed a sudden increase in $i_{T,\infty}$ when the glass sheath near the Pt tip was cracked (Figure 2-9 C), but not when only the glass sheath was damaged (Figure 2-9 D). The approach curves were analyzed to determine total step sizes of ~100 nm after the tip–substrate contact (Figure 2-15). These total step sizes are comparable to those of intermittent contact mode, where a tip was pushed toward a substrate by three steps of 50 nm after the initial tip–substrate contact to ensure that the damping of tip vibration well exceeds the noise level.[10]

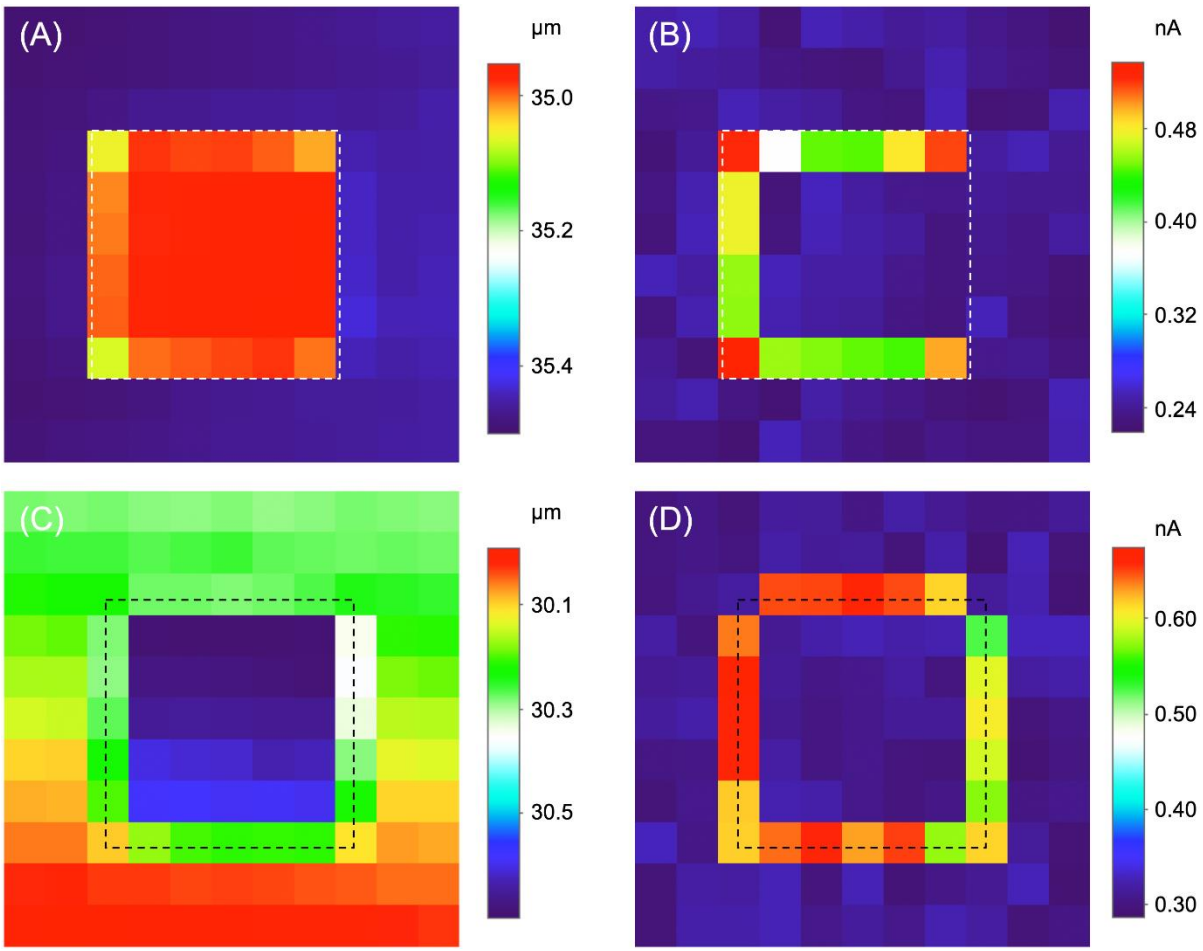

Figure 2-8 11 μm x 11 μm images based on (A) topography and (B) current at a protrusion and (C) topography and (D) current at a recession on insulating substrates in 10 mM $Ru(NH_3)_6^{3+}$ and 1 M KCl. Each pixel is equivalent to 1 μm x 1 μm. The position of step edges is represented by 6 μm x 6 μm dashed boxes. The tip was scanned laterally from the left bottom corner and stepped upward after each line scan.

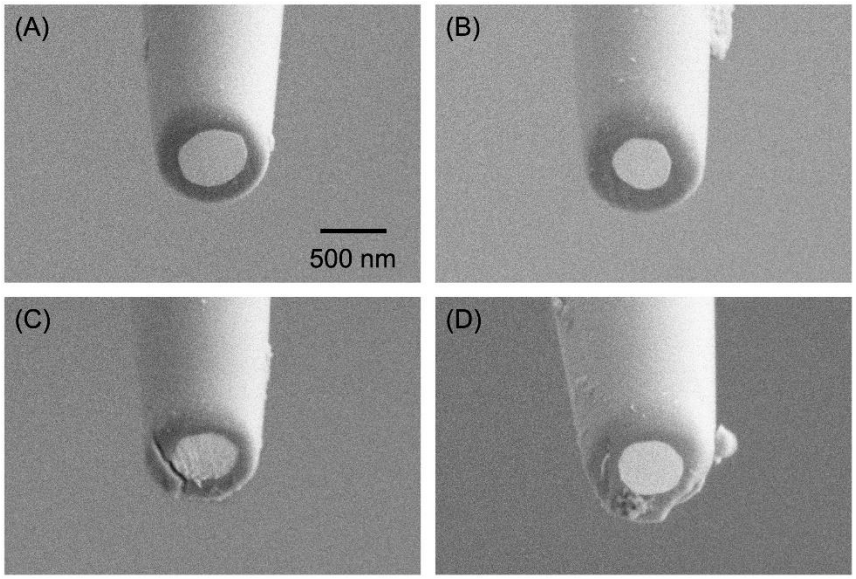

Figure 2-9 SEM images of (A) and (B) undamaged and (C) and (D) damaged Pt nanotips after SECM imaging with low and high threshold values of –0.1 and –0.5 pA/nm for Δslope, respectively. Figure 2-10 shows SEM images of these tips just after FIB milling.

2.3.6 Imaging Time

Here, we assess the imaging time of the proposed method, which is intrinsically long but can be improved significantly. The measurement and analysis of the approach curve at every lateral tip position requires longer imaging time than constant-height and constant-current modes. In this work, the measurement of the approach curve took twice longer than its real-time analysis. In the algorithm shown in Figure 2-4, it took ~0.1 s to move and stabilize the tip position before the tip current was measured and averaged for ~0.1 s. Then, it took ~0.1 s to quantitatively analyze the approach curve. The majority of analysis time was spent for non-linear fitting, which was even longer when a good fit was not obtained for approach curves at lower terraces adjacent to the edge, i.e., curve 4 in Figure 2-5. Overall, it took ~40 min for the measurement of 151 approach curves in line scan (Figure 2-5) and ~32 min for 121 approach curves in imaging (Figure 2-8), which

corresponds to ~16 s per approach curve with ~50 points. A travel distance of ~5 μm for each approach curve yields an apparent velocity of ~0.3 μm/s. This velocity is similar to a velocity of ~0.3 μm/s employed in the intermittent contact mode,[10] which is also intrinsically slow.

The speed of approach curve measurement can be made much faster by employing instrumentation developed for fast scanning ion-conductance microscopy.[35] For instance, an ionic current of ~2.7 nA was measured with a precision of ±0.5 pA (i.e., ±0.02% of the ionic current) when an ~100 nm-diameter water-filled nanopipet traveled 2 μm in 4–40 ms, i.e., 50–500 μm/s.[36] In comparison with our setup, not only was the similar current measured more precisely despite much faster sampling, but also the approach velocity was ~100–1000 times faster. Importantly, this high velocity is still slow enough to measure the current response of SECM nanotips under diffusion-limited steady-state conditions, which were also assumed for SECM theory (e.g., eq 2). These conditions are satisfied at up to the maximum velocity of tip approach to an insulating substrate, v_{max}, given by[37]

$$v_{max} = \frac{D}{a}\frac{RG}{115+22RG^{1.9}} \quad (6)$$

where an error of 2% is anticipated. Eq 6 with D = 1 x 10^{-5} cm^2/s gives a high v_{max} value of ~35 μm/s for Pt tips with a = 0.25 μm and RG = 1.5 as used in this study. An even higher v_{max} value of ~600 μm/s is obtained for nanopipet tips with a = 15 nm and RG = 1.4 as used in our previous studies.[38,39] With these high velocities, the imaging time is limited by real-time analysis of approach curves, which may be accelerated by using a fast computing method, e.g., quantum computing.[40]

It should be noted that the imaging mode proposed in this work is feasible by using micrometer-sized tips, but is less practical, because the slower tip approach to a substrate is required to avoid a convection effect on the tip current. Eq 6 yields a v_{max} value of ~0.4 μm/s for

a tip with a = 12.5 μm and RG = 10. Moreover, a larger tip with lower distance sensitivity is used for imaging a larger topographic profile, which increases the travel distance of approach curve and, subsequently, imaging time. Previously, SECM topography imaging was enabled by moving a micrometer-sized tip (a = 12.5 μm) to insulating and conductive substrates at 40 μm/s to obtain the transient convection-controlled tip current that was in-dependent of substrate reactivity.[41]

2.3.7 General Applicability

We envision that the proposed imaging method will be generally applicable to quantitatively determine the topography and reactivity of various substrates by analyzing experimental approach curves both in real time and after imaging complimentarily. For real-time analysis, eq 2 can be combined or replaced with analytical expressions for flat substrates with various reactivities to cover a wide spectrum of approach curves from purely negative ones to purely positive ones.[24,33,42] These analytical expressions are similar to each other (see Supporting Information) and will be adoptable into our future software straightforwardly. By contrast, the tip approach can be terminated without the tip–substrate contact when an experimental approach curve deviates from theoretical curves for any reason, e.g., the local non-flatness of the substrate. The resultant experimental approach curve can be analyzed numerically after imaging to determine the local topography and reactivity of the substrate, which are manifested as causes of the deviation. In this work, experimental approach curves near or at step edges were fitted well not by real-time analysis based on eq 2 (Figures 2-7 B, 2-7 C, and 2-7 D) but by post-imaging analysis based on the finite element method (Figures 2-13) to locate non-reactive step edges. This result suggests that the numerical analysis of approach curves will be useful for non-flat substrates with various reactivities.

2.4 Conclusions

In this work, a new imaging mode of SECM was proposed by implementing the real-time analysis of the approach curve for the first time, thereby enabling active control of nanometer tip–substrate distances without contact. In contrast to combined SECM techniques,[9] this imaging mode is based on standard instrumentation, which is controlled by the advanced version of Labview-based software[20,21] and equipped with a nanotip[18,19] to quickly yield steady-state diffusion-limited current without a convection effect.[37] This powerful operation mode yielded high-resolution and non-contact images of the insulating substrate with step edges. Advantageously, the step height and inert reactivity of substrate were unambiguously determined from topography and reactivity images (Figure 2-8), respectively, as obtained by locally adjusting tip height (Figure 2-6 A) and threshold tip current (Figure 2-6 B) to maintain short tip–substrate distances and, subsequently, high spatial resolution (eq 1). By contrast, other imaging modes based on standard instrumentation employ constant heights[5,12,14] or a constant threshold current,[8,13,16] where long distances from non-flat substrates are used for non-contact imaging to compromise the lateral spatial resolution and the accuracy of inert reactivity and step height of substrate.

SECM imaging based on real-time analysis of approach curve can be more versatile and robust to image the topography and reactivity of various substrates. Analytical theories are available for disk-shaped tips at flat substrates with a wide range of electrochemical reversibility[24,33,42] as diverse guidelines to decide whether a tip can approach closer to a substrate without contact. The topography and reactivity of substrate can be determined in real time from good fits between experimental and theoretical curves or after imaging by the numerical analysis of experimental approach curves, which are terminated as soon as the tip current deviates from theoretical curves. The numerical analysis requires the further exploration of approach curves at

non-flat substrates, which will yield new fundamental insights into SECM. Ultimately, theoretical curves may be replaced with characteristic approach curves that are measured at different locations of a target substrate and numerically analyzed in advance. This empirical approach may be reinforced by machine learning,[43] where experimental approach curves from previous images are accumulated and used as guidelines to stop the tip approach immediately before the tip–substrate contact.

2.5 Supporting Information

2.5.1 SEM of FIB-Milled Tips

We employed SEM to image Pt tips immediately after FIB milling (Figure 2-10). SEM images of the same tips after SECM imaging are shown in Figure 2-9.

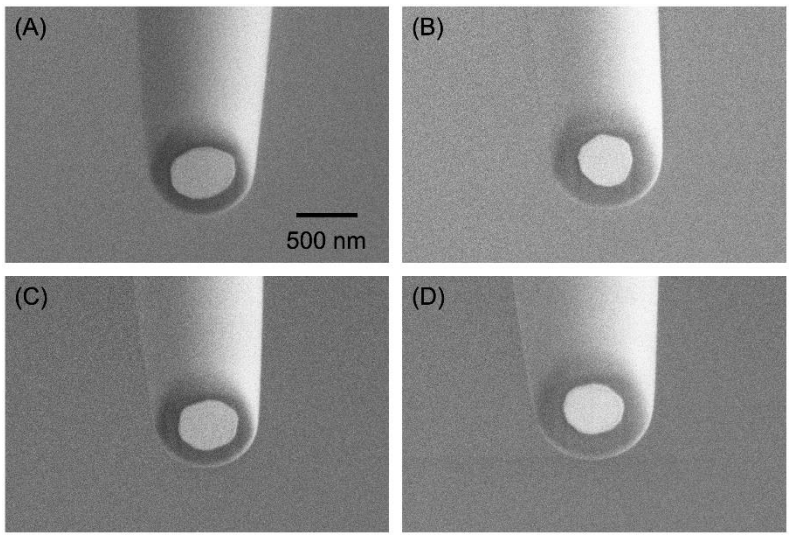

Figure 2-10 SEM images of Pt tips immediately after FIB milling. Their SEM images after SECM imaging are shown in the corresponding parts of Figure 2-9.

2.5.2 Finite Element Simulation of Characteristic Approach Curves

The limiting current at a disk-shaped tip in the SECM configuration was simulated by solving a three-dimensional (3D) diffusion problem with an array of square-shaped protrusions or recessions as defined in Cartesian coordinates (Figure 2-11). The origin of the coordinate axes was set at the center of a protrusion (or recession). The length, *m*, interval, *s*, and height, *h*, of recessions (or protrusions with $h < 0$) were determined from SEM images of the substrate (Figure 2-2). No protrusion (or recession) was placed on the half of the substrate, which did not contribute to the tip current. Initially, the solution contained redox-active species, O, at a bulk concentration of c_0. The steady-state diffusion of the redox molecule in solution was defined by

$$\frac{\partial c}{\partial t} = D\left(\frac{\partial^2 c}{\partial x^2} + \frac{\partial^2 c}{\partial y^2} + \frac{\partial^2 c}{\partial z^2}\right) = 0 \quad \text{(S-1)}$$

where c is the ion concentration at (x, y, z). The zero concentration of redox species was the electrode surface boundary condition. The insulating substrate yielded zero flux perpendicular to these boundaries. Boundary conditions at simulation space limits were the bulk concentration of redox species, c_0.

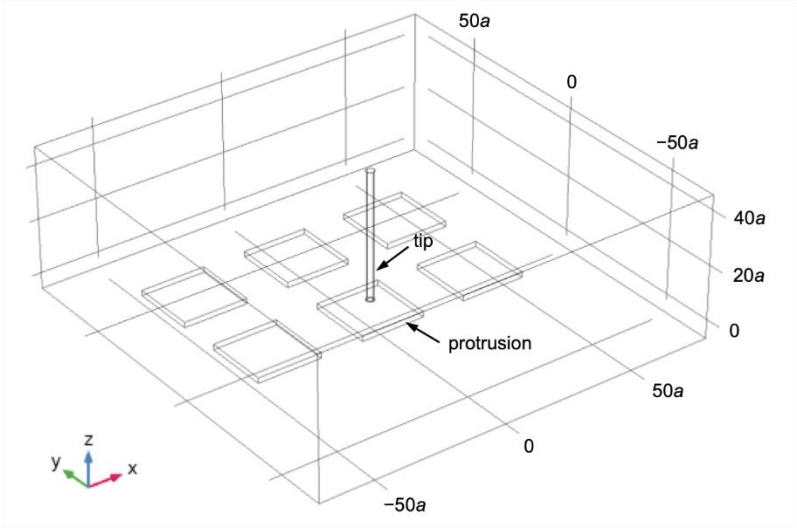

Figure 2-11 Scheme for the finite element simulation of SECM diffusion problems with a disk tip positioned over an insulating substrate with an array of squared-protrusions (or recessions).

We employed COMSOL Multiphysics (version 5.4a, COMSOL, Inc., Burlington, MA) to solve the 3D SECM diffusion problem in dimensionless form. Eq 1 was defined by dimensionless parameters as

$$\frac{\partial C}{\partial t} = \left(\frac{\partial^2 C}{\partial X^2} + \frac{\partial^2 C}{\partial Y^2} + \frac{\partial^2 C}{\partial Z^2} \right) = 0 \quad \text{(S-2)}$$

where

$$C = \frac{c}{c_0} \quad \text{(S-3)}$$

$$t = \frac{4Dt}{a^2} \quad \text{(S-4)}$$

$$X = \frac{x}{a} \quad \text{(S-5)}$$

$$Y = \frac{y}{a} \quad \text{(S-6)}$$

$$Z = \frac{z}{a} \quad \text{(S-7)}$$

In addition, dimensionless geometric parameters were defined for protrusions (or recessions) as

$$M = \frac{m}{a} \quad \text{(S-8)}$$

$$S = \frac{s}{a} \quad \text{(S-9)}$$

$$H = \frac{h}{a} \quad \text{(S-10)}$$

This problem was solved numerically to calculate the normalized tip current, $i_T/i_{T,\infty}$, which was set to 1 at $L = 30$.

Figure 2-12 shows approach curves simulated at corners of recession and protrusion. Red lines were shifted by the height of protrusion (or depth of recession) to obtain dashed lines for edge–corner and edge–edge contacts.

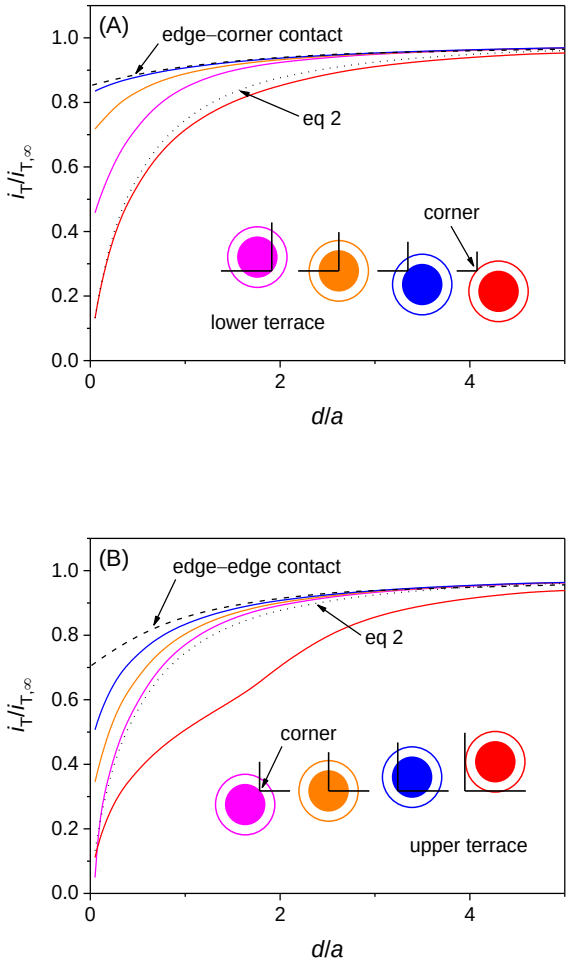

Figure 2-12 Characteristic approach curves (solid lines) simulated at various lateral tip positions over the corner of (A) protrusion and (B) recession as depicted in the inset (top view) by using the same colors.

Experimental approach curves near or at step edges (Figures 2-7 B, 2-7 C, and 2-7 D) fitted very well with simulated approach curves (Figure 2-13 A, 2-13 B, and 2-13 C, respectively). Remarkably, excellent fits between experimental and simulated approach curves were obtained down to $d/a \approx 0$ when the tip approached a step edge (Figures 2-13 B and 2-13 C).

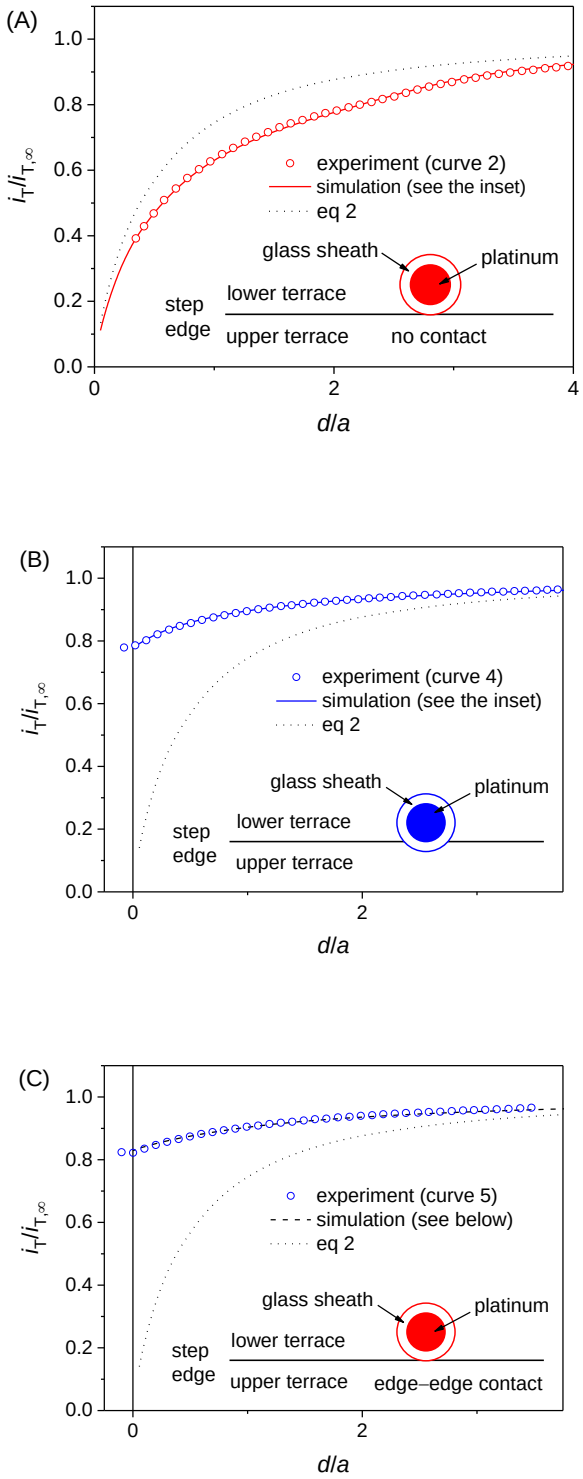

Figure 2-13 Experimental approach curves at step edges from Figures (A) 2-7 B, (B) 2-7 C, and (C) 2-7 D fitted with simulated curves at step edges. The best fits were obtained by using a = 0.20 µm and RG = 1.6.

2.5.3 Constant-Height Images

We employed the constant height mode to image 6 µm × 6 µm protrusion and recession (Figure 2-14 A and 2-14 B, respectively), where the contrast of the tip current can be attributed the substrate topography when the inert reactivity of the substrate is known. Without the knowledge, the higher tip current at a higher terrace can be misinterpreted as a higher reactivity.

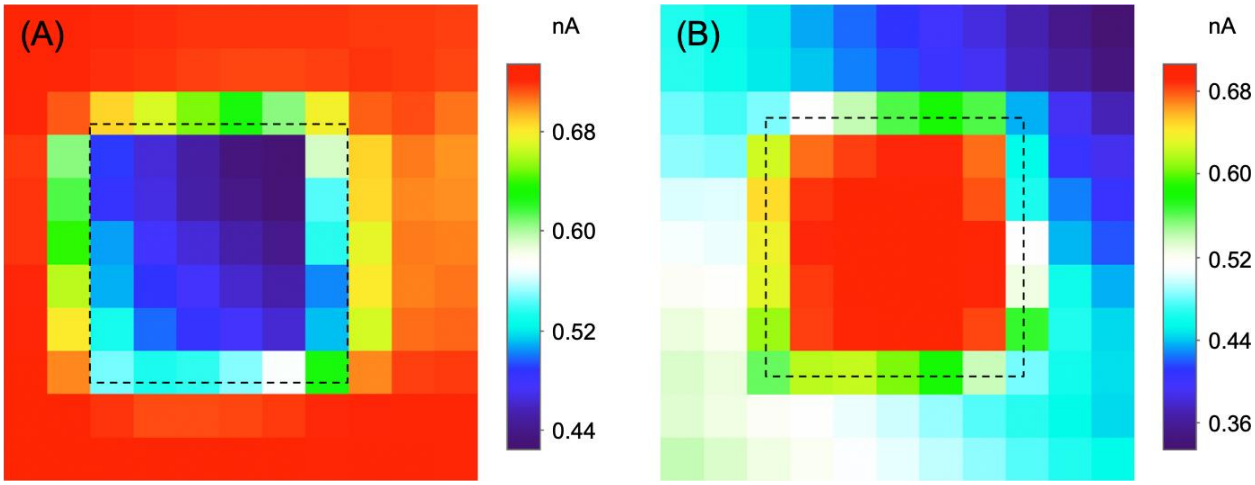

Figure 2-14 11 µm × 11 µm constant-height images at (A) a protrusion and (B) a recession on insulating substrates in 10 mM $Ru(NH_3)_6^{3+}$ and 1 M KCl. Each pixel is equivalent to 1 µm × 1 µm. The position of step edges is represented by 6 µm × 6 µm dashed boxes. The tip was scanned laterally from the left top corner and stepped downward after each line scan

2.5.4 Approach Curves with Multistep Tip-Substrate Contact

Pt tips were seriously damaged (Figures 2-9 C and 2-9 D) when they were pushed several steps further toward substrates after the tip–substrate contact as shown in approach curves (Figures 2-15 A and 2-15 B, respectively). Curves 1 and 2 in the respective figures are indicated in the time profile of tip current in Figures 2-16 A and 2-16 B, respectively.

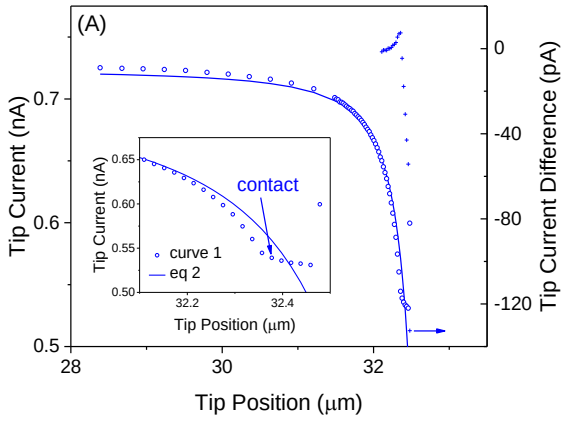

Figure 2-15 Experimental approach curves (circles) with the tip–substrate contact. Curves 1 and 2 are indicated by arrows in Figure 2-16. Theoretical curves (lines) were obtained by the best fit of eq 2. Crosses are Δi_T values defined by eq 3. Insets show the last part of approach curves.

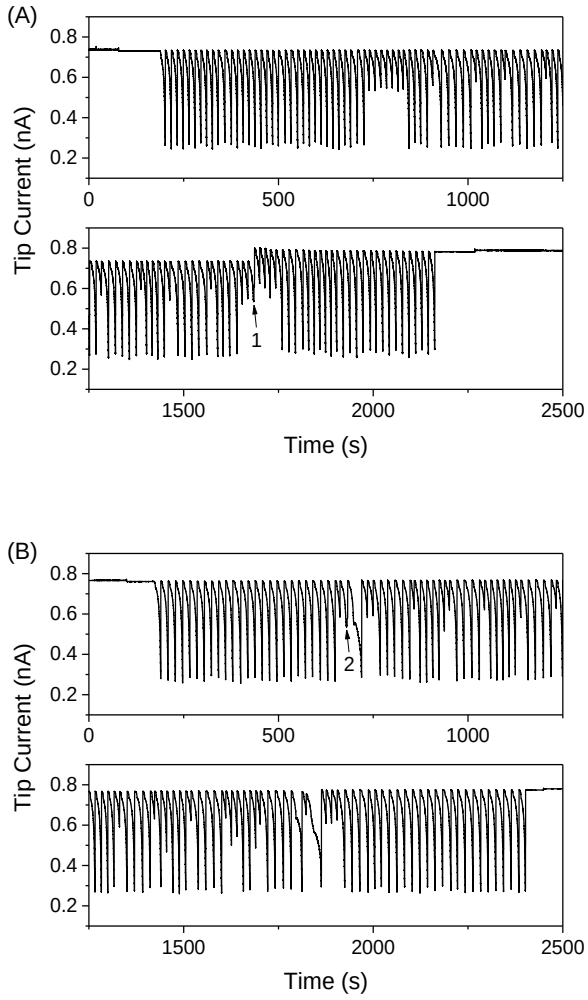

Figure 2-16 Current of Pt tips damaged during SECM imaging. SEM images of damaged tips used for parts (A) and (B) are shown in Figures 2-9 C and 2-9 D, respectively. Arrows indicate approach curves with the multi-step tip–substrate contact shown in Figure 2-15.

2.5.5 Analytical Expressions of Approach Curves at Reactive Substrates

The proposed imaging method can be extended for substrates with various reactivity by combining or replacing eq 2 with appropriate equations, e.g., for purely positive feedback effects at conductors as give by[44]

$$\frac{i_T^{PF}}{i_{T,\infty}} = a + \frac{p}{4b\arctan(L)} + \left(1 - a - \frac{1}{2b}\right)\frac{2}{p}\arctan(L) \quad \text{(S-11)}$$

with

$$a = \ln 2 + \ln 2\left[1 - \frac{2}{p}\arccos\left(\frac{1}{RG}\right)\right] - \ln 2\left\{1 - \left[\frac{2}{p}\arccos\left(\frac{1}{RG}\right)\right]^2\right\} \quad \text{(S-12)}$$

$$b = 1 + 0.639\left[1 - \frac{2}{p}\arccos\left(\frac{1}{RG}\right)\right] - 0.186\left\{1 - \left[\frac{2}{p}\arccos\left(\frac{1}{RG}\right)\right]^2\right\} \quad \text{(S-13)}$$

where i_T^{PF} is the tip current based on the positive feedback effect. Both eqs 2 and S-11 are functions of only *L* because *RG* is determined separately to yield constant α and β values in eq S-11. The additional use of eq S-11 will enable non-contact topography and reactivity imaging of non-flat substrates with both insulating and conductive regions. Eqs 2 and S-11 can be used also to obtain approach curves for irreversible electron-transfer reactions at conductive substrates.[45] More generally, eq S-11 can be used to obtain approximate equations for any electron-transfer kinetics at substrates in feedback and substrate generation/tip collection modes under quasi-steady states.[46] It should be noted that all theoretical expressions are applicable for flat substrates and disk-shaped tips.

2.6 Acknowledgements

This work was supported by the National Institutes of Health (R01 GM112656). D.T.J. and K.C.L also acknowledge funding through the Army Research Office Young Investigator Grant No. 66446-CH-YIP (Award Number W911NF-17-1-0098).

2.7 References

(1) Amemiya, S.; Bard, A. J.; Fan, F.-R. F.; Mirkin, M. V.; Unwin, P. R. *Annu. Rev. Anal. Chem.* **2008**, *1*, 95-131.

(2) Bard, A. J.; Mirkin, M. V., *Scanning electrochemical microscopy*. 2nd ed.; Tayler and Francis: New York, 2012.

(3) Amemiya, S., Scanning electrochemical microscopy of nanopores, nanocarbons, and nanoparticles. In *Nanoelectrochemistry*, Mirkin, M. V.; Amemiya, S., Eds. Taylor and Francis: Boca Raton, FL, 2015; pp 621-653.

(4) Bard, A. J.; Mirkin, M. V.; Unwin, P. R.; Wipf, D. O. *J. Phys. Chem.* **1992**, *96*, 1861-1868.

(5) Kwak, J.; Bard, A. J. *Anal. Chem.* **1989**, *61*, 1794-1799.

(6) Fan, F.-R. F.; Bard, A. J.; He, P., Instrumentation. In *Scanning electrochemical microscopy*, 2nd ed.; Bard, A. J.; Mirkin, M. V., Eds. Tayler and Francis: New York, 2012; pp 15-23.

(7) Amemiya, S.; Guo, J.; Xiong, H.; Gross, D. A. *Anal. Bioanal. Chem.* **2006**, *386*, 458-471.

(8) Wipf, D. O.; Bard, A. J.; Tallman, D. E. *Anal. Chem.* **1993**, *65*, 1373-1377.

(9) O'Connell, M. A.; Wain, A. J. *Anal. Methods* **2015**, *7*, 6983-6999.

(10) Lazenby, R. A.; McKelvey, K.; Unwin, P. R. *Anal. Chem.* **2013**, *85*, 2937-2944.

(11) Wei, C.; Bard, A. J. *J. Electrochem. Soc.* **1995**, *142*, 2523-2527.

(12) Zhang, M. M. N.; Long, Y.-T.; Ding, Z. *J. Inorg. Biochem.* **2012**, *108*, 115-122.

(13) Jedraszko, J.; Michalak, M.; Jönsson-Niedziolka, M.; Nogala, W. *J. Electroanal. Chem.* **2018**, *815*, 231-237.

(14) Filice, F. P.; Li, M. S. M.; Henderson, J. D.; Ding, Z. F. *J. Phys. Chem. C* **2015**, *119*, 21473-21482.

(15) Lazenby, R.; McKelvey, K.; Peruffo, M.; Baghdadi, M.; Unwin, P. *J. Solid State Electrochem.* **2013**, *17*, 2979-2987.

(16) Takahashi, Y.; Shevchuk, A. I.; Novak, P.; Babakinejad, B.; Macpherson, J.; Unwin, P. R.; Shiku, H.; Gorelik, J.; Klenerman, D.; Korchev, Y. E.; Matsue, T. *Proc. Natl. Acad. Sci. U. S. A.* **2012**, *109*, 11540-11545.

(17) Cornut, R.; Lefrou, C. *J. Electroanal. Chem.* **2007**, *608*, 59-66.

(18) Amemiya, S., Nanoscale scanning electrochemical microscopy. In *Electroanalytical chemistry*, Bard, A. J.; Zoski, C. G., Eds. CRC Press: 2015; pp 1-72.

(19) Kai, T.; Zoski, C. G.; Bard, A. J. *Chem. Commun.* **2018**, *54*, 1934-1947.

(20) Barforoush, J. M.; McDonald, T. D.; Desai, T. A.; Widrig, D.; Bayer, C.; Brown, M. K.; Cummings, L. C.; Leonard, K. C. *Electrochim. Acta* **2016**, *190*, 713-719.

(21) Pathirathna, P.; Balla, R. J.; Jantz, D. T.; Kurapati, N.; Gramm, E. R.; Leonard, K. C.; Amemiya, S. *Anal. Chem.* **2019**, *91*, 5446-5454.

(22) Nioradze, N.; Chen, R.; Kurapati, N.; Khyataeva-Domanov, A.; Mabic, S.; Amemiya, S. *Anal. Chem.* **2015**, *87*, 4836-4843.

(23) Kim, J.; Shen, M.; Nioradze, N.; Amemiya, S. *Anal. Chem.* **2012**, *84*, 3489-3492.

(24) Nioradze, N.; Kim, J.; Amemiya, S. *Anal. Chem.* **2011**, *83*, 828-835.

(25) Kim, J.; Izadyar, A.; Nioradze, N.; Amemiya, S. *J. Am. Chem. Soc.* **2013**, *135*, 2321-2329.

(26) Nioradze, N.; Chen, R.; Kim, J.; Shen, M.; Santhosh, P.; Amemiya, S. *Anal. Chem.* **2013**, *85*, 6198-6202.

(27) Kim, J.; Kim, B.-K.; Cho, S. K.; Bard, A. J. *J. Am. Chem. Soc.* **2014**, *136*, 8173-8176.

(28) Chen, R.; Balla, R. J.; Li, Z. T.; Liu, H. T.; Amemiya, S. *Anal. Chem.* **2016**, *88*, 8323-8331.

(29) Fulian, Q.; Fisher, A. C.; Denuault, G. *J. Phys. Chem. B* **1999**, *103*, 4387–4392.

(30) Sklyar, O.; Wittstock, G. *J. Phys. Chem. B* **2002**, *106*, 7499-7508.

(31) Cornut, R.; Bhasin, A.; Lhenry, S.; Etienne, M.; Lefrou, C. *Anal. Chem.* **2011**, *83*, 9669-9675.

(32) Gossage, Z. T.; Simpson, B. H.; Schorr, N. B.; Rodríguez-López, J. *Anal. Chem.* **2016**, *88*, 9897-9901.

(33) Lefrou, C. *J. Electroanal. Chem.* **2006**, *592*, 103-112.

(34) Liu, B.; Bard, A. J. *J. Phys. Chem. B* **2002**, *106*, 12801-12806.

(35) Simeonov, S.; Schaffer, T. E. *Nanoscale* **2019**, *11*, 8579-8587.

(36) Novak, P.; Shevchuk, A.; Ruenraroengsak, P.; Miragoli, M.; Thorley, A. J.; Klenerman, D.; Lab, M. J.; Tetley, T. D.; Gorelik, J.; Korchev, Y. E. *Nano Lett.* **2014**, *14*, 1202-1207.

(37) Cornut, R.; Poirier, S.; Mauzeroll, J. *Anal. Chem.* **2012**, *84*, 3531-3537.

(38) Shen, M.; Ishimatsu, R.; Kim, J.; Amemiya, S *J. Am. Chem. Soc.* **2012**, *134*, 9856-9859.

(39) Chen, R.; Balla, R. J.; Lima, A.; Amemiya, S. *Anal. Chem.* **2017**, *89*, 9946-9952.

(40) Wiebe, N.; Braun, D.; Lloyd, S. *Phys. Rev. Lett.* **2012**, *109*, 050505.

(41) Borgwarth, K.; Ebling, D. G.; Heinze, J. *Ber. Bunsen-Ges. Phys. Chem.* **1994**, *98*, 1317-1321.

(42) Cornut, R.; Lefrou, C. *J. Electroanal. Chem.* **2008**, *621*, 178-184.

(43) Huang, B. Y.; Li, Z. H.; Li, J. Y. *Nanoscale* **2018**, *10*, 21320-21326.

(44) Lefrou, C. *J. Electroanal. Chem.* **2006**, *592*, 103.

(45) Cornut, R.; Lefrou, C. *J. Electroanal. Chem.* **2008**, *621*, 178.

(46) Nioradze, N.; Kim, J.; Amemiya, S. *Anal. Chem.* **2011**, *83*, 828.

3.0 Simultaneous Imaging of Nanoscale Reactivity and Topography by Intelligent Scanning Electrochemical Microscopy

Ryan J. Balla, Dylan T. Jantz, Siao-Han Huang, Niraja Kurapati, Shigeru Amemiya and Kevin C. Leonard. This thesis author fabricated electrodes, collaborated with programmers to create novel software to address long-standing SECM problems, utilized COMSOL simulation and collected and analyzed experimental data.

3.1 Introduction

Nanoscale scanning electrochemical microscopy (SECM) has emerged as a powerful method that can visualize the reactivity and topography of single nanometer-sized objects in the electrolyte solution.[1,2] Recently, the constant-height mode of SECM based on feedback effects[3] was used to image molecular transport through single solid-state nanopores with diameters of down to ~40 nm[4,5] and electrocatalysis at single metal nanoparticles with diameters of down to ~120 nm.[6,7] Constant-height imaging, however, suffers from the convolution of local reactivity and topography of substrate,[8] which was mitigated by the separate measurement and analysis of SECM approach curves.[4-7] By contrast, the local reactivity of substrate can be resolved from topography by maintaining a constant tip–substrate distance during constant-current imaging,[9] which is straightforward only for the substrates that are relatively flat or uniformly reactive (or inert) as demonstrated by nanoscale SECM.[10,11] Alternatively, another imaging method, e.g., atomic force microscopy, was combined with SECM[12] to obtain the topography image of single

nanostructures in advance, which guides constant-distance reactivity imaging by SECM. Combined SECM techniques, however, require specialized hardware and multifunctional probes, which have been limiting their adoption.[13]

Herein, we advance the intelligent mode of nanoscale SECM[14] to simultaneously and independently visualize the reactivity and topography of non-flat substrates with both reactive and inert regions. In the intelligent mode, the distance-dependent current response of a nanotip is assessed after every step of the vertical tip approach to the substrate to achieve a short tip–substrate distance, d, without contact, thereby maximizing the spatial resolution based on feedback effects as represented by[15]

$$h^{\infty} = 1.5d + a \quad (1)$$

where h^{∞} is the radius of local substrate surface seen by a disk-shaped tip with a radius of a. Recently, we employed non-flat inert substrates to demonstrate that the intelligent mode enables non-contact topography imaging with a high resolution of $h^{\infty} \leq 1.45a$ with $d \leq 0.3a$ in eq 1[14] in contrast to other imaging modes based on approach curves, i.e., intermittent contact[16] and hopping ($h^{\infty} = 8.5a$ with $d = 5a$[17]) modes. In this study, we reinforce the intelligent mode by the post-analysis of each approach curve to locate the substrate under the tip for quantitative topography imaging and determine the tip current at a constant distance for topography-independent reactivity imaging.

Experimentally, we demonstrate the unprecedented power of the intelligent mode by resolving simultaneous changes in reactivity and topography at the grooved boundary between flush glass and Au surfaces of an interdigitated electrode (Figure 3-1). While the respective surfaces exert only negative or positive feedback effects on a tip (Figures 3-1 A and 3-1 B), the tip experiences both effects over the boundary to yield the mixed feedback current response (Figure

3-1 C). Abrupt changes in the mixed feedback current across the boundary can be monitored not by the constant-current mode[9] but by the intelligent mode to yield a topography-independent reactivity image. Moreover, intelligent topography imaging reveals the nanoscale grooves, which are unnoticed by constant-height imaging owing to the convolution of topography with reactivity. In addition to the feedback current, we utilize the tip current based on electron tunneling to the edge of the Au band for non-contact tip positioning in contrast to the sole use of the tunneling mode for topography imaging,[18] which requires a conductive substrate. Importantly, intelligent images are based on the feedback mechanism not on the tunneling mechanism, which can not be distinguished by constant-height imaging.[19,20]

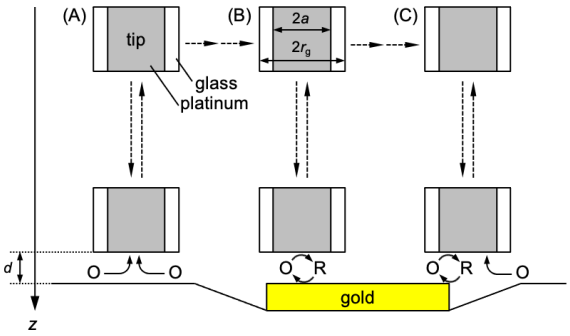

Figure 3-1 Scheme of tip approach for (A) negative, (B) positive, and (c) mixed feedback effects for intelligent SECM imaging of a gold band on a grooved glass substrate under a disk-shaped Pt nanotip with a thin glass sheath. Dashed lines with arrows indicate the tip movement. O and R are the oxidized and reduced forms of a redox mediator, respectively.

3.2 Experimental

3.2.1 Chemicals and Materials

$Ru(NH_3)_6Cl_3$ was obtained from Strem Chemicals (Newburyport, MA). KCl (≥99%) was purchased from Sigma Aldrich (Milwaukee, WI). Interdigitated Au electrodes on glass substrates (012260) were obtained from CH Instruments (Austin, TX). A Milli-Q Advantage A10 system combined with Elix 3 Advantage (EMD Millipore, Billerica, MA) purified tap water to obtain ultrapure water with the resistivity of 18.2 MΩ·cm and the total organic carbon of 2–3 ppb.[21]

3.2.2 SECM Imaging

A home-built SECM instrument[22] was equipped with a potentiostat (CHI 802D, CH Instruments) and controlled by using the Labview program based on a custom fuzzy logic algorithm.[23] An SECM stage was accommodated in an isothermal chamber equipped with heat sinks and vacuum insulation plates to minimize thermal drift.[24] Pt tips with inner and outer radii of ~0.22 and ~0.33 μm, respectively, were fabricated by laser-assisted pulling, heat annealing, and focused-ion-beam (FIB) milling[25,26] and characterized by scanning electron microscopy (SEM) before and after use for SECM experiments to check the damage of the tips. The tips were protected from electrostatic discharge[27] under sufficiently high humidity (>30%)[28] as detailed in Supporting Information and also from electrochemical damage by using the cell-on-between-run function of the modified potentiostat.[29] Pt wires served as counter and quasi-reference electrodes. The tip potential was set to obtain the steady-state current based on the diffusion-limited reduction of 10 mM $Ru(NH_3)_6^{3+}$ in 1 M KCl.

3.2.3 Characterization of Interdigitated Au Electrodes

We employed SEM and atomic force microscopy (AFM) to characterize the topography of interdigitated Au electrodes. An SEM image of the Au band array shows a groove on the glass surface at each side of the Au band (Figure 3-2 A). A part of the Au band and surroundings was removed by FIB milling to view the cross-section (Figure 3-2 B), which ensures that the groove is formed at the glass region. The glass surface beyond the groove is nearly flush with the gold surface as confirmed by AFM (Figures 3-2 C and D). The AFM images show not only the ~100-depth grooves but also the asymmetric curvature of the Au surface, which widens a groove more than the other groove. Subsequently, an SECM tip can penetrate the ~2 μm-wide groove deeper than the ~1 μm-wide groove to manifest the asymmetric topography of the Au band (see below).

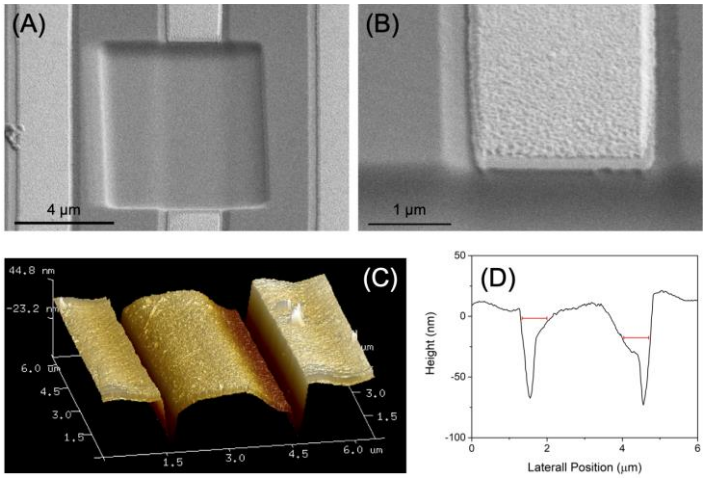

Figure 3-2 (A) and (B) SEM images of Au bands embedded in a glass substrate. A Au band was milled by FIB to expose the cross-section. (C) AFM image of unmilled Au band and (D) plot of its surface profile. Bars represent the outer diameter of the SECM tip (0.66 μm) and locate its penetration depths.

3.3 Results and Discussion

3.3.1 Theoretical Approach Curves

We employed the finite element method to simulate approach curves at different lateral positions of an SECM tip over a conductive band on a grooved insulating substrate (see Supporting Information), which mimics the interdigitated electrodes (Figure 3-2). We considered the groove of the glass surface adjacent to a Au band but neglected the curvature of the Au surface. In the simulated curves (Figure 3-3), the tip–substrate distance, d, and the tip current, i_T, were normalized against the tip radius, a, and the tip current in the bulk solution, $i_{T,\infty}$, respectively, with

$$i_{T,\infty} = 4xnFDc_0a \quad (2)$$

where x is a function of RG (= r_g/a =~1.5; see Figure 3-1), n is the number of the transferred electrons, and D and c_0 are the diffusion coefficient and concentration of the redox mediator in the solution.

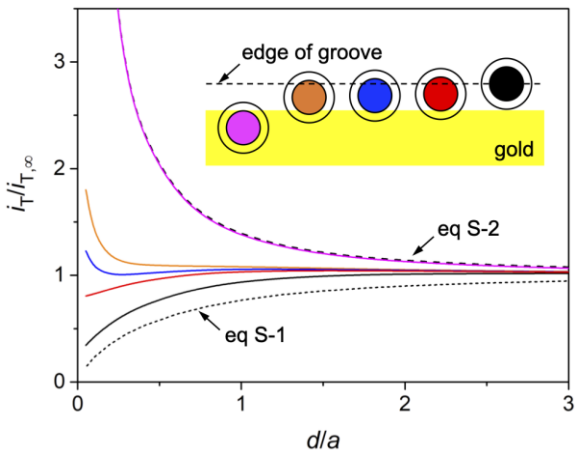

Figure 3-3 Characteristic approach curves (solid lines) simulated at various lateral tip positions over a Au band as depicted in the inset (top view) by using the same colors. Dotted and dashed lines represent diffusion-limited negative and positive curves, respectively.

The finite element simulation demonstrated that approach curves over the grooved boundary between Au and glass regions are highly sensitive to the lateral position of the tip owing to mixed positive and negative feedback effects from the respective regions (Figure 3-1 C). When the entire surface of the Pt tip is located over a Au band (purple line in Figure 3-3), the resultant current was maximized to follow the diffusion-limited positive approach curve (black dashed line). Interestingly, the approach curve changed from monotonically positive (orange line), positive and then negative (blue line), and monotonically negative (red line) as the lateral tip position was changed only by 10% of the tip radius beyond the boundary. The approach curve with both positive and negative feedback regions yielded a characteristic maximum around $d/a = 1.5$, which uniquely fitted with an experimental approach curve to identify the corresponding lateral position of the substrate (see below).

The finite element simulation also illustrates how the insulating groove at the boundary can be detected by intelligent topography imaging but not by widely-used constant-height imaging. When the tip approaches the insulating groove, the tip current is enhanced by the diffusion of redox molecules from the groove. Subsequently, the tip approaches closer to the groove to suppress the tip current to a preset threshold for negative approach curves (e.g., $<0.40 i_{T,\infty}$; see below). The additional tip approach below the flush gold and glass surfaces is further emphasized at the groove that is widened by the curvature of the gold surface (Figure 3-2 D). By contrast, the presence of the insulating groove is missed in the constant-height mode, where the tip is scanned at a constant height from the flush gold and glass surfaces to observe a monotonic change of the tip current over the boundary from positive feedback current to negative feedback current or vice versa (e.g., $d/a = 0.3$ in Figure 3-3).

3.3.2 Imaging Algorithm

We developed a new algorithm for non-contact and high-resolution intelligent imaging of mixed reactive and inert substrates by considering characteristic approach curves, which were simulated numerically (Figure 3-3) and confirmed experimentally (see below). The tip approach at a reactive or inert region is terminated at a short tip–substrate distance of $d/a = 0.3$, which yields tip currents of $3.0i_{T,\infty}$. (purple line in Figure 3-3) and $0.40i_{T,\infty}$ (black dotted line), respectively, to represent substrate reactivities at the constant distance. These preset values, however, can not be reached when the tip approaches the boundary (red, blue, and orange lines), thereby requiring different conditions for the termination of the tip approach. Specifically, the tip approach is terminated without the tip–substrate contact when a mildly negative approach (red line) significantly deviates from the diffusion-limited negative curve (black dotted line). This algorithm was successfully used for the intelligent imaging of insulating steps in our previous work.[14] Specifically, the tip current is measured after every step of the tip approach and compared with a theoretical value, i_T^{NF}, predicted by eq S-1, where $i_{T,\infty}$ and z tip position at $L = 0$ are obtained by fitting eq S-1 to all previous data points using the Virtual Instrument of Labview for nonlinear curve fit. A difference between experimental and theoretical currents, Δi_T, is defined as

$$\Delta i_T = i_T - i_T^{NF} \quad (3)$$

When Δi_T exceeds a preset value, the tip approach is terminated to achieve the shortest non-contact distance.

In this work, we implement two new conditions to terminate the tip approach to the boundary without contact when the tip current is enhanced monotonically (orange line in Figure

3-3) or is peaked (blue line). In the latter, the tip approach is terminated when the tip current goes below the maximum value, $i_{T,max}$, by a present value, $\Delta i_{T,max}$, to yield

$$\Delta i_{T,max} < i_{T,max} - i_T \quad (4)$$

By contrast, the termination of the tip approach is challenging when the tip current is enhanced only mildly by a positive feedback effect from the reactive side of the boundary (orange line). This challenge, however, can be overcome by detecting a sudden increase in the tip current owing to electron tunneling between the tip and the reactive edge of the substrate as found experimentally (see below). Subsequently, the tip approach is terminated when the slope of the approach curve exceeds a preset value, m_{max}, as given by

$$m_{max} < \Delta i_n/\Delta z_n \quad (5)$$

where Δi_n and Δz_n are changes in tip current and vertical tip position, respectively, after the nth step of the tip approach.

Overall, five criteria for the termination of tip approach were implemented in a new algorithm for non-contact intelligent imaging of mixed reactive/inert substrate (Figure 3-4). In this algorithm, the tip current is measured and assessed after each step of the tip approach to decide whether the tip–substrate distance is short enough to enhance or suppress the tip current, i.e., $i_T > 1.02 i_{T,\infty}$ or $i_T < 0.98\ i_{T,\infty}$, respectively. Otherwise, the tip approaches one step closer to the substrate. If the tip current is suppressed, the tip approach is terminated when the tip current reaches a threshold value, e.g., $0.40 i_{T,\infty}$, or deviates from eq S-1 (see eq 2) as introduced in our previous work.[14] Alternatively, the tip approach is terminated when the tip current is enhanced to exceed a preset current value, e.g., $3.0 i_{T,\infty}$, by the positive feedback effect, go below the maximum by a preset amount (eq 3), or increase abruptly by electron tunneling (eq 4).

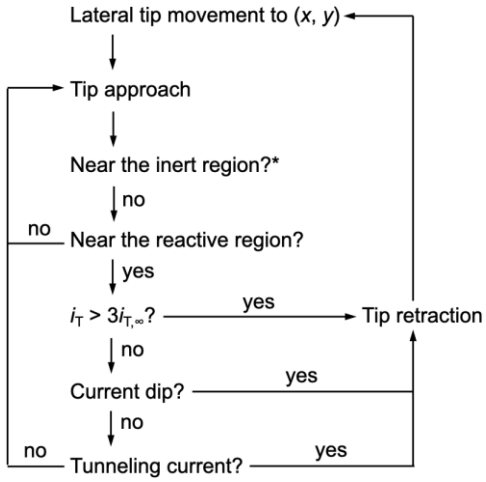

Figure 3-4 Flow chart of real-time assessment of approach curve. * See text for the algorithm when the tip approaches the inert region.

3.3.3 Intelligent Line Scan Over Interdigitated Au Electrodes

We tested the new algorithm by scanning a tip over the reactive and inert regions of interdigitated Au electrodes to separately obtain reactivity and topography information. In this line scan experiment, we aimed at observing five characteristic approach curves at the short tip–substrate distances as represented in Figure 3-3. Accordingly, the tip approach to the boundary was not terminated by the deviation of the approach curve from eq S-1 (eq 2) or the maximum of approach curve (eq 3), where the tip was still relatively far from the substrate. In these cases, the tip approach was terminated when the tunneling current was observed (eq 4) or when the tip–substrate contact was detected by assessing a change in the slope of the negative portion of the approach curve as reported previously.[14]

The tip current based on the diffusion-limited reduction of $Ru(NH_3)_6^{3+}$ was stable during the 20 minutes-long line scan to reproducibly observe five characteristic approach curves (Figure 3-5). Specifically, the tip current reached the preset thresholds of $3.0i_{T,\infty}$ and $0.4i_{T,\infty}$ (e.g., curves 1

and 2, respectively) whenever the entire surface of Pt tip approached flush Au or glass surfaces, respectively. The tip current also exceeded the former threshold when the tip approached the boundary to eventually generate tunneling current between the tip and the edge of the Au band (e.g., curve 3). When the tip approached closer to the glass side of the boundary, approach curves with a maximum were also observed (e.g., curve 4). When the tip approached even further to the glass side of the boundary, the tip experienced a mild negative feedback effect from the groove (e.g., curve 5), where the tip contacted the substrate to terminate the approach.

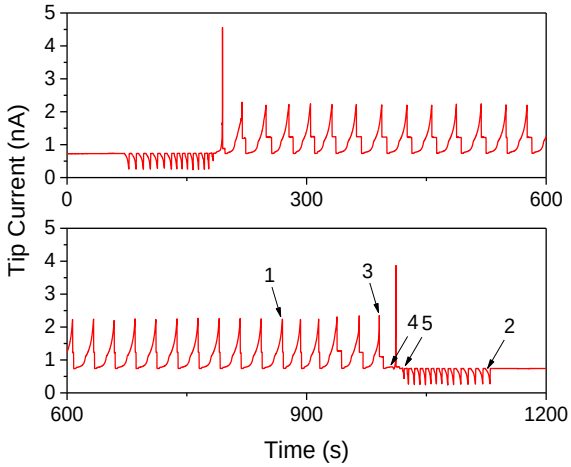

Figure 3-5 The tip current during line scan based on tip approach to Au and glass regions in 10 mM $Ru(NH_3)_6^{3+}$ and 1 M KCl. Arrows indicate characteristic approach curves shown in Figure 3-7.

In the intelligent mode, the topography of the interdigitated Au electrode was obtained by plotting the vertical tip position against the lateral tip position to reveal nanoscale grooves at both sides of a Au band (Figure 3-6 A). The grooves were observed by plotting the vertical tip position where the tip approach was terminated (black circles). Most of these tip locations are farther from the substrate because the tip approach was terminated before the tip–substrate contact. Accordingly, experimental approach curves were fitted with eqs S-1 and S-2 over glass and Au surfaces, respectively, and also with simulated curves over the boundaries (see below) to determine

the actual positions of the substrate surface under the tip (red circles). The actual topography of the substrate indicates that the tip moved more deeply into one groove than the other to even contact the grove surface, where the final tip position was below the actual grove position (curve 4). By contrast, the final tip positions at the narrower groove are only slightly below the Au surface. The width of the Au band determined from the actual topography is ~2.8 μm as expected from SEM and AFM images (Figure 3-2). The depth of the groove is also similar, i.e., ~100 nm, between the intelligent topography image and the AFM image (Figure 3-2 D).

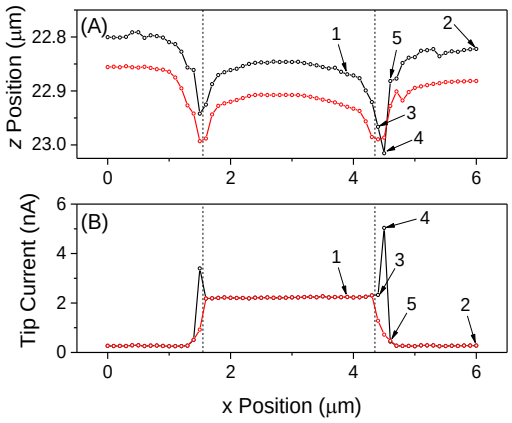

Figure 3-6 (A) The final *z* positions of approach curves (black circles) and the *z* positions of substrate determined by fitting approach curves with eq S-1 or simulated approach curves (red circles). (B) The tip current at the final *z* positions of approach curves (red circles) except for *x* = 1.5 μm and curves 3–5 (black circles), where the tip current was calculated at *d*/*a* = 0.3 from fitted approach curves (red circles).

The intelligent mode yielded the topography-independent reactivity of the substrate as represented by the tip currents of $3.0i_{T,\infty}$ or $0.40i_{T,\infty}$ at a constant distance of d/a = 0.30 over Au (curve 1 in Figure 3-6 B) or glass (curve 2) regions, respectively. In addition, the tip approach to the edge of the Au band was terminated by tunneling current (black circles for curves 3 and 4) or the tip-substrate contact (black circle for curve 5). The corresponding approach curves were fitted with simulated curves (see below) to determine the tip current at the constant distance of d/a =

0.30 from the boundary under the tip (red circles for curves 3–5). The reactivity line scan thus corrected is ideal because the corresponding tip currents were obtained or calculated at the constant distance from the substrate surface under the tip. The constant-distance line scan of substrate reactivity is independent of the topography, thereby showing no groove, which is obvious from the complementary topography line scan.

3.3.4 Characteristic Approach Curve

Five characteristic approach curves at the interdigitated Au electrodes were compared with theoretical curves to separately determine the actual position of the substrate surface under the tip for substrate topography and the tip currents at the constant distance from the local substrate surface for substrate reactivity. Negative and positive approach curves at glass and Au surfaces fitted well with eqs S-1 and S-2 (Figure 3-7 A) to represent the lowest and highest substrate reactivity, respectively. Only a mild negative feedback effect was observed when the tip approached the inert groove adjacent to the Au band (Figure 3-7 B). The experimental approach curve fitted well with an approach curve simulated for a tip approaching the inert groove. The experimental approach curve is more positive than the diffusion-limited negative approach curve. Accordingly, the tip penetrated toward the groove to reach a threshold tip current of $0.4i_{T,\infty}$, thereby manifesting the nanoscale groove in the intelligent topography line scan (Figure 3-6 A).

Interestingly, both positive and negative feedback effects were observed when the tip approached the boundary between the edge of the Au band and the insulating groove (Figure 3-7 C). Specifically, the tip current gradually increased when the tip was still far from the boundary to experience a more positive feedback effect from the Au band than a negative feedback effect from the insulating groove. As the tip approached the boundary closer, the negative feedback effect

became comparable to the positive feedback effect to reach a maximum tip current around the tip position of 22.7 μm. The negative feedback effect became dominant at shorter distances until the positive feedback effect from the side of the Au band became significant to eventually increase the tip current around the tip position of 22.9 μm. The increasing tip current, however, was lower than expected from the simulated curve, perhaps because the tip penetrated the groove to further approach the insulating surface of the groove, which is not considered in the simulation. The penetration depth reaches ~100 nm to finally observe the abrupt increase in the tip current around 23.0 μm owing to electron tunneling, which terminated the tip approach. Similarly, the lower tip current owing to the tip penetration and the abrupt increase in the tip current owing to electron tunneling was observed when the tip approached at the slightly Au side of the boundary (Figure 3-7 D), where the positive feedback effect always exceeded the negative feedback effect to monotonically increase the tip current at the shorter tip–substrate distances. In this case, the penetration depth is lower and is limited by the curvature of the Au surface.

It should be noted that a small step size of 1 nm was needed to detect a transition of the tip response from positive feedback current to tunneling current, thereby lengthening the measurement of positive approach curves (blue circles in Figure 3-7). The time of approach curve measurement was minimized by employing a custom fuzzy logic algorithm,[23] which reduces the step size as the tip approach closer to the substrate. This algorithm was used also for the measurement of negative approach curves, where only feedback currents were measured to maintain a much larger step size of down to 20 nm for faster tip approach (see blue circles in Figures 3-7 A and 3-7 B).

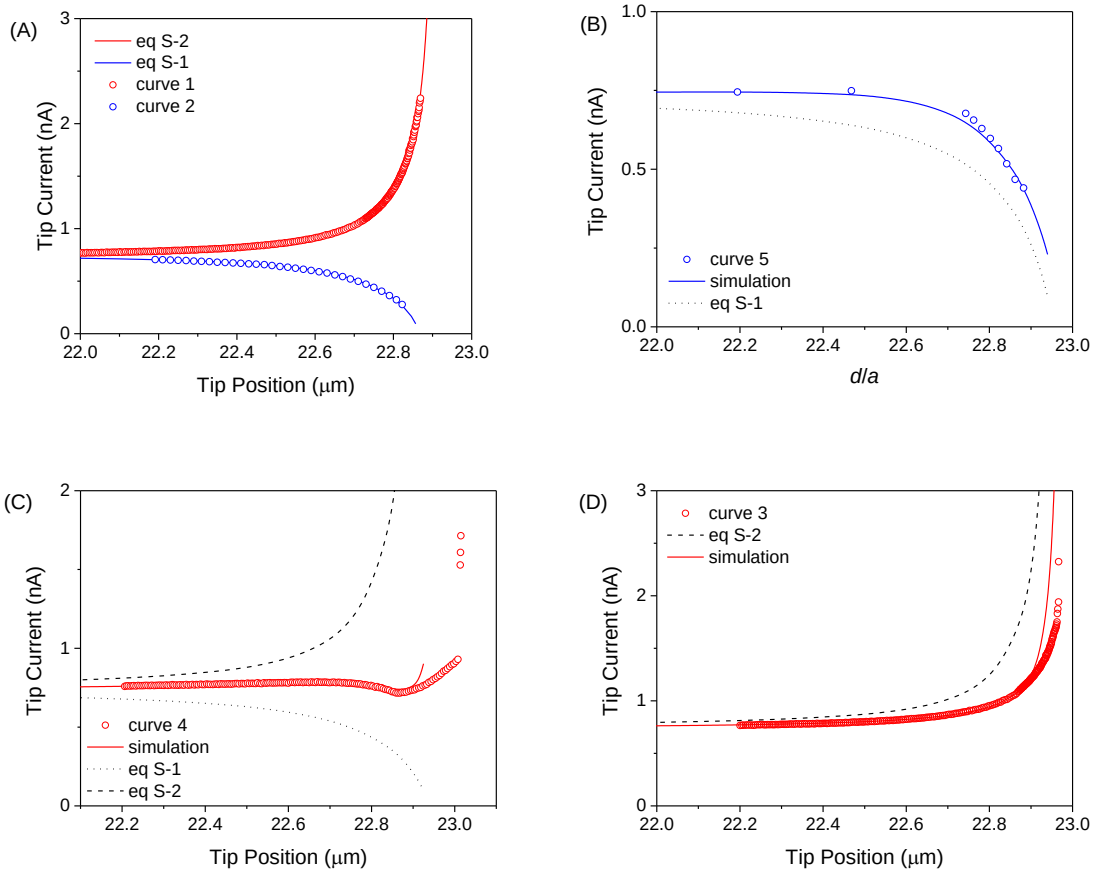

Figure 3-7 Experimental approach curves (circles) at (A) glass (blue) and Au (red) surfaces, at the insulating groove (B) far and (C) near the Au/glass boundary, and (D) the edge of the Au band in 10 mM $Ru(NH_3)_6^{3+}$ and 1 M KCl. Solid lines are simulated approach curves. Dotted and dashed lines represent diffusion-limited negative and positive approach curves.

3.3.5 Intelligent Reactivity and Topography Imaging

We employed the new algorithm to demonstrate intelligent reactivity and topography imaging without the tip–substrate contact, which can damage the tip[14] or the substrate[16] to potentially cause artifacts. The lack of tip–substrate contact was ensured by good fits between

experimental and theoretical approach curves as well as by the lack of tip damage. Intelligent reactivity and topography images of an interdigitated Au electrode (Figures 3-8 A and B, respectively) were obtained by the analysis of each approach curve to separately determine the tip current at a constant distance of $d/a = 0.3$ and the location of the substrate under the tip as illustrated above. The reactivity image demonstrates two Au bands separated by the glass surface. The Au/glass boundaries are located by the topography image, which is otherwise featureless. The consistency between reactivity and topography images is represented by their cross-sections (Figures 3-8 C and D, respectively). In the reactivity cross-section, the tip currents that are intermediate between positive and negative feedback responses were observed at boundaries (closed red circles). Correspondingly, the topography cross-section shows that the tip moved more deeply into wider grooves than narrower grooves (closed red circles). By contrast, the constant-height image of the interdigitated Au electrodes (Figure 3-8 E) shows the contrast between Au and glass surfaces but no feature of the boundaries. The cross-section of the constant-height image overlaps well with that of the intelligent reactivity image (Figure 3-8 C) to indicate the significance of the separate topography image, which manifests grooves.

It should be noted that intelligent reactivity and topography images of the interdigitated electrodes are based on feedback effects, not electron tunneling, which was used for the termination of the tip approach and excluded during post-imaging analysis. By contrast, the feedback current and tunneling current responses of a tip were used for reactivity and topography imaging, respectively, in recent work by others, thereby requiring a conductive substrate.[18] Moreover, distinguishment between feedback and tunneling currents are crucial to ensure the reliability of nanoscale SECM imaging. Recently, the constant-height image of single cubic nanoparticles was analyzed quantitatively to find that the edge of the cubic nanoparticles was too

sharp in their images to fit with the simulated images, where the edges were blurred by the mediator diffusion to resemble a hemispherical image.[20] This discrepancy was attributed to the contribution of tunneling current to the tip response, which questions whether similar images of single nanoparticles[19] based on the same experimental approach resulted from the SECM feedback effect.

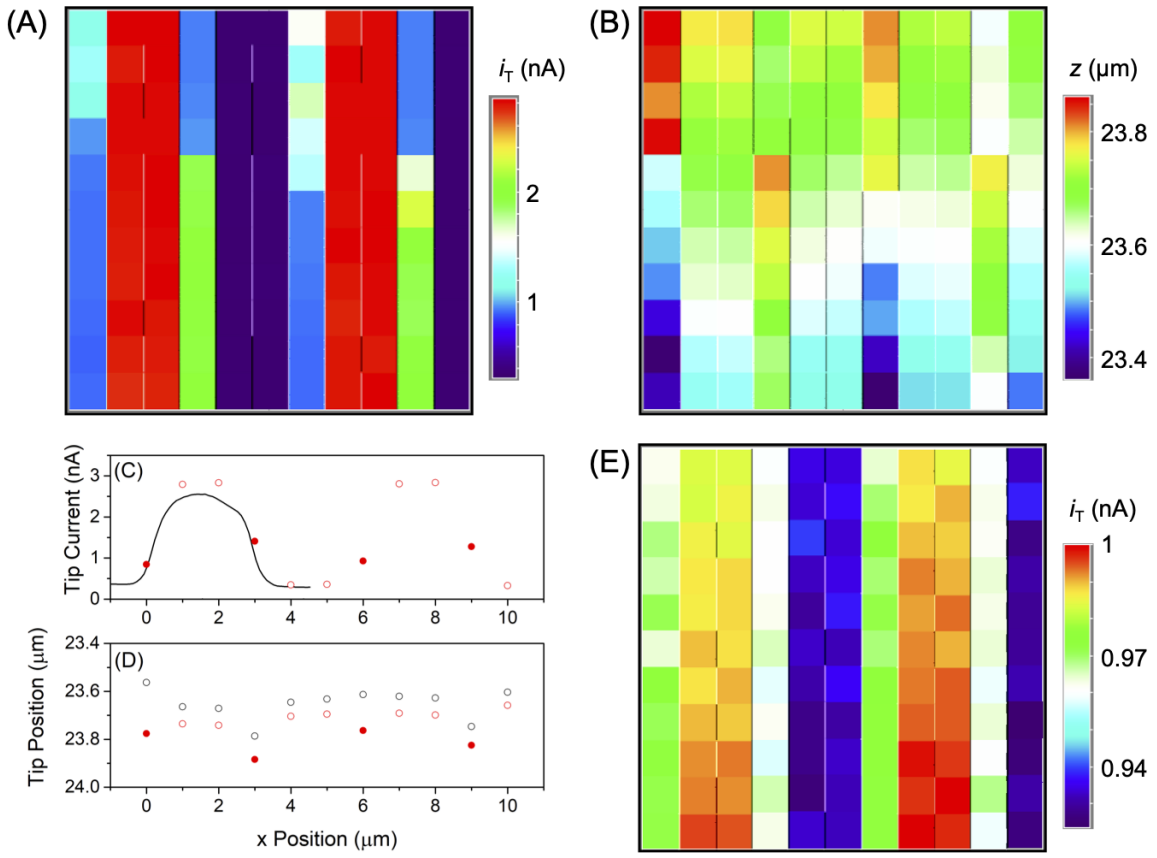

Figure 3-8 Intelligent (A) reactivity and (B) topography images of a 2.8 μm-wide Au band embedded in a glass substrate in 10 mM $Ru(NH_3)_6^{3+}$ and 1 M KCl. Each pixel is equivalent to 1 μm × 1 μm. The tip was scanned laterally from the left bottom corner and stepped upward after each line scan. The cross-sections of intelligent (C)reactivity and (D) topography images are shown in parts (A) and (B), respectively. Open and closed circles represent Au or glass surfaces and grooves, respectively. The solid line in part (C) represents the line scan of a constant-height image in part (E).

3.3.6 Tip Damage

Contact between the substrate and the nanotip can result in the damage of the fragile tip, thereby requiring non-contact imaging for nanoscale SECM. In this study, the new algorithm was developed to terminate the tip approach to the substrate before their contact, which maintained the intact nanotip before and after the non-contact imaging (Figure 3-9 A and 3-9 B, respectively). The intact tip was also protected by additional care from electrostatic discharge, which can be more serious in winter and also with a person who has a higher static charge (see Supporting Information). By contrast, a Pt nanotip (Figure 3-9 C) was cracked (Figure 3-9 D) after contact with the groove of the interdigitated Au electrode (e.g., curve 5 in Figure 3-7 B). The damage, however, was not noticeable during the intelligent line scan because the tip current did not change significantly. Similar damage of a nanotip caused by its contact with a substrate was reported previously for nanoscale intelligent imaging[14] but not for nanoscale intermittent-contact imaging,[16] which damaged the substrate.

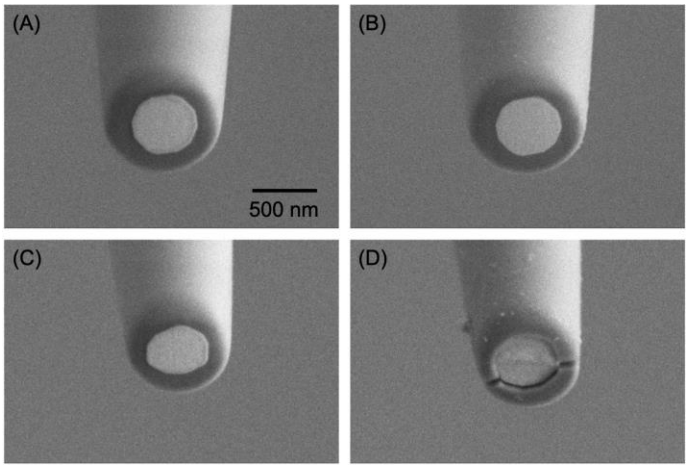

Figure 3-9 SEM images of Pt tips used for intelligent SECM imaging without (A) and (B) and with (C) and (D) tip–substrate contact. Tips immediately after FIB milling are shown in parts (A) and (C). The respective tips after intelligent imaging are shown in parts (B) and (D).

3.3.7 Imaging Time

We evaluate the intrinsically slow speed of intelligent imaging based on the measurement and assessment of each approach curve to find that the real-time analysis of a negative approach curve (eq 2) remains the slowest step ultimately, as identified in our previous work.[14] In this study, characteristic approach curves at a reactive region and its boundary with an inert region were identified theoretically (Figure 3-3) and investigated experimentally (Figures 3-7 A, C, and D). The measurement of these characteristic approach curves required a short step size of 1 nm to detect the possible transition of the tip response from positive feedback current to tunneling current without the tip–substrate contact. The subsequent time required for one step of tip approach included 25 ms for the stabilization of the piezo position and 40 ms for the measurement and assessment of the tip current (eqs 3 and 4), thereby yielding the tip approach speed of 0.015 μm/s. This speed, however, is ~100 times slower than achieved with the fastest positioning system employed for the tunneling mode of SECM, where the tip approach speed of ~2 μm/s can be accomplished with a step size of 1–2 nm without overshooting to crash the tip into the substrate.[18] By contrast the measurement of a negative approach curve uses a step size of 20 nm but requires ~60 ms for the fitting of an approach curve after each step, thereby corresponding to the maximum speed of 0.33 μm/s even by neglecting the times required for other steps, i.e, tip movement and tip current measurement.[14] The fitting time may be shortened by using a faster computing method, e.g., quantum computing.[30]

The time required for intelligent imaging will be shortened by employing a smaller tip, which requires a shorter travel distance during the tip approach. In this study, the vertical travel distance of a 500 nm-diameter tip was determined not by the roughness of the substrate, i.e., 100 nm, but by the tip diameter to measure the $i_{T,\infty}$ value at d/a = 10. Subsequently, the measurement

and assessment of each approach curve took ~30 seconds although the step size was reduced from 280 nm to 1 nm by the custom fuzzy logic algorithm only when the tip was positioned within 1 μm from the substrate (Figure 3-7). By contrast, the use of a 30 nm-diameter tip[4,5] will reduce the travel distance to 300 nm and, subsequently, shorten the imaging time by an order of magnitude. In addition, such a small tip can penetrate nanoscale gloves more deeply to determine their topography and reactivity with higher resolution. It should be noted that the steady-state current response of a smaller tip is obtained within a shorter time, which is also shorter at the reactive region than the insulator region[31] to allow for fast tip movement without a convection effect.[32]

3.4 Conclusions

In this work, the intelligent mode was developed as a powerful alternative mode of nanoscale SECM imaging[4-7] to separately visualize the reactivity and topography of non-flat substrates with both reactive and inert regions. The quantitative analysis of each approach curve constituted the quantitative topography image of the local substrate surface and the topography-independent reactivity image based on the tip current at a constant tip–substrate distance. Remarkably, intelligent topography imaging revealed nanoscale grooves as quantitatively as SEM and AFM, which contain no reactivity information. The nanoscale grooves were not noticeable in the constant-height SECM image, which only resembles the intelligent reactivity image. The continuous change in the constant-distance tip current in the intelligent reactivity image confirms that the constant-current imaging of the boundary between reactive and inter regions is impossible.[9] Moreover, the short tip–substrate distances of the intelligent mode yields high spatial resolution (eq 1) in comparison with the long tip–substrate distances of the hopping mode[17] and

also ensures the lack of the tip–substrate contact in contrast to the intermittent-contact mode,[16] which can damage the substrate (and potentially the tip) to cause artifacts. In this study, the reactivity of a large unbiased conductor was diffusion-limited,[33,34] thereby requiring nanoscale voltammetric characterization to determine the local kinetics of substrate reactivity.[35]

Uniquely, we employed both feedback and tunneling modes of SECM to enable the intelligent reactivity and topography imaging of substrates with both reactive and inert regions. The tunneling mode was employed only to terminate the tip approach to the edge of a reactive region by detecting the transition of the tip response from positive feedback current to tunneling current. Otherwise, the feedback tip current was monitored and used to terminate the tip approach, thereby enabling the intelligent imaging of both conductive and insulating regions as well as their boundaries. By contrast, a recent study employed feedback and tunneling modes for reactivity and topography imaging, respectively, thereby requiring a conductive substrate.[18] In addition, we analyzed each approach curve theoretically to ensure that reactivity and topography images are based on the feedback mechanism, not the tunneling mechanism. By contrast, constant-height imaging can not distinguish between feedback[19] and tunneling[20] mechanisms. Overall, the intelligent mode serves as a versatile and reliable mode of nanoscale SECM imaging.

3.5 Supporting Information

3.5.1 Theorical Approach Curves

Diffusion-limited positive and negative approach curves were represented by approximate equations. Specifically, the tip current based on the negative feedback effect was given by[36]

$$\frac{i_T^{NF}}{i_{T,\infty}} = \frac{\frac{2.08}{RG^{0.358}}\left(L-\frac{0.145}{RG}\right)+1.585}{\frac{2.08}{RG^{0.358}}(L+0.0023RG)+1.57+\frac{lnRG}{L}+\frac{2}{\pi RG}ln\left(1+\frac{\pi RG}{2L}\right)} \quad \text{(S-1)}$$

where L (= d/a) is the normalized tip–substrate distance, RG (= r_g/a) is the normalized tip outer diameter. The positive feedback effect on the tip current was represented by[37]

$$\frac{i_T^{PF}}{i_{T,\infty}} = \alpha + \frac{\pi}{4\beta arctan(L)} + \left(1-\alpha-\frac{1}{2\beta}\right)\frac{2}{\pi}arctan(L) \quad \text{(S-2)}$$

with

$$\alpha = ln2 + ln2\left[1-\frac{2}{\pi}acrcos\left(\frac{1}{RG}\right)\right] - ln2\left\{1-\left[\frac{2}{\pi}arccos\left(\frac{1}{RG}\right)\right]^2\right\} \quad \text{(S-3)}$$

$$\beta = 1 + 0.639\left[1-\frac{2}{\pi}acrcos\left(\frac{1}{RG}\right)\right] - 0.186\left\{1-\left[\frac{2}{\pi}arccos\left(\frac{1}{RG}\right)\right]^2\right\} \quad \text{(S-4)}$$

3.5.2 Finite Element Simulation

The limiting current at a disk-shaped tip in the SECM configuration was simulated by solving a three-dimensional (3D) diffusion problem with an array of microbands on the insulating substrate as defined in Cartesian coordinates (Figure 3-11). The origin of the coordinate axis was set at the center of a microband. The width, w, of a microband was determined from SEM images of the substrate (Figure 3-2). Initially, the solution contained redox-active species, O, at a bulk concentration of c_0. The same diffusion coefficient, D, was assumed for both species O and its product, R, to yield the steady-state diffusion of species O in solution as defined by

$$\frac{\partial c}{\partial t} = D\left(\frac{\partial^2 c}{\partial x^2}+\frac{\partial^2 c}{\partial y^2}+\frac{\partial^2 c}{\partial z^2}\right) = 0 \quad \text{(S-5)}$$

where c is the ion concentration at (x, y, z). The zero concentration of redox species was the boundary condition of the tip. The tip-generated species, R, is immediately oxidized to O at the

microband surface, where the boundary condition is the bulk concentration of R, i.e., c_0. The insulating substrate yielded zero flux perpendicular to these boundaries. Boundary conditions at simulation space limits were the bulk concentration of redox species, c_0.

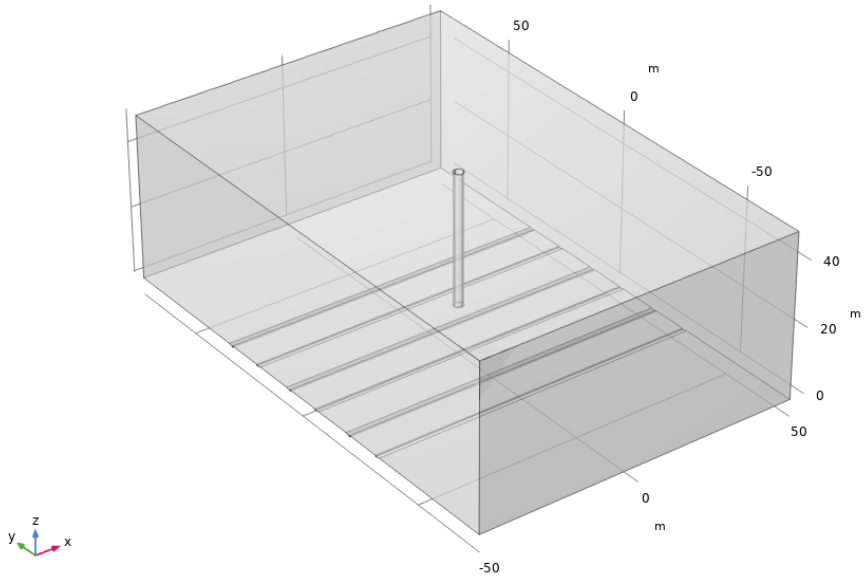

Figure 3-10 Scheme for the finite element simulation of an SECM diffusion problem with a disk tip positioned over an array of microband electrodes embedded in the insulating substrate.

We employed COMSOL Multiphysics (version 5.4a, COMSOL, Inc., Burlington, MA) to solve the 3D SECM diffusion problem in dimensionless form. Eq S-1 was defined by dimensionless parameters as

$$\frac{\partial C}{\partial t} = \left(\frac{\partial^2 C}{\partial X^2} + \frac{\partial^2 C}{\partial Y^2} + \frac{\partial^2 C}{\partial Z^2} \right) = 0 \quad \text{(S-6)}$$

where

$$C = \frac{c}{c_0} \quad \text{(S-7)}$$

$$t = \frac{4Dt}{a^2} \quad \text{(S-8)}$$

$$X = \frac{x}{a} \quad \text{(S-9)}$$

$$Y = \frac{y}{a} \quad \text{(S-10)}$$

$$Z = \frac{z}{a} \quad \text{(S-11)}$$

In addition, dimensionless geometric parameters were defined for protrusions (or recessions) as

$$W = \frac{w}{a} \quad \text{(S-12)}$$

$$H = \frac{h}{a} \quad \text{(S-13)}$$

This problem was solved numerically (Figure 3-11) to calculate the normalized tip current, $i_T/i_{T,\infty}$, which was set to 1 at $L = 30$.

The reliability of simulated approach curves was ensured by using eqs S-1 and S-2. When the entire Pt tip approached the insulating region of the inert surface far from the groove, the simulated tip current fitted well with the tip current based on the diffusion-limited negative feedback effect (eq S-1). Moreover, the simulated tip current over the middle of conductive regions agreed with the tip current based on the diffusion-limited positive feedback effect (eq S-2).

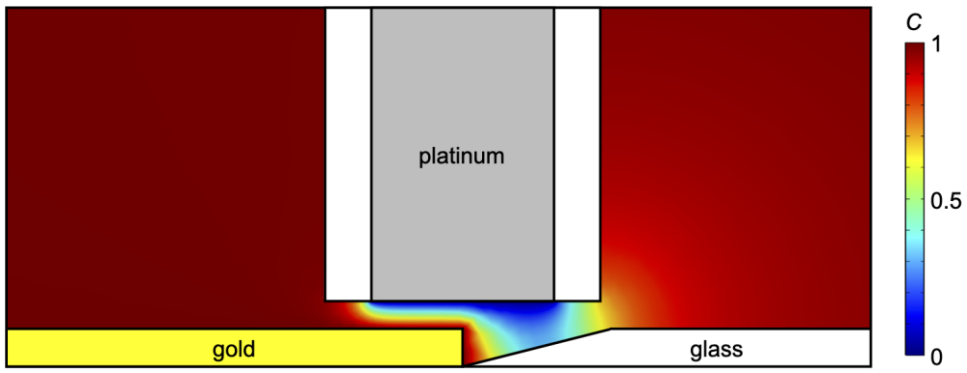

Figure 3-11 Simulated concentration profile around a Pt tip positioned over the boundary between Au band and grooved glass.

3.5.3 Prevention of Electrostatic Tip Damage

Protections were needed to prevent the electrostatic damage of Pt nanotips in winter. Specifically, we handled the tips in the foggy environment created by an ultrasonic humidifier (Figures 3-12 A and 3-12 B) to prevent the electrostatic damage of the nanotips. A cool-mist humidifier was also used (Figures 3-12 C and 3-12 D) to achieve a similar humidity but no fog, which resulted in the tip damage (Figures 3-12 E and 3-12 F). The surface of items in the plexiglass box was wet with the ultrasonic humidifier but not with the cool-mist humidifier.

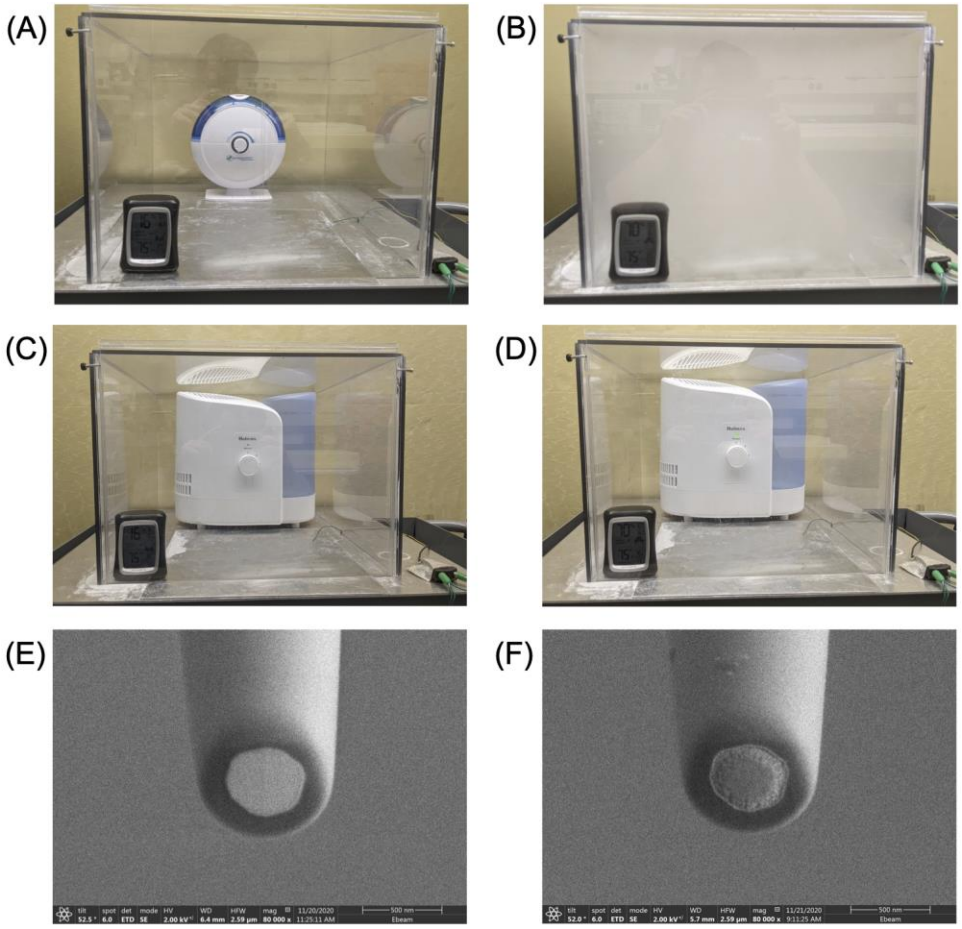

Figure 3-12 Photos of (A) and (B) ultrasonic and (C) and (D) cool-mist humidifiers in a plexiglass box, where Pt tips were handled. The low humidity of 16 % in (A) and (C) increased to 70% in (B) and (D) when the humidifiers were turned on. SEM images of the tip (E) before and (F) after handled in the plexiglass box with the cool-mist humidifier.

We also made additional changes in our practice. We stored Pt tips in the grounded metal box, not in the conductive plastic box (Figure 3-14 A). Moreover, dissipative fingercots (8C, QPR Gloves, Latham, NY) were worn to attach an alligator clip to the electrode lead (Figure 3-13 B).

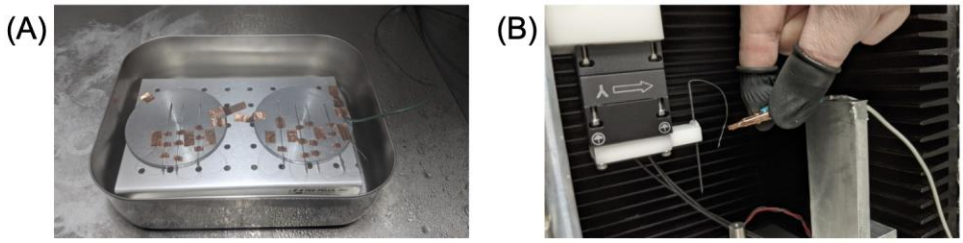

Figure 3-13 Photos of (A) a metal box for tip storage and (B) dissipative fingercots for handling electrode leads.

3.6 Acknowledgements

This work was supported by the Army Research Office Young Investigator Grant No. 66446-CH-YIP (Award Number W911NF-17-1-0098). S.A. acknowledges supports from the National Science Foundation (CHE-1904258) and the National Institutes of Health (R01 GM112656).

3.7 References

(1) Amemiya, S., Nanoscale scanning electrochemical microscopy. In *Electroanalytical chemistry*, Bard, A. J.; Zoski, C. G., Eds. CRC Press: 2015; pp 1-72.

(2) Kai, T.; Zoski, C. G.; Bard, A. J. *Chem. Commun.* **2018**, *54*, 1934-1947.

(3) Kwak, J.; Bard, A. J. *Anal. Chem.* **1989**, *61*, 1794–1799.

(4) Shen, M.; Ishimatsu, R.; Kim, J.; Amemiya, S. *J. Am. Chem. Soc.* **2012**, *134*, 9856-9859.

(5) Chen, R.; Balla, R. J.; Lima, A.; Amemiya, S. *Anal. Chem.* **2017**, *89*, 9946-9952.

(6) Kim, J.; Renault, C.; Nioradze, N.; Arroyo-Currás, N.; Leonard, K. C.; Bard, A. J. *J. Am. Chem. Soc.* **2016**, *138*, 8560–8568.

(7) Kim, J.; Renault, C.; Nioradze, N.; Arroyo-Currás, N.; Leonard, K. C.; Bard, A. J. *Anal. Chem.* **2016**, *88*, 10284-10289.

(8) Amemiya, S.; Guo, J.; Xiong, H.; Gross, D. A. *Anal. Bioanal. Chem.* **2006**, *386*, 458–471.

(9) Wipf, D. O.; Bard, A. J.; Tallman, D. E. *Anal. Chem.* **1993**, *65*, 1373–1377.

(10) Fan, F.-R. F.; Bard, A. J. *Proc. Natl. Acad. Soci. U.S.A.* **1999**, *96*, 14222–14227.

(11) Laforge, F. O.; Velmurugan, J.; Wang, Y.; Mirkin, M. V. *Anal. Chem.* **2009**, *81*, 3143-3150.

(12) O'Connell, M. A.; Wain, A. J. *Analytical Methods* **2015**, *7*, 6983-6999.

(13) Lazenby, R. A.; McKelvey, K.; Unwin, P. R. *Anal. Chem.* **2013**, *85*, 2937-2944.

(14) Balla, R. J.; Jantz, D. T.; Kurapati, N.; Chen, R.; Leonard, K. C.; Amemiya, S. *Anal. Chem.* **2019**, *91*, 10227-10235.

(15) Bard, A. J.; Mirkin, M. V.; Unwin, P. R.; Wipf, D. O. *J. Phys. Chem.* **1992**, *96*, 1861–1868.

(16) Lazenby, R.; McKelvey, K.; Peruffo, M.; Baghdadi, M.; Unwin, P. R. *J. Solid State Electrochem.* **2013**, *17*, 2979-2987.

(17) Jedraszko, J.; Michalak, M.; Jönsson-Niedziolka, M.; Nogala, W. *J. Electroanal. Chem.* **2018**, *815*, 231-237.

(18) Edmondson, J. F.; Meloni, G. N.; Costantini, G.; Unwin, P. R. *ChemElectroChem* **2020**, *7*, 697-706.

(19) Sun, T.; Yu, Y.; Zacher, B. J.; Mirkin, M. V. *Angew. Chem. Int. Ed.* **2014**, *53*, 14120-14123.

(20) Blanchard, P.-Y.; Sun, T.; Yu, Y.; Wei, Z.; Matsui, H.; Mirkin, M. V. *Langmuir* **2016**, *32*, 2500-2508.

(21) Nioradze, N.; Chen, R.; Kurapati, N.; Khyataeva-Domanov, A.; Mabic, S.; Amemiya, S. *Anal. Chem.* **2015**, *87*, 4836-4843.

(22) Pathirathna, P.; Balla, R. J.; Jantz, D. T.; Kurapati, N.; Gramm, E. R.; Leonard, K. C.; Amemiya, S. *Anal. Chem.* **2019**, *91*, 5446-5454.

(23) Barforoush, J. M.; McDonald, T. D.; Desai, T. A.; Widrig, D.; Bayer, C.; Brown, M. K.; Cummings, L. C.; Leonard, K. C. *Electrochim. Acta* **2016**, *190*, 713-719.

(24) Kim, J.; Shen, M.; Nioradze, N.; Amemiya, S. *Anal. Chem.* **2012**, *84*, 3489-3492.

(25) Nioradze, N.; Kim, J.; Amemiya, S. *Anal. Chem.* **2011**, *83*, 828-835.

(26) Kim, J.; Izadyar, A.; Nioradze, N.; Amemiya, S. *J. Am. Chem. Soc.* **2013**, *135*, 2321-2329.

(27) Nioradze, N.; Chen, R.; Kim, J.; Shen, M.; Santhosh, P.; Amemiya, S. *Anal. Chem.* **2013**, *85*, 6198-6202.

(28) Kim, J.; Kim, B.-K.; Cho, S. K.; Bard, A. J. *J. Am. Chem. Soc.* **2014**, *136*, 8173-8176.

(29) Chen, R.; Balla, R. J.; Li, Z. T.; Liu, H. T.; Amemiya, S. *Anal. Chem.* **2016**, *88*, 8323-8331.

(30) Wiebe, N.; Braun, D.; Lloyd, S. *Phys. Rev. Lett.* **2012**, *109*, 050505.

(31) Bard, A. J.; Denuault, G. H.; Friesner, R. A.; Dornblaser, B. C.; Tuckerman, L. S. *Anal. Chem.* **1991**, *63*, 1282–1288.

(32) Cornut, R.; Poirier, S.; Mauzeroll, J. *Anal. Chem.* **2012**, *84*, 3531-3537.

(33) Wipf, D. O.; Bard, A. J. *J. Electrochem. Soc.* **1991**, *138*, 469–474.

(34) Xiong, H.; Guo, J.; Amemiya, S. *Anal. Chem.* **2007**, *79*, 2735–2744.

(35) Chen, R.; Najarian, A. M.; Kurapati, N.; Balla, R. J.; Oleinick, A.; Svir, I.; Amatore, C.; McCreery, R. L.; Amemiya, S. *Anal. Chem.* **2018**, *90*, 11115-11123.

(36) Cornut, R.; Lefrou, C. *J. Electroanal. Chem.* **2007**, *608*, 59.

(37) Lefrou, C. *J. Electroanal. Chem.* **2006**, *592*, 103.

4.0 Simulation of Fast-Scan Nanogap Voltammetry at Double-Cylinder Ultramicroelectrodes

This thesis author contributed to the development of the finite element simulation, which models the electrochemical responses of the nanogap electrode system discovered by the author. The author's design of the double carbon fiber ultramicroelectrodes separated by a nanogap is proposed in this chapter to justify the double cylinder geometry of the simulation model.

4.1 Introduction

Fast-scan cyclic voltammetry (FSCV) is a powerful electrochemical method to monitor rapid dynamics of heterogeneous electron transfer[1] and neurotransmitter release[2] at high temporal resolution. FSCV at >100 V/s is routinely used for real-time monitoring of neurotransmitters in the brain at sub-millisecond resolution.[3] Ultra-FSCV at ~10^6 V/s was developed to resolve the kinetics of extremely fast electrode reactions at nanosecond resolution.[4] Faster potential scan, however, linearly increases a background current based on double-layer charging at the electrode/solution interface[5] and electrolysis of the electrode surface.[6] The transient background is

suppressed by using a ultramicroelectrode (UME) to minimize the *iR* drop, but often exceed a response to the diffusing redox species. This diffusional response also becomes transient with fast scan, but grows only with the square-root of scan rate.[7] Accordingly, FSCV is typically used for the study of redox molecules adsorbed on[3] or tethered to[4] the electrode surface to yield a transient response that is proportional to scan rate.[6] A background voltammogram, however, must be subtracted for quantitative FSCV, which is limited to differential measurement of concentration changes in vivo.[8]

Herein, we report on finite element simulation of fast-scan nanogap voltammetry (FSNV) to quantitatively detect diffusing redox species at high temporal resolution of FSCV without the need of background subtraction. Specifically, we simulate diffusional redox cycling across a nanometer-wide gap between a parallel pair of cylindrical UMEs with identical sizes (Figure 4-1). With this setup, the generator electrode voltammetrically electrolyzes a redox reactant, O, at a fast scan rate to obtain a current response with the high background. By contrast, a constant potential is applied to the collector electrode to amperometrically detect the product, R, without the transient background. Subsequently, background subtraction is not needed for quantitative analysis of a nanogap voltammogram based on the amperometric collector response against the cycled generator potential.[9,10] Only slow scan at $\leq$0.1 V/s, however, has been used to characterize nanogap electrochemical cells.[11,12] Moreover, double-cylinder UMEs only with micrometer-wide gaps have been reported[13-15] to assess steady-state theories[16,17] at slow scan rates.

In this work, we predict that quasi-steady states are achieved by FSNV of diffusing redox species at up to hundreds volts and megavolts per second using double-microcylinder and nanocylinder UMEs, respectively. We adapt a previous model of chronoamperometry[18] for FSNV to reveal that local redox cycling between nanogap sides of double-cylinder electrodes (red and

blue arrows in Figure 4-1 A) quickly reaches quasi-steady states to allow for fast scan while a voltammetric response at the solution side of the generator electrode (black arrows) is still transient. A quasi-steady-state collector response is determined by a ratio between gap width and cylinder radius and can be enhanced by using longer cylinders even with a smaller radius to facilitate fast current measurement. Simulation results are obtained using general dimensionless parameters[18] and related to actual currents, scan rates, and sizes for double-cylinder UMEs that we propose to fabricate from double-disk-like UMEs.[19,20] The proposed method requires neither nanolithography[21,22] nor nanoscale scanning electrochemical microscopy (SECM)[23,24] in contrast to other nanogap cells[11,12] to widen the application of nanogap voltammetry.

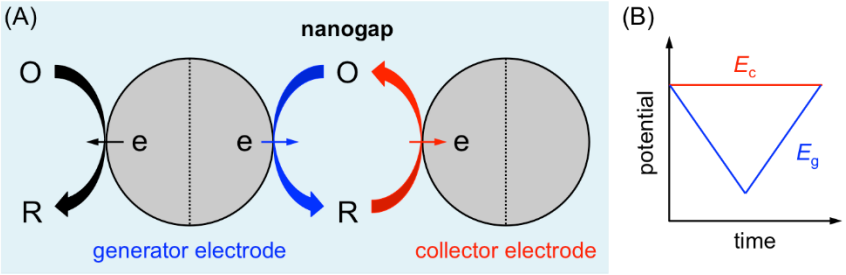

Figure 4-1 (A) Orthogonal cross-section of a parallel pair of cylindrical UMEs with the identical radius and length as voltammetric generator and amperometric collector electrodes in a solution containing a redox species, O. Dotted lines separate nanogap and solution sides of each electrode. Blue and red arrows indicate redox cycling between nanogap sides of the double-cylinder UMEs. Black arrows indicate the electrolysis of the original redox species at the solution side of the generator electrode. (B) Potentials of generator and collector electrodes, *Eg* and *Ec*, respectively, during FSNV.

Table 4-1 Geometric Parameters and Scan Rates for FSNV Simulation.

UME	*r*	*g*		v^a		
		$G = 0.1$	$G = 1$	$\sigma = 300$	$\sigma = 3$	$\sigma = 0.03$
double microcylinder	3.5 µm	0.35 µm	3.5 µm	400 V/s	4 V/s	0.04 V/s

double nanocylinder	**35 nm**	**3.5 nm**	**35 nm**	**4 MV/s**	**40 kV/s**	**400 V/s**

[a] Calculated by solving eq 9 with $D = 6 \times 10^{-6}$ cm^2/s.

4.2 Model

Here, we consider FSNV at a parallel pair of cylindrical electrodes with the identical radius, *r*, and length, *L*, and a narrow separation, *g* (Figure 4-6 in Supplementary Material). Geometrically, our model is equivalent to the model used for simulation of chronoamperometry at double-hemi-cylinder electrodes[18] owing to the symmetry of double-cylinder electrodes with respect to the *x*-axis. In this work, we simulate voltammetric responses not only at generator and collector electrodes, but also at nanogap and solution sides of each electrode (Figure 4-1) in contrast to the previous study.[18]

We employ a commercial package for finite element simulation (COMSOL version 5.3a, COMSOL, Burlington, MA) to solve a 2D diffusion problem at double-cylinder electrodes in the solution containing a redox species, O. This reactant participates in a *n*-electron transfer reaction as given by

$$\mathrm{O} + n\mathrm{e} \rightleftharpoons \mathrm{R} \quad (1)$$

We assume the identical diffusion coefficient, *D*, for species O and R so that the diffusion problem needs to be solved only for the reactant. Diffusional mass transport of the reactant is represented by

$$\partial c_\mathrm{O}/\partial t = D(\partial^2 c_\mathrm{O}/\partial x^2 + \partial^2 c_\mathrm{O}/\partial y^2) \quad (2)$$

where c_O is the local concentration of the reactant at (x, y) in solution. The reactant is voltammetrically electrolyzed at the generator electrode to yield the boundary condition based on the Butler–Volmer kinetics[25] as

$$D(\partial c_O/\partial \boldsymbol{n}) = -v_{et} \quad (3)$$

with

$$v_{et} = k^0\{c_O\exp[-\alpha nF(E_g - E^{0'})/RT] - (c_0 - c_O)\exp[(1-\alpha)nF(E_g - E^{0'})/RT] \quad (4)$$

where $\boldsymbol{n}$ is a vector with a length of r and is normal to the surface of the generator electrode at the point of interest, v_{et} is the heterogeneous electron-transfer rate, k^0 is the heterogeneous standard electron-transfer rate constant, α is transfer coefficient, E_g is the potential of the generator electrode, $E^{0'}$ is the formal potential of the redox couple, and c_0 is the bulk concentration of the reactant, O. We employ large k^0 values to obtain reversible voltammetric responses at generator and collector electrodes unless mentioned otherwise.

We simulate current responses at generator and collector electrodes, i_g and i_c, respectively, by solving eq 2 with boundary conditions including eq 3 at the generator electrode. The boundary condition for diffusion-limited regeneration of the reactant at the collector electrode is given by

$$c_O = c_0 \quad (5)$$

This boundary condition implies that the potential of the collector electrode, E_c, is positive enough with respect to $E^{0'}$. Other boundary conditions are shown in Figure 4-6 (Supplementary Material). We employ dimensionless parameters (Supplementary Material and Results and Discussion) to simulate normalized currents at generator and collector electrodes, I_g and I_c, respectively, as given by[18]

$$I_g = i_g/nFDLc_0 \quad (6)$$

$$I_c = i_c/nFDLc_0 \quad (7)$$

Normalized currents at nanogap and solution sides of generator and collector electrodes are also simulated. The reliability of our simulation was validated for chronoamperometry at single-cylinder UMEs[26] as reported in the previous study[18] (Supplementary Material).

4.3 Results and Discussion

4.3.1 Scan Rates and Geometric Parameters

In this work, we consider double-cylinder UMEs with a micrometer or nanometer radius and a nanometer-wide gap to simulate quasi-steady-state FSNV at up to hundreds volts or megavolts per second, respectively. The gap width is normalized against the cylinder radius to yield one of key dimensionless parameters[18] as

$$G = g/r \quad (8)$$

Another key dimensionless parameter is the normalized scan rate given by

$$\sigma = r^2 nFv/DRT \quad (9)$$

where v is the scan rate of generator potential. Actual cylinder radii are used to calculate gap widths and scan rates from the corresponding dimensionless parameters (Table 4-1).

We consider the radii and gap widths of double-cylinder UMEs (Table 4-1) that we propose to fabricate from double-disk-like UMEs. Specifically, a pair of independent carbon-disk UMEs with gap distances of <1 μm was fabricated by filling each channel of a theta glass capillary with a carbon fiber, pulling the assembly using a pipet puller with a heating coil, and mechanically polishing the tip end.[19] The glass sheath of double-disk carbon-fiber UMEs may be etched in a HF solution to expose double-microcylinder UMEs with a desirable length. A typical carbon-fiber

radius of 3.5 μm[3] is considered in our model to yield a gap width of 0.35 μm with G = 0.1. Similarly, double-microcylinder UMEs with wider gaps (G = 1) may be fabricated from double-disk carbon-fiber UMEs with micrometer-wide gaps,[19,27] which are too wide to establish redox cycling for FSNV (see below).

We also propose that double-nanocylinder UMEs with nanogaps may be fabricated from double carbon nanoelectrodes obtained by pyrolysis of a carbon source inside a theta quartz nanopipet.[20] Double-nanocylinder UMEs may be obtained by etching the insulating sheath of double carbon nanoelectrodes in a HF solution as demonstrated for fabrication of single-cone carbon nanoelectrodes with precisely controlled lengths of 5 μm–175 μm.[28] The geometry of double carbon nanoelectrodes is semielliptical[20] and tapered,[28] but idealized in our model to yield a pair of 35 nm-radius cylinders with a gap width of G = 0.1 or 1. A narrow gap width of 3.5 nm with G = 0.1 is still wide enough to prevent direct electron tunneling between generator and collector electrodes.[29] Our simple model neglects long-range electron transfer through redox species in the narrow gap[30] and the migration of redox species through electrical double layers at the electrodes.[12]

Simulation of FSNV at double-microcylinder and nanocylinder UMEs employs the identical σ values of 300, 3, and 0.03, which correspond to very different scan rates for the respective UMEs (Table 4-1). The highest σ value of 300 is equivalent to a fast scan rate of 400 V/s at the double-microcylinder UMEs as practiced for in-vivo FSCV with single carbon-fiber UMEs.[3] By contrast, the highest σ value at the double-nanocylinder UMEs reaches an ultrafast scan rate of 4 MV/s, which is the highest scan rate achieved for FSCV by using single disk UMEs.[31,32] Accordingly, the lowest σ value of 0.03 at the double-nanocylinder UMEs maintains a fast scan rate of 400 V/s as realized for in-vivo FSCV using single-cone carbon nanoelectrodes.[28]

By comparison, the same σ value yields a slow scan rate of 0.04 V/s for the double-microcylinder UMEs as typically employed for nanogap voltammetry.[11,12]

It should be noted that the normalized scan rate is related to the normalized duration of the entire simulation, τ_e, given by eq S-3 in Supplemental Material as

$$\tau_e = 2F\Delta E/\sigma RT \quad (10)$$

where ΔE is a difference between initial and switching potentials. Eq 10 with ΔE = 0.5 V yields τ_e = 0.13, 13, and 1300 for σ = 300, 3, and 0.03, respectively. These time regimes match those examined in the previous study of double-hemi-cylinder electrodes,[18] where chronoamperograms were reported at τ_e values of up to 10 and at steady states (i.e., $\tau_e \to \infty$). Our simulation of FSNV, however, provides a new insight that the collector electrode reaches quasi-steady states much faster than the generator electrode to allow for fast scan (see below).

4.3.2 FSNV at Double-Cylinder UMEs with Narrow Gaps (G=0.1)

We employed the finite element method to demonstrate that quasi-steady-state FSNV is enabled even at σ = 300 when the gap of double-cylinder UMEs is narrow, i.e., G = 0.1 (Figure 4-2 A). This σ value corresponds to 400 V/s and 4 MV/s at 3.5 μm- and 35 nm-radii cylinder electrodes, respectively (Table 4-1). At σ = 300, the collector electrode yielded a limiting current during the reverse scan (red dashed line) to ensure quasi-steady states despite large hysteresis in comparison with the forward wave (red solid line). This hysteresis is due to the finite time required for the redox product, R, to diffuse from the generator electrode to the collector electrode across the gap (Figure 4-1 A). In fact, the collector response was delayed from the generator response during the forward scan (blue solid line). Noticeably, peak-shaped transient responses were

obtained at the generator electrode even during the reverse scan (blue dashed line), thereby indicating that only the collector response reached quasi-steady states at $\sigma = 300$.

An intermediate scan rate of $\sigma = 3$ also yielded a quasi-steady-state voltammogram with small hysteresis at the collector electrode in addition to a peaked-shape transient voltammogram at the generator electrode (Figure 4-2 B). This slower scan rate is still relevant to FSNV, because it corresponds to a fast scan rate of 40 kV/s at 35 nm-radius double-cylinder UMEs with a 3.5 nm-wide gap (Table 4-1). The normalized limiting current at the collector electrode changed only by ~25% from –3.5 to –4.4 as σ decreased by two orders of magnitude from 300 to 3. The scan-rate dependence of the limiting current is weak and opposite to that of a transient response, thereby ensuring quasi-steady states at the collector electrode. By contrast, the generator response was transient during the entire potential cycle as indicated by the peak-shaped negative response during the reverse scan as well as by lower peak currents at $\sigma = 3$ than at $\sigma = 300$. Again, only the collector electrode reached quasi-steady states at $\sigma = 3$.

Quasi-steady state responses were obtained at both generator and collector electrodes with $\sigma = 0.03$ (Figure 4-2 C) to demonstrate that the collector electrode reached quasi-steady states ~10^4 times faster ($\sigma = 300$) than the generator electrode. A low σ value of 0.03 still corresponds to a fast scan rate of 400 V/s at the double-nanocylinder UMEs (Table 4-1). The slow scan rate yielded a high collection efficiency of 0.90 as defined by an absolute ratio of a normalized limiting current of –4.7 at the collector electrode with respect to that of 5.2 at the generator electrode. High collection efficiency at the slow scan rate is anticipated form the previous simulation study,[18] which yielded high collection efficiency at steady states. Importantly, our simulation revealed that lower collection efficiency at faster scan rates (or shorter time regimes) is mainly due to a larger

transient response of the generator electrode and is irrelevant to FSNV, which measures a quasi-steady-state collector response.

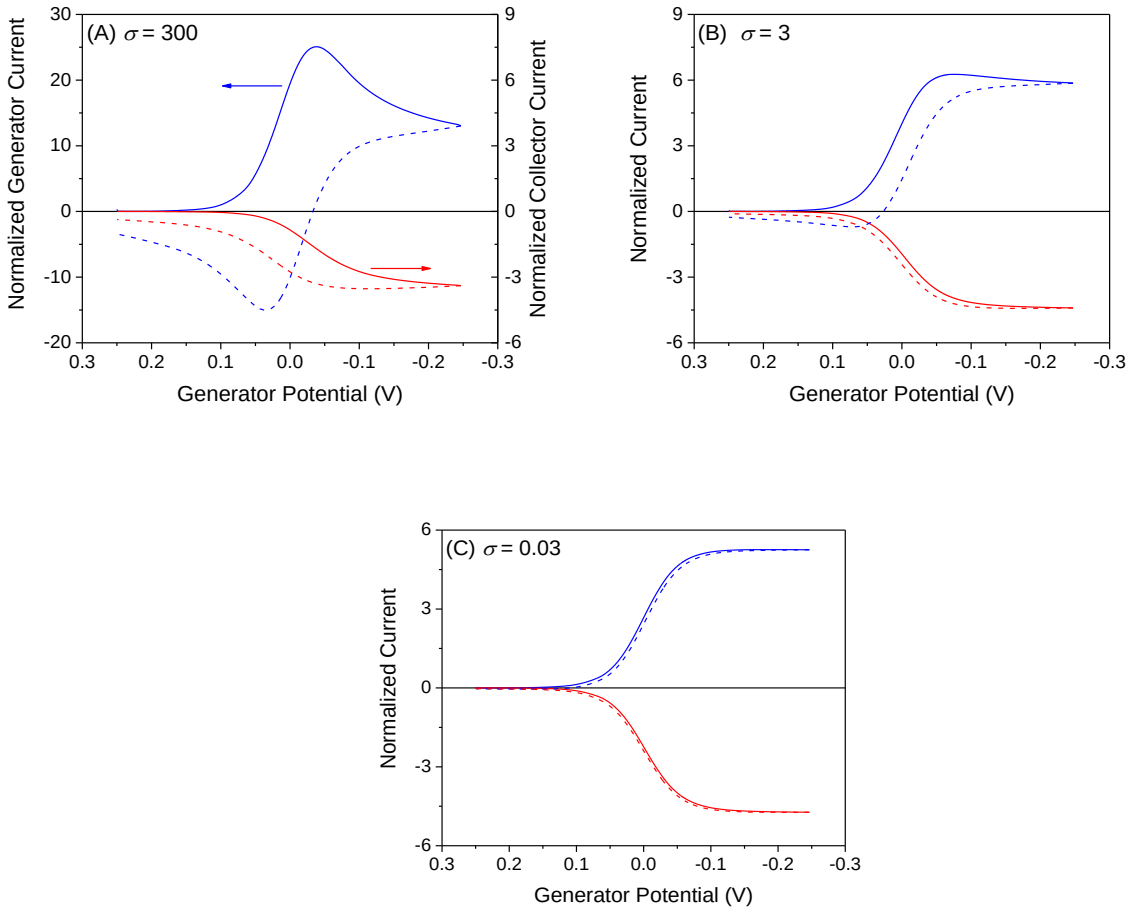

Figure 4-2 Voltammetric responses of generator (blue) and collector (red) electrodes with narrow gaps (G = 0.1) during forward (solid) and reverse (dashed) scans of generator potential.

4.3.3 Current Distributions at Generator and Collector Electrodes with Narrow Gaps (G=0.1)

Voltammetric responses at nanogap and solution sides of generator and collector electrodes with $G = 0.1$ were simulated to demonstrate that the collector response reaches quasi-steady states much faster than the generator response because of the slow decay of the current response at the

solution side of the generator electrode. The normalized current at each side of generator and collector electrodes (Figure 4-1 A) was simulated against generator potential to yield a pair of voltammograms for each electrode at σ = 300, 3, and 0.03 (Figures 4-3 A, 4-3 C, and 4-3 E, respectively). In these plots, the polarity of the collector response was inverted to compare the absolute collector response with the generator response during the forward scan. Additionally, we simulated the concentration profile of the reactant, O, at the respective scan rate (Figures 4-3 B, 4-3 D, and 4-3 F) to visualize a diffusion layer of the reactant, which is complementary to that of the product with a concentration given by $c_0 - c_O$.

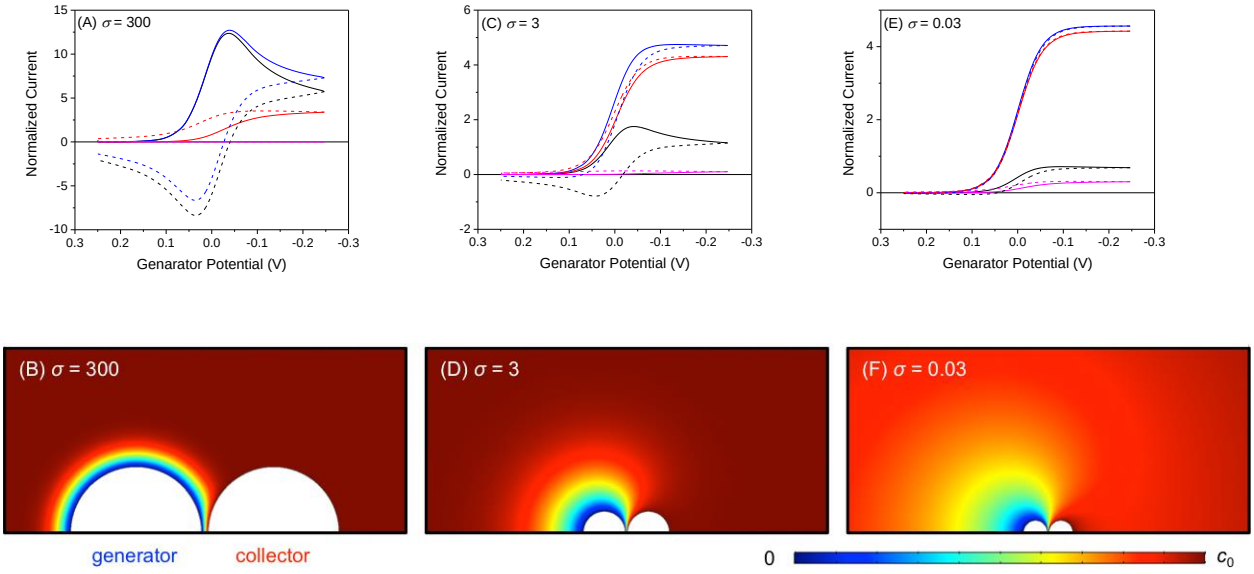

Figure 4-3 (A, C, E) Voltammetric responses at nanogap (blue and red) and solution (black and magenta) sides of generator and collector electrodes, respectively, with narrow gaps (G = 0.1) during forward (solid) and reverse (dashed) scans of generator potential. (B, D, F) Concentration profiles of the reactant, O, at the switching potential.

The highest scan rate of σ = 300 yielded a quasi-steady-state voltammetric response at the nanogap side of the collector electrode (red lines in Figure 4-3 A), which evidences that quasi-steady-state redox cycling was established between nanogap sides of generator and collector

electrodes. Redox cycling occurred between local regions of the nanogap sides as demonstrated by the simulated concentration profile of the reactant, O (Figure 4-3 B). Accordingly, the generator response at the nanogap side (blue lines in Figure 4-3 A) was still transient and dominated by the reactant diffusing from solution. Moreover, the potential scan was too fast for solution sides of generator and collector electrodes to participate in redox cycling. No current response was obtained at the solution side of the collector electrode (magenta lines), whereas a transient voltammetric response at the solution side of the generator electrode was unaffected (black lines). Overall, both nanogap and solution sides of the generator electrode yielded transient responses at σ = 300 when a quasi-steady-state response was obtained at the collector electrode without a contribution from the solution side.

Remarkably different responses were obtained at nanogap and solution sides of the generator electrode at σ = 3 (Figure 4-3 C). In this case, a voltammetric response at the nanogap side of the generator electrode reached quasi-steady states to nearly match a voltammetric response at the nanogap side of the collector electrode, thereby yielding a high collection efficiency of 0.91 determined from limiting currents. By contrast, a voltammetric response at the solution side of the generator electrode was still transient and peak-shaped during both forward and reverse scans. These results indicate that a transient generator response at σ = 3 (Figure 4-2 B) was attributed to a transient response at the solution side of the generator electrode, which was too far from the collector electrode to participate in redox cycling. In fact, only a small current response was obtained at the solution side of the collector electrode, which was also too far from the generator electrode. Moreover, the diffusion layer at the generator electrode extended nearly to the entire surface of the nanogap side of the collector electrode, but yet to its solution side (Figure 4-3 D). A

larger area of the nanogap side of the collector electrode contributed to redox cycling at $\sigma = 3$, thereby yielding a higher collector response (Figure 4-2 B) than at $\sigma = 300$ (Figure 4-2 A).

Eventually, the entire assembly of double-cylinder electrodes reached quasi-steady states at $\sigma = 0.03$. Voltammetric responses at each side of generator and collector electrodes showed a sigmoidal shape with negligible or small hysteresis (Figure 4-3 E). Voltammetric responses at nanogap sides of generator and collector electrodes nearly overlapped with each other to yield a remarkably high collection efficiency of 0.97 determined from liming currents. By contrast, the current response at the solution side of the generator electrode was higher than that at the solution side of the collector electrode, thereby yielding a lower overall collection efficiency of 0.90 for the entire double-cylinder electrodes (Figure 4-2 C). A simulated concentration profile (Figure 4-3 F) shows that the solution side of the collector electrode was only partially exposed to the redox product, R, produced at the generator electrode, whereas its solution side was fully exposed to the redox reactant, O, in solution.

Importantly, we found that the solution side of the generator electrode makes no influence on the collector response and, subsequently, on FSNV. This finding implies that the fabrication of double-cylinder UMEs is simplified without affecting FSNV by exposing the entire surfaces of generator and collector electrodes as proposed by removing the insulation sheath of double-disk-like UMEs.[19,20] Specifically, the solution side of the generator electrode was insulated in our model to prevent a redox reaction (Figure 4-8 in Supplemental Material). The resultant collector response was affected negligibly at $\sigma = 300$ and 3 (Figures 4-8 A and 4-8 B, respectively) and barely noticeable at $\sigma = 0.03$ (Figure 4-8 C). By contrast, the generator response was significantly reduced at $\sigma = 300$ and 3 to improve collection efficiency, which is irrelevant to FSNV. A very small insulation effect on the generator response was observed at $\sigma = 0.03$, where the current response

of the solution side of the generator electrode was already very low without insulation (Figure 4-3 E).

4.3.4 FSNV at Double-Cylinder UMEs with Wide Gaps (G=1)

We investigated the effects of gap width on FSNV by considering double-cylinder UMEs with wider gaps (G = 1). These gaps were still narrow enough to yield a substantial collector response at σ = 30, 3, and 0.03 (Figure 4-4), but not at σ = 300 (data not shown). This result indicates that a 3.5 μm-wide gap of the double-microcylinder UMEs with G = 1 is too wide for FSNV at the corresponding scan rate of 400 V/s (Table 4-1), thereby requiring a nanometer-wide gap to achieve sub-millisecond resolution of in-vivo FSCV.[3] A 35 nm-wide gap of the double-nanocylinder UMEs with G = 1 is also too wide to enable ultra-FSNV at 4 MV/s (Table 4-1), which requires a narrower gap (e.g., G = 0.1 in Figure 4-2 A). The current response of a collector electrode with a wide gap (G = 1) became substantial when the normalized scan rate was decreased to σ = 30 (Figure 4-4 A), which corresponds to 40 V/s and 400 kV/s for double-microcylinder and nanocylinder UMEs, respectively, with cylinder radii listed in Table 4-1. The collector response was delayed from the generator response during the forward scan, which is attributed to the time required for the redox product, R, to diffuse across the wide gap from the generated electrode to the collector electrode. The resultant collector response was transient without reaching a limiting value even during the reverse scan.

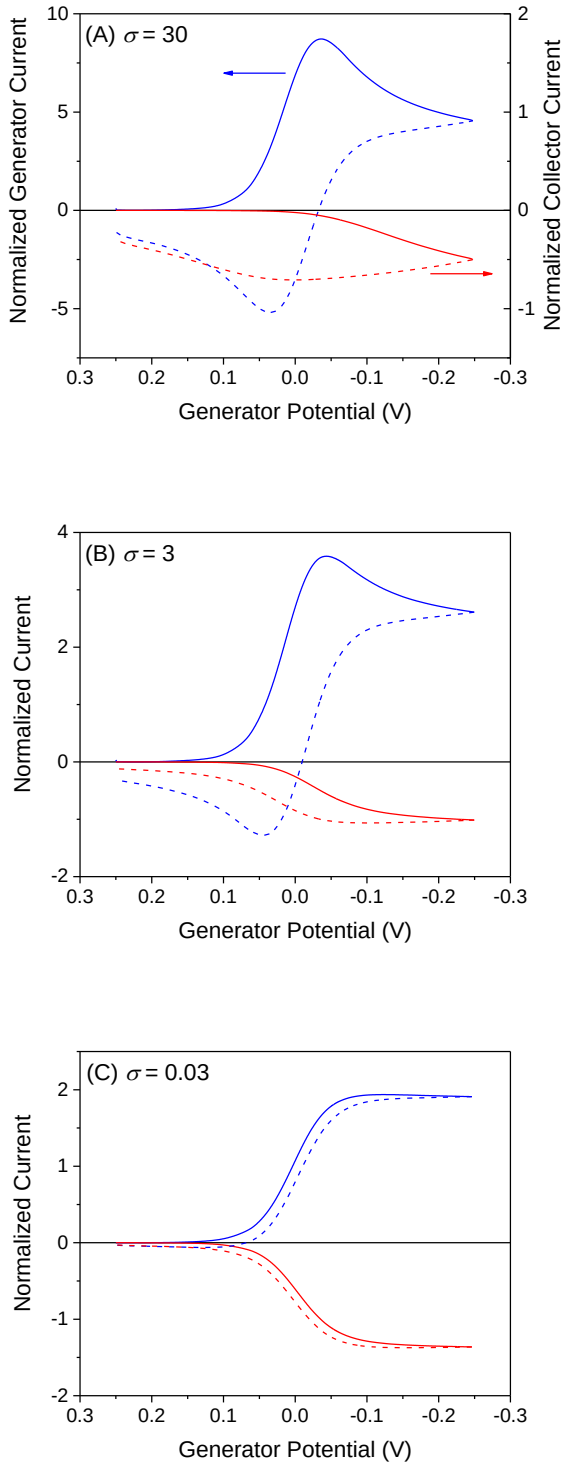

Figure 4-4 Voltammetric responses of generator (blue) and collector (red) electrodes with wide gaps (G = 1) during forward (solid) and reverse (dashed) scans of generator potential.

Quasi-steady-state FSNV was enabled by the collector electrode with G = 1 at σ = 3 and 0.03 (Figures 4-4 B and 4-4 C, respectively). The respective σ values correspond to fast scan rates of 40 kV/s and 400 V/s at the double-nanocylinder UMEs listed in Table 4-1. As σ decreased from 3 to 0.03, a limiting current at the collector electrode increased only from –1.1 to –1.4 to ensure quasi-steady states. By contrast, the generator response did not reach quasi-steady states even at σ = 0.03 as demonstrated by a slightly negative response during the reverse scan. These results indicate that the collector electrode reached quasi-steady states at least 100 times faster (σ > 3) than the generator electrode (σ < 0.03) with wider gaps (G = 1).

4.3.5 Current Distributions at Generator and Collector Electrodes with Wide Gaps (G=1)

Mechanistic insights into FSNV with wider nanogaps (G = 1) were gained by simulating voltammetric responses at nanogap and solution sides of generator and collector electrodes (Figure 4-5). In these plots, the polarity of the collector response was inverted for a comparison with the generator response. Interestingly, transient voltammetric responses at both sides of the generator electrode were nearly identical at σ = 30 while the current response at the nanogap side of the collector electrode was significant (Figure 4-5 A). The collector response indicates that this scan rate was slow enough for the redox product, R, to diffuse across the wider gap from the generator electrode to the collector electrode. By contrast, the generator response was unaffected, because this scan rate was too fast for the original reactant, O, regenerated at the collector electrode to return to the generator electrode across the wide gap. Accordingly, the collector response at σ = 30 was based on the time-of-arrival mechanism[33] rather than the redox-cycling mechanism. In fact,

the diffusion layer at the generator electrode barely overlapped with the nanogap side of the collector electrode (Figure 4-5 B).

The establishment of redox cycling across the wider gap required slower scan rates of σ = 3 and 0.03, thereby enhancing current responses at nanogap sides of both generator and collector electrodes (Figures 4-5 C and 4-5 E, respectively). In fact, the corresponding diffusion layers at the generator electrode significantly overlapped with the nanogap side of the collector electrode (Figures 4-5 D and 4-5 F). The efficiency of redox cycling, however, was still low at σ = 3 as indicated by a peak current and a lower liming current at the nanogap side of generator and collector electrodes, respectively. Finally, redox cycling became efficient enough at σ = 0.03 to obtain quasi-steady-state responses with small hysteresis at nanogap sides of both generator and collector electrodes with a high collection efficiency of 0.87 (Figure 4-5 E). At this scan rate, solution sides of generator and collector electrodes also participated in redox cycling, but showed large voltammetric hysteresis. Moreover, a peak-shaped transient response was obtained at the solution side of the generator electrode to render the entire generator response transient even at σ = 0.03 (Figure 4-4 C).

It should be noted that the voltammetric response of the collector electrode with G = 1 was also barely affected by insulating the solution side of the generator electrode (Figure 4-9 in Supplemental Material). Accordingly, the entire generator electrode may be fully exposed to simplify the fabrication of double-cylinder UMEs for FSNV. Lower collection efficiency based on a higher response at the fully exposed generator electrode is irrelevant to FSNV, which measures the collector response.

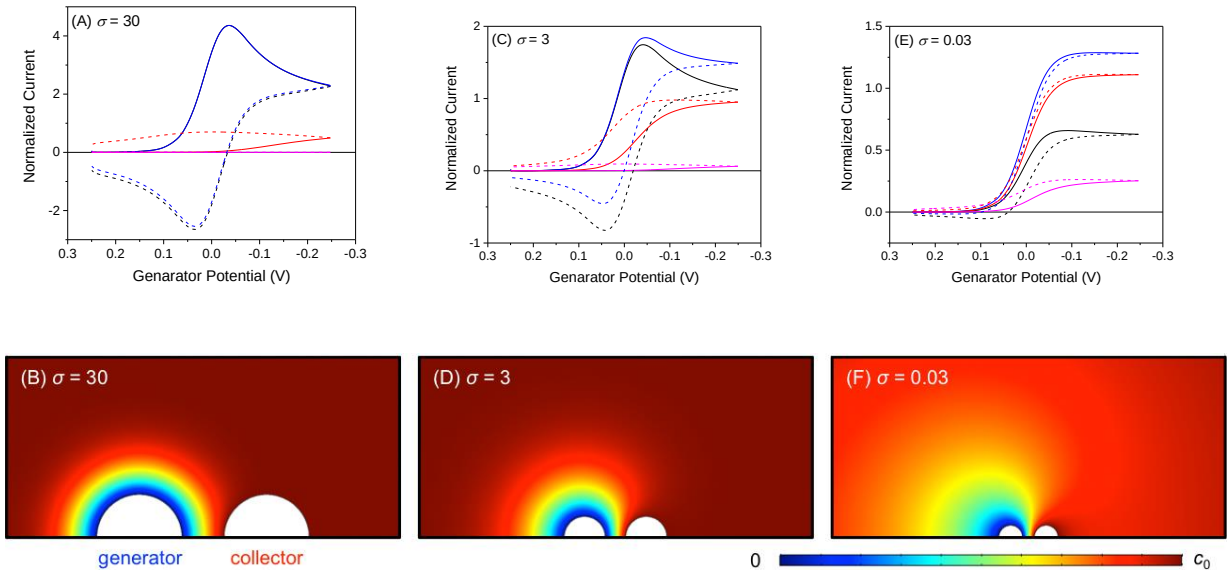

Figure 4-5 (A, C, E) Voltammetric responses at nanogap (blue and red) and solution (black and magenta) sides of generator and collector electrodes, respectively, with narrow gaps (G = 1) during forward (solid) and reverse (dashed) scans of generator potential. (B, D, F) Concentration profiles of the reactant, O, at the switching potential.

4.3.6 Effects of Cylinder Radius of FSNV

Advantageously, a collector electrode with a smaller cylinder radius reaches quasi-steady states faster without compromising sensitivity when a constant ratio of the cylinder radius against the gap width, i.e., *G*, is maintained. Accordingly, double-nanocylinder UMEs enable quasi-steady-state FSNV at up to megavolt per second (Table 4-1) to yield a limiting current that is as high as obtained with the micrometer counterpart, thereby facilitating ultrafast current measurement. A smaller cylinder radius decreases not only the active electrode area, but also the gap width to increase the flux across the gap and, subsequently, maintain a constant collector response. Importantly, a collector response can be used to determine the bulk concentration of the

redox reactant, which is electrolyzed at the generator electrode, not at the collector electrode. A limiting current at a collector electrode, $i_{c,lim}$, is proportional to the bulk concentration, c_0, as given by eq 7

$$i_{c,lim} = nFDLc_0I_{c,lim} \quad (11)$$

where $I_{c,lim}$ is the dimensionless liming current determined by G for a given σ value. $I_{c,lim}$ with G = 0.1 increased only by ~35% (Figure 4-2) as σ decreased from 300 to 0.03, where $I_{c,lim}$ with G = 1 was lower and varied by a factor of ~3 (Figure 4-4).

In addition, the cylinder radius affects the reversibility of FSNV as detailed in Supplementary Material. The reversibility of FSNV at the collector electrode is controlled by the dynamics of electron transfer at the generator electrode (eq 4) and mass transport across the nanogap. The reversibility of FSNV is apparent, because the regeneration of the reactant at the collector electrode is diffusion-limited (eq 5). When a constant gap–radius ratio, G, is maintained, FSNV becomes less reversible with a smaller cylinder radius, which narrows a gap to enhance mass transport across the gap. By contrast, the reversibility of FSNV is nearly independent of scan rate, which controls transient mass transport at the solution side of the generator electrode, but weakly affects quasi-steady-state mass transport across the gap. Practically, reversible FSNV is expected for fast redox couples, e.g., ferrocene compounds and $Ru(NH_3)_6^{3+}$,[34-39] at the double-cylinder UMEs listed in Table 4-1 with the exception of those with the narrowest 3.5 nm-wide gap. Fast mass transport across a nanogap is advantageous to mitigate interferences by slow redox couples, e.g., ascorbic acid in the brain.[2]

4.3.7 Comparison Between FSNV and FSCV

FSNV will complement FSCV by eliminating the need of background subtraction to enable some applications, which may also compensate the lower sensitivity of quasi-steady-state FSNV in comparison with transient FSCV as detailed in Supplementary Material. Briefly, the FSNV response of the double-cylinder UMEs listed in Table 4-1 is up to 14 times lower than the FSCV response of single-cylinder UMEs with identical sizes. Moreover, ultra-FSCV at 4 MV/s is ~23 times more sensitive than ultra-FSNV when the respective techniques employ 2.5 µm-radius single-disk UMEs[31,32] and 175 µm-long double-cylinder UMEs with 35 nm radius and 3.5 nm-wide gap[20,28] for ultrafast scan as listed in Table 4-1. Nevertheless, no background response of FSNV is crucial for various applications as represented by in-vivo determination of a basal concentration of neurotransmitters.[8] In this application, FSNV of neurotransmitters adsorbed on the electrode surface[3] will yield an enhanced transient response.[36] Moreover, the kinetics of extremely fast electrode reactions will be determinable more reliably by ultra-FSNV than ultra-FSCV with the high background,[31,32] where a higher reactant concentration can be used to enhance an ultra-FSNV response. It, however, should be noted that a higher FSNV response increases the *iR* drop, which is as large as in FSCV (Supplementary Material) and must be compensated for ultrafast scan.[31,32]

4.4 Conclusions

In this work, we employed the finite element method to predict that double-cylinder UMEs with nanometer-wide gaps will allow FSNV to quantitatively detect diffusing redox species at high

temporal resolution of transient FSCV under quasi-steady states without the need of background subtraction. It should be emphasized that we simulated FSNV only under quasi-steady states as demonstrated by the noticeable scan-rate-dependence of limiting currents and hysteresis in contrast to true steady states (i.e., $\tau_e \to \infty$) considered in the previous study.[18] Specifically, we predict that double-microcylinder UMEs will enable FSNV at hundreds volts per second as practiced for in-vivo FSCV in the brain using single carbon-fiber UMEs.[3] Moreover, ultra-FSNV at megavolts per second will be feasible using double-nanocylinder UMEs with narrower gaps to reach nanosecond resolution as demonstrated by ultra-FSCV using single-disk UMEs.[31,32] The cylindrical collector electrode can reach quasi-steady states ~10^4 times faster than the generator electrode with identical sizes to simultaneously yield quasi-steady-state and transient voltammograms, respectively, at fast scan rates as observed by SECM-based nanogap voltammetry with a UME tip and a macroscopic substrate at slow scan rates.[10,36-39] The versatile model[18,40] adapted for FSNV in this study will accommodate the adsorption of redox species on the electrode surface[36,41,42] to simulate transient FSNV for in-vivo-detection of adsorbed neurotransmitters, e.g., dopamine and serotonin[3] using adsorption isotherms reported in the literature.[43]

This study provides valuable information to rationally design double-cylinder UMEs for FSNV. A quasi-steady-state response is obtained faster at the collector electrode with a smaller gap–radius ratio, *G*, and can be enhanced by using longer cylinders even with a smaller radius to facilitate fast current measurement. While steady-state collection efficiency is useful to determine a gap–radius ratio[18], the improvement of collection efficiency at a slower scan rate is mainly due to a decay of the generator response, which is irrelevant to FSNV, thereby allowing for the exposition of the entire cylinder surfaces to simplify electrode fabrication. In fact, we proposed to fabricate double-cylinder carbon UMEs for FSNV by removing the insulating sheath of double-

disk-like carbon UMEs.[19,20] Double-cylinder carbon UMEs thus fabricated may be implantable in the brain with minimal tissue damage[44] and electrode fouling[45] to enable sensitive FSNV of adsorbed neurotransmitters in vivo.[3] Advantageously, FSNV will be minimally interfered by ascorbic acid, one of the most common interfering species for in-vivo FSCV,[2] because the irreversible interfering species is oxidized at the generator electrode and hydrolyzed in the nanogap to become redox-inactive at the collector electrode.[46-48] More broadly, a simple method for fabrication of nanogap electrodes will be useful for other electrode materials to promote the application of nanogap voltammetry at both fast and slow scan rates.

4.5 Supporting Information

4.5.1 Dimensionless Model

The diffusion problem defined in Figure 4-6 was solved using the following equations and parameters in the dimensionless form, in addition to eqs 6–9.[49]

$$\partial C_O/\partial \tau = (\partial^2 C_O/\partial X^2 + \partial^2 C_O/\partial Y^2) \quad \text{(S-1)}$$

$$C_O = c_O/c_0 \quad \text{(S-2)}$$

$$\tau = Dt/r^2 \quad \text{(S-3)}$$

$$X = x/r \quad \text{(S-4)}$$

$$Y = y/r \quad \text{(S-5)}$$

$$\partial C_O/\partial \boldsymbol{N} = -\lambda[C_O \theta^{-\alpha} - (1-C_O)\theta^{1-\alpha}] \quad \text{(S-6)}$$

$$\boldsymbol{N} = \boldsymbol{n}/r \quad \text{(S-7)}$$

$$\lambda = k^0 r/D \quad \text{(S-8)}$$

$$\theta = \exp[nF(E_g - E^{0'})/RT] \quad \text{(S-9)}$$

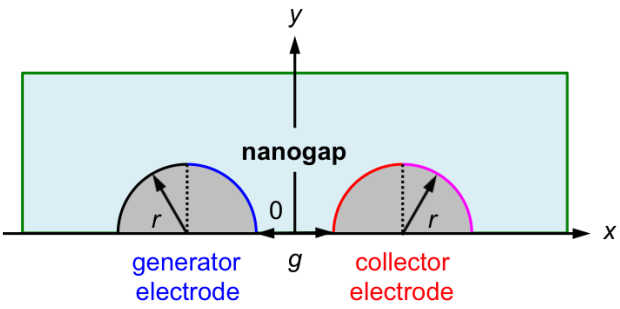

Figure 4-6 A model for double-cylinder electrodes with nanogaps. Boundary conditions for generator and collector electrodes are given by eqs 3 and 5, respectively. Blue and red boundaries represent nanogap and solution sides of the respective electrodes. Black and magenta boundaries represent solution sides of the respective electrodes. Green boundaries are simulation limits. The *x*-axis is the symmetry axis.

Our simulation was validated as follows.[49] Chronoamperometry at double-cylinder electrodes with a wide gap (G = 100) was simulated and compared with theory for single-cylinder electrodes.[50] The theoretical normalized current, $I(\tau)$, is given by

$$I(\tau) = \pi\exp[-(\pi\tau)^{1/2}/10]/(\pi\tau)^{1/2} + \pi/\ln\{2[\pi\exp(-\gamma_e)]^{1/2} + \exp(5/3)\} \quad \text{(S-10)}$$

where γ_e = 0.5772156… is the Euler's constant. Eq S-10 assumes diffusion-limited conditions, which we simulated by using a boundary condition of C_O = 0 at the generator electrode. The simulated generator response fitted well with eq S-10 (Figure 4-7) when the gap was much wider than the thickness of a diffusion layer at the generator electrode to mediate no redox cycling.[49] Time regimes of chronoamperometry matched those of voltammetry simulated in this work.

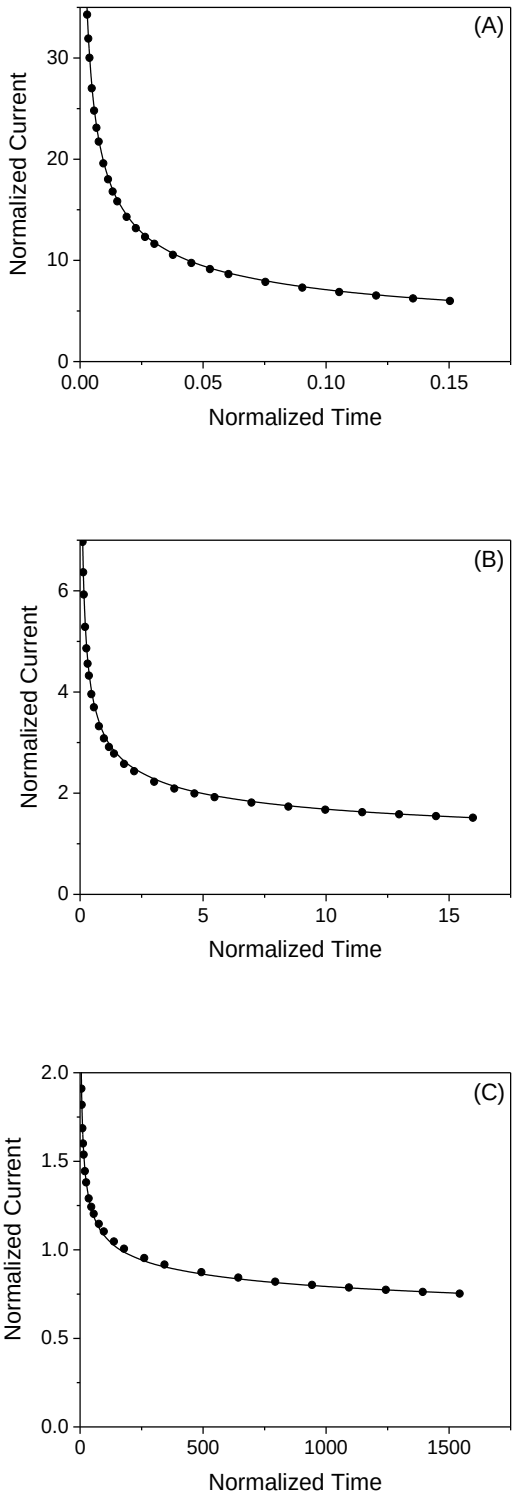

Figure 4-7 (A) Short-, (B) intermediate- and (C) long-time chronoamperometric responses (dots) of the generator electrode with *G* = 100. Solid lines represent eq S-10.

4.5.2 Insulation of the Solution Side of Generator Electrode

We simulated voltammetric responses of double-cylinder electrodes when the solution side of the generator electrode was insulated to locally prevent a redox reaction. We considered gap widths of G = 0.1 and 1 (Figures 4-8 and 4-9, respectively) at σ = 300, 3, and 0.03 (parts A, B, and C of each figure, respectively) to compare the resultant voltammograms with those at fully exposed double-cylinder UMEs depicted from Figure 4-2 and 4-4.

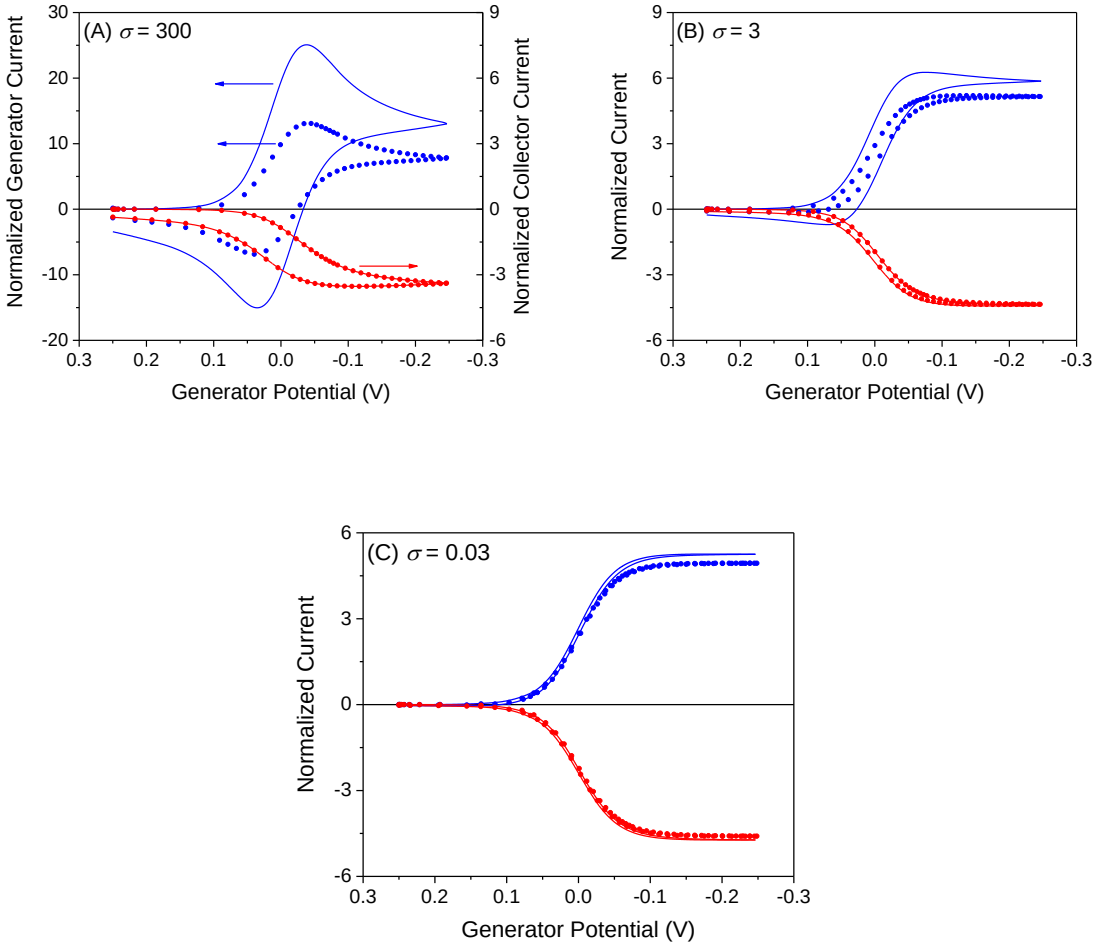

Figure 4-8 Voltammetric responses of generator (blue) and collector (red) electrodes with narrow gaps of *G* = 0.1 with (dots) and without (lines) the insulation of the solution side of the generator electrode.

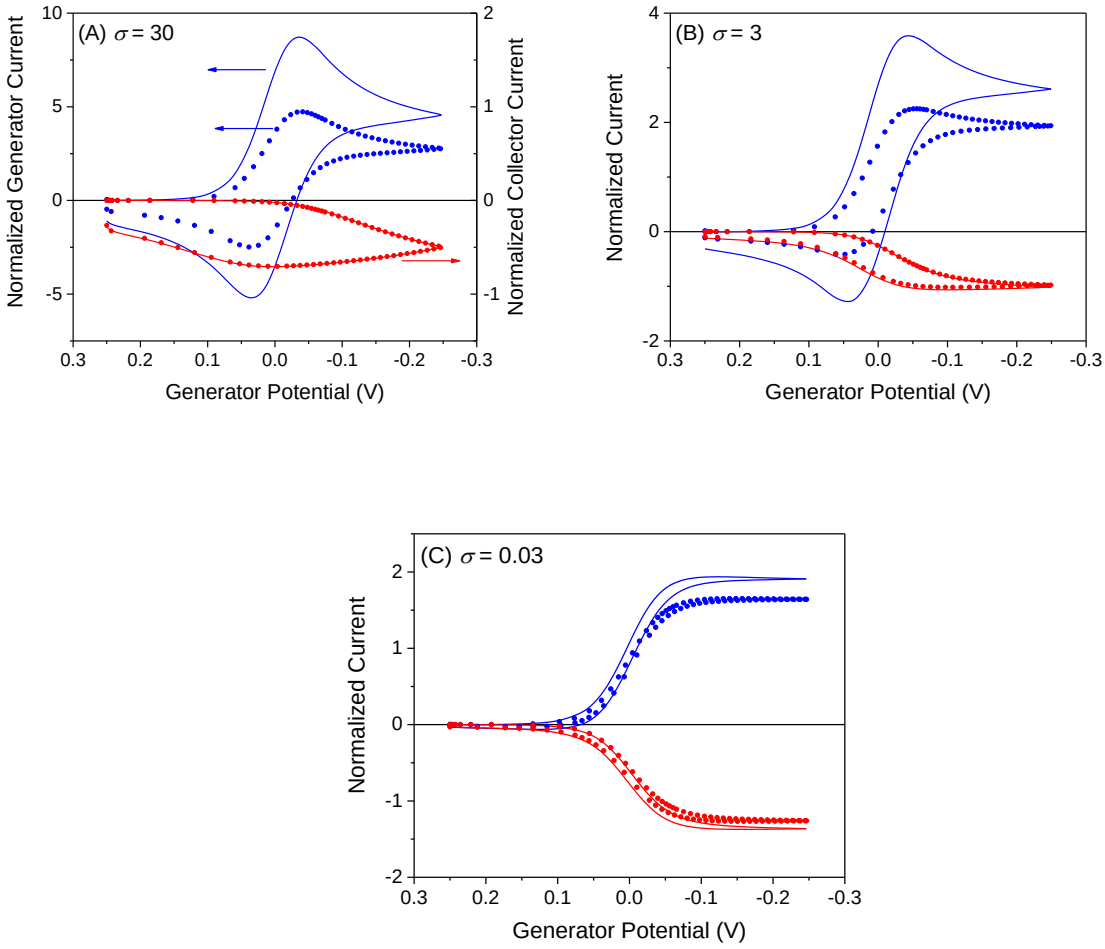

Figure 4-9 Voltammetric responses of generator (blue) and collector (red) electrodes with narrow gaps of *G* = 1 with (dots) and without (lines) the insulation of the solution side of the generator electrode.

4.5.3 Kinetic Effects

We simulated the effects of the dimensionless standard electron-transfer rate constant, λ, on voltammetric responses of double-cylinder electrodes with G = 0.1 and 1 (Figures 4-10 and 4-11, respectively) at σ = 300, 3, and 0.03 (parts A, B, and C of each figure, respectively). The collector response was nearly identical with $\lambda \geq 100$ and ≥ 10 for G = 0.1 and 1, respectively, thereby ensuring reversible responses. With G = 0.1, $\lambda \geq 100$ corresponds to k^0 values of ≥1.7 and

$\geq 1.7 \times 10^2$ cm/s for 3.5 μm- and 35 nm-radius cylinders, respectively. Lower λ values of ≥ 10 with G = 1 correspond to k^0 values of ≥0.17 and ≥17 cm/s for 3.5 μm- and 35 nm-radius cylinders, respectively.

Reversible FSNV is expected for fast redox couples under the conditions listed in Table 1 with the exception of the 35 nm-radius cylinder electrode with a gap width of 3.5 nm. The narrowest gap requires a k^0 value of $\geq 1.7 \times 10^2$ cm/s for reversible FSNV to exceed not only an extremely high k^0 value of 1×10^2 cm/s expected from the Marcus theory of adiabatic outer-sphere electron transfer[53] for (ferrocenylmethyl)trimethylammonium ($FcTMA^+$) with a small reorganization energy,[51,52] but also anomalously high k^0 values of 79[54] and 36[55] cm/s experimentally determined for $Ru(NH_3)_6^{3+}$ at platinum to exceed the Marcus prediction.[56] By contrast, the k^0 values required for reversible FSNV at other double-cylinder UMEs listed in Table 1 are comparable to or lower than large k^0 values estimated for $FcTMA^+$,[51,52,57] ferrocenemethanol,[58] and $Ru(NH_3)_6^{3+}$ [52] from reversible nanogap voltammograms at various carbon electrodes by SECM.

It should be noted that $\lambda \geq 100$ was required to obtain reversible voltammograms at generator electrodes at $\sigma \geq 3$ with either G = 0.1 or 1. The reversibility of the transient generator response at $\sigma \geq 3$ was weakly dependent of the gap–radius ratio, G, and was significantly lowered at higher σ, which enhances transient mass transport of the reactant, O, from solution to the generator electrode.

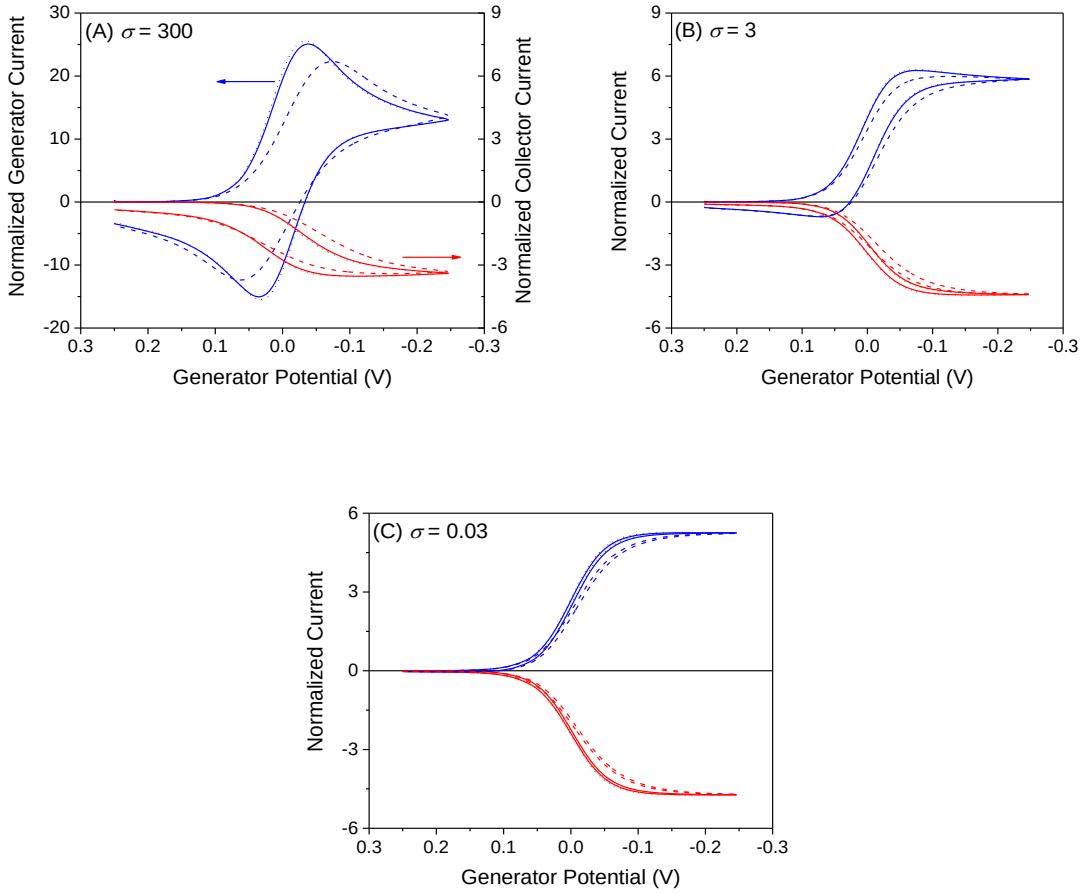

Figure 4-10 Voltammetric responses of generator (blue) and collector (red) electrodes with narrow gaps (*G* = 0.1) with λ = (dotted) 1000, (solid) 100, and (dashed) 10.

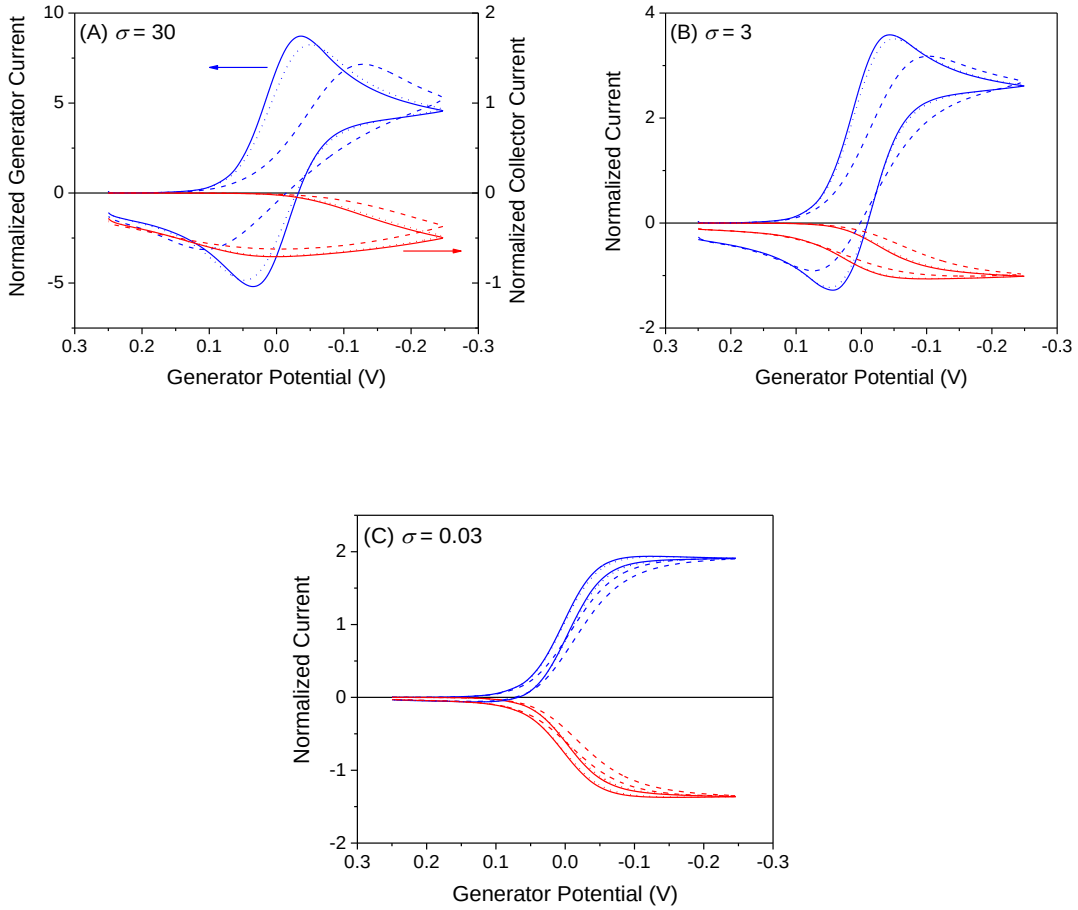

Figure 4-11 Voltammetric responses of generator (blue) and collector (red) electrodes with wide gaps (G = 1) with λ = (solid) 100, (dotted) 10, and (dashed) 1.

4.5.4 Sensitivity of FSNV and FSCV

We compared quasi-steady-state FSNV at double-cylinder UMEs with transient FSCV at single UMEs in terms of sensitivity and the *iR* drop. While the limiting current of quasi-steady-state FSNV is given by eq 11, the forward peak current of transient FSCV based on purely planar diffusion is given for reversible conditions by[61]

$$i_p = 0.4463(n^3F^3Dv/RT)^{1/2}Ac_0 \quad \text{(S-11)}$$

where A is the electrode area. As the reaction becomes less reversible, the peak current is lowered slightly by a factor of down to $\sim\alpha^{1/2}$ with $\alpha \approx 0.5$[53] under irreversible conditions.[62]

First, we compared the sensitivity of FSNV at double-cylinder UMEs with that of transient FSCV at single-cylinder UMEs with identical radius and length. Specifically, the ratio of the forward peak current of FSCV at a single-cylinder electrode (eq S-11 with $A = 2\pi rL$) with respect to the limiting current of FSNV at a cylindrical collector electrode with identical sizes (eq 11) was obtained as

$$i_p(\text{cylinder})/i_{c,lim} = (0.8926\pi/I_{c,lim})(n\sigma)^{1/2} \quad \text{(S-12)}$$

Eq S-12 gives a ratio of 14 with $G = 0.1$ and $\sigma = 300$, which corresponds to $v = 400$ V/s and 4 MV/s at 3.5 μm- and 35 nm-radius cylinders, respectively (Table 4-1). Eq S-12 yields a smaller ratio of 1.1 for $G = 0.1$ and $\sigma = 3$, which corresponds to $v = 40$ kV/s at the 35 nm-radius cylinder electrode.

In addition, we compared the sensitivity of ultra-FSNV at double-cylinder UMEs with that of ultra-FSCV at single-disk UMEs. In this case, the ratio of the peak current at the disk electrode (eq S-11 with $A = \pi r^2$) with respect to a limiting current at the cylindrical collector electrode (eq 11) was obtained as

$$i_p(\text{disk})/i_{c,lim} = (0.4463\pi a^2/I_{c,lim}L)(nFv/RTD)^{1/2} \quad \text{(S-13)}$$

Eq S-13 gives a ratio of 23 at $v = 4$ MV/s for a 2.5 μm-radius disk UME (S-11, S-12) with respect to 175 μm-long double-cylinder UMEs with 35 nm radius and 3.5 nm gap[63,64] in Table 4-1.

Finally, the iR drop in quasi-steady-state FSNV at a double-cylinder electrode can be as large as that in transient FSCV at a single electrode. In FSNV, the collector response is measured against the generator potential. Accordingly, the iR drop at the generator electrode is relevant to

FSNV and can be as large as the *iR* drop at the corresponding single electrode in FSCV when the high background current dominates current responses of both generator and single electrodes in FSNV and FSCV, respectively. It should be noted that the *iR* drop at the collector electrode is much smaller, because of a lack of a background response, and can be compensated by applying a sufficiently large potential to detect a redox species under diffusion-limited conditions.

4.6 Acknowledgments

This work was partially supported by the National Science Foundation (CHE 1608703) and the National Institutes of Health (GM112656).

4.7 References

(1) C. Amatore and E. Maisonhaute, *Anal. Chem.* **2005**, ***77***, 303A.

(2) D. L. Robinson, A. Hermans, A. T. Seipel and R. M. Wightman, *Chem. Rev.* **2008**, *108*, 2554.

(3) N. T. Rodeberg, S. G. Sandberg, J. A. Johnson, P. E. M. Phillips and R. M. Wightman, *ACS Chem. Neurosci.* **2017**, *8*, 221.

(4) X. S. Zhou, B. W. Mao, C. Amatore, R. G. Compton, J. L. Marignier, M. Mostafavi, J. F. Nierengarten and E. Maisonhaute, *Chem. Commun.* **2016**, *52*, 251.

(5) A. J. Bard and L. R. Faulkner, *Electrochemical Methods: Fundamentals and Applications*, John Wiley & Sons, New York, 2001, p. 14.

(6) A. J. Bard and L. R. Faulkner, *Electrochemical Methods: Fundamentals and Applications*, John Wiley & Sons, New York, 2001, p. 589.

(7) A. J. Bard and L. R. Faulkner, *Electrochemical Methods: Fundamentals and Applications*, John Wiley & Sons, New York, 2001, p. 232.

(8) E. S. Bucher and R. M. Wightman, *Annu. Rev. Anal. Chem.* **2015**. *8*, 239.

(9) M. A. G. Zevenbergen, D. Krapf, M. R. Zuiddam and S. G. Lemay, *Nano Lett.* **2007**, *7*, 384.

(10) N. Nioradze, J. Kim and S. Amemiya, *Anal. Chem.* **2011**, *83*, 828.

(11) S. Amemiya, R. Chen, N. Nioradze and J. Kim, *Acc. Chem. Res.* **2016**, *49*, 2007.

(12) H. S. White and K. McKelvey, *Curr. Opin. Electrochem.***2018**, *7*, 48.

(13) B. J. Seddon, C. F. Wang, W. F. Peng and X. J. Zhang, *J. Chem. Soc., Faraday Trans.* **1994**, *90*, 605.

(14) B. J. Seddon, C. F. Wang, W. F. Peng and X. J. Zhang, *Electrochim. Acta*, **1995**, *40*, 455.

(15) C. G. Zhang, X. J. Zhang, C. Yang, W. M. Zhang, B. Yao and X. Y. Zhou, *Electroanalysis*, **1996**, *8*, 947.

(16) B. J. Seddon, H. H. Girault, M. J. Eddowes, W. Peng and Z. Zhao, *J. Chem. Soc., Faraday Trans.* **1991**, *87*, 2603.

(17) W. F. Peng, P. B. Li and X. Y. Zhou, *J. Electroanal. Chem.* **1993**, *347*, 1.

(18) C. Amatore, A. Oleinick and I. Svir, *J. Electroanal. Chem.*, **2003**, *553*, 49.

(19) J. E. Baur, H. M. Miller and M. A. Ritchason, *Anal. Chim. Acta*, **1999**, *397*, 123.

(20) K. McKelvey, B. P. Nadappuram, P. Actis, Y. Takahashi, Y. E. Korchev, T. Matsue, C. Robinson and P. R. Unwin, *Anal. Chem.*, **2013**, *85*, 7519.

(21) S. G. Lemay, S. Kang, K. Mathwig and P. S. Singh, *Acc. Chem. Res.* **2013**, *46*, 369.

(22) B. Wolfrum, E. Kätelhön, A. Yakushenko, K. J. Krause, N. Adly, M. Hüske and P. Rinklin, *Acc. Chem. Res.***2016**, *49*, 2031.

(23) S. Amemiya, Nanoscale Scanning Electrochemical Microscopy in *Electroanalytical Chemistry*, A. J. Bard and C. G. Zoski Editors, CRC Press, 2015, p. 1.

(24) T. Kai, C. G. Zoski and A. J. Bard, *Chem. Commun.* **2018**, ***54***, 1934.

(25) A. J. Bard and L. R. Faulkner, *Electrochemical Methods: Fundamentals and Applications*, John Wiley & Sons, New York, 2001, p. 98.

(26) A. Szabo, D. K. Cope, D. E. Tallman, P. M. Kovach and R. M. Wightman, *J. Electroanal. Chem.* **1987**, *217*, 417j.

(27) B. Zhang, K. L. Adams, S. J. Luber, D. J. Eves, M. L. Heien and A. G. Ewing, *Anal. Chem.* **2008**, *80*, 1394.

(28) H. R. Rees, S. E. Anderson, E. Privman, H. H. Bau and B. J. Venton, *Anal. Chem.* **2015**, *87*, 3849.

(29) F.-R. F. Fan and A. J. Bard, *Science* **1995**, 267, 871.

(30) R. J. White and H. S. White, *Langmuir* **2008**, *24*, 2850.

(31) C. Amatore, E. Maisonhaute and G. Simonneau, *Electrochem. Commun.* **2000**, *2*, 81.

(32) C. Amatore, E. Maisonhaute and G. Simonneau, *J. Electroanal. Chem.* **2000**, *486*, 141.

(33) A. Boika and A. J. Bard, *Anal. Chem.* **2015**, *87*, 4341.

(34) R. M. Penner, M. J. Heben, T. L. Longin and N. S. Lewis, *Science* **1990**, *250*, 1118.

(35) J. Kim and A. J. Bard, *J. Am. Chem. Soc.* **2016**, *138*, 975.

(36) R. Chen, R. J. Balla, Z. T. Li, H. Liu and S. Amemiya, *Anal. Chem.* **2016**, *88*, 8323.

(37) A. Morteza Najarian, R. Chen, R. J. Balla, S. Amemiya and R. L. McCreery, *Anal. Chem.* **2017**, *89*, 13532.

(38) N. Nioradze, R. Chen, N. Kurapati, A. Khvataeva-Domanov, S. Mabic and S. Amemiya, *Anal. Chem.* **2015**, *87*, 4836.

(39) R. Chen, N. Nioradze, P. Santhosh, Z. Li, S. P. Surwade, G. J. Shenoy, D. G. Parobek, M. A. Kim, H. Liu and S. Amemiya, *Angew. Chem. Int. Ed.* **2015**, *54*, 15134.

(40) C. Amatore, A. Oleinick and I. Svir, *Electrochem. Commun.* **2003**, *5*, 989.

(41) M. A. Bhat, N. Nioradze, J. Kim, S. Amemiya and A. J. Bard, *J. Am. Chem. Soc.* **2017**, *139*, 15891.

(42) O. V. Klymenko, I. Svir and C. Amatore, *J. Electroanal. Chem.* **2013**, *688*, 320.

(43) Heien M. L. A. V., Phillips P. E. M., Stuber G. D., Seipel A. T. and Wightman R. M. *Analyst* **2003,** *128*, 1413.

(44) A. Jaquins-Gerstl and A. C. Michael, *Analyst* **2015,** *140*, 3696.

(45) P. Takmakov, M. K. Zachek, R. B. Keithley, P. L. Walsh, C. Donley, G. S. McCarty and R. M. Wightman, *Anal. Chem.* **2010**, *82*, 2020.

(46) B. Wolfrum, M. Zevenbergen and S. Lemay, *Anal. Chem.* **2008**, *80*, 972.

(47) F. Zhu, J. Yan, M. Lu, Y. Zhou, Y. Yang and B. Mao, *Electrochim. Acta* **2011**, *56*, 8101.

(48) C. Ma, N. M. Contento, L. R. Gibson and P. W. Bohn, *Anal. Chem.* **2013**, *85*, 9882.

(49) C. Amatore, A. Oleinick and I. Svir, *J. Electroanal. Chem.* **2003**, *553*, 49.

(50) A. Szabo, D. K. Cope, D. E. Tallman, P. M. Kovach and R. M. Wightman, *J. Electroanal. Chem.* **1987**, *217*, 417.

(51) R. Chen, R. J. Balla, Z. T. Li, H. T. Liu and S. Amemiya, *Anal. Chem.* **2016**, *88*, 8323.

(52) A. Morteza Najarian, R. Chen, R. J. Balla, S. Amemiya and R. L. McCreery, *Anal. Chem.* **2017**, *89*, 13532.

(53) R. A. Marcus, *J. Chem. Phys.* **1965**, *43*, 679.

(54) R. M. Penner, M. J. Heben, T. L. Longin and N. S. Lewis, *Science* **1990**, *250*, 1118.

(55) J. Kim and A. J. Bard, *J. Am. Chem. Soc.* **2016**, *138*, 975.

(56) J. T. Hupp, H. Y. Liu, J. K. Farmer, T. Gennett and M. J. Weaver, *J. Electroanal. Chem.* **1984**, *168*, 313.

(57) N. Nioradze, R. Chen, N. Kurapati, A. Khvataeva-Domanov, S. Mabic and S. Amemiya, *Anal. Chem.* **2015**, *87*, 4836.

(58) R. Chen, N. Nioradze, P. Santhosh, Z. Li, S. P. Surwade, G. J. Shenoy, D. G. Parobek, M. A. Kim, H. Liu and S. Amemiya, *Angew. Chem. Int. Ed.* **2015**, *54*, 15134.

(59) C. Amatore, E. Maisonhaute and G. Simonneau, *Electrochem. Commun.* **2000**, *2*, 81.

(60) C. Amatore, E. Maisonhaute and G. Simonneau, *J. Electroanal. Chem.* **2000**, *486*, 141.

(61) A. J. Bard and L. R. Faulkner, *Electrochemical Methods: Fundamentals and Applications*, John Wiley & Sons, New York, 2001, p. 231.

(62) A. J. Bard and L. R. Faulkner, *Electrochemical Methods: Fundamentals and Applications*, John Wiley & Sons, New York, 2001, p. 234.

(63) H. R. Rees, S. E. Anderson, E. Privman, H. H. Bau and B. J. Venton, *Anal. Chem.* **2015**, *87*, 3849.

(64) K. McKelvey, B. P. Nadappuram, P. Actis, Y. Takahashi, Y. E. Korchev, T. Matsue, C. Robinson and P. R. Unwin, *Anal. Chem.* **2013**, *85*, 7519.

5.0 Nanogap-based Electrochemical Measurements at Double-Carbon-Fiber Ultramicroelectrodes

This thesis author pulled and characterized newly developed double-carbon-fiber ultramicroelectrodes utilizing vertical puller. Electrodes were further characterized using scanning electron microscopy and milled to controlled lengths by focused ion beam milling.

5.1 Introduction

A pair of electrodes with nanometer-wide separation constitutes a nanogap cell to enable unprecedented electrochemical measurements.[1-3] Nanogap-based electrochemical cells were used for the highly sensitive detection of analytes at down to the single molecule level,[4,5] the kinetically selective elimination of interfering species,[6,7] and the measurement of extremely fast electron-transfer kinetics.[8,9] The fabrication of nanogap cells, however, is based on the extensive nanolithography of chip-type electrodes[5,10] or nanoscale electrode positioning by scanning electrochemical microscopy (SECM),[11,12] thereby preventing a wider range of applications. Moreover, the power of nanogap electrodes has not been fully explored owing to limited designs. Recently, we employed finite element simulation to predict that a parallel pair of cylindrical ultramicroelectrodes (UMEs) with nanometer-wide separation enables quasi-steady-state

voltammetry at fast scan rates without serious interference from transient background[13] in contrast to fast-scan cyclic voltammetry with single-cylinder UMEs.[14] In addition, the probe-type design of nanogap-based double-cylinder UMEs is potentially useful for implantation into tissues with minimal damage[15] to enable in-vivo measurements with high temporal and spatial resolution as practiced by using single-cylinder UMEs.[14] There, however, have been reports of double-cylinder UMEs only with micrometer-wide gaps,[16] which were used to assess steady-state theories[17] at slow scan rates. Moreover, nanogap cells were characterized voltammetrically only at slow scan rates of $\leq$0.1 V/s.[2,3]

Herein, we report the simple fabrication of UMEs based on a pair of carbon fibers (CFs) with nanometer-wide separation (Figure 5-1 A) to voltammetrically achieve the high temporal resolution, low background current, and high kinetic selectivity at fast scan rates. In this work, the potential of the generator electrode is scanned to reduce $Ru(NH_3)_6^{3+}$ to $Ru(NH_3)_6^{2+}$, which is amperometrically detected at the collector electrode at a constant potential (Figure 5-1 B) to regenerate $Ru(NH_3)_6^{3+}$ and, subsequently, complete redox cycling (red and blue arrows in Figure 5-1 C). We demonstrate experimentally and theoretically that the efficient diffusion of the $Ru(NH_3)_6^{3+/2+}$ couple across a nanogap establishes quasi-steady-state redox cycling when the generator potential is cycled at 100 V/s and 1000 V/s, respectively. Moreover, the transient background of amperometric collector response is ~100 times lower than that of the generator voltammogram based on the plot of the generator current against the generator potential. Accordingly, background subtraction is not needed to quantitatively analyze the resultant nanogap voltammogram based on the plot of the amperometric collector response against the generator potential by the finite element method,[13] which yields reproducible gap widths of ~180 nm.

Preliminarily, we apply double-CF UMEs to detect dopamine (DA) with improved kinetic selectivity against ascorbic acid (AA) at fast scan rates of up to 100 V/s.

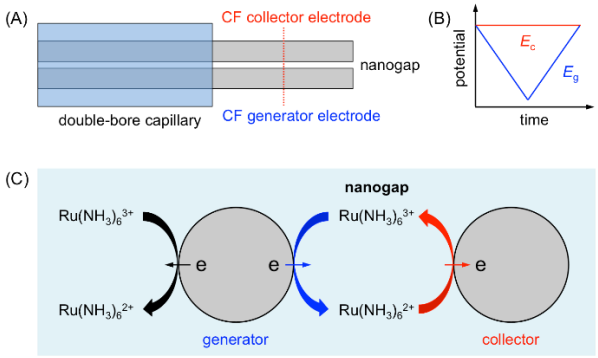

Figure 5-1 Scheme of (A) a double-CF UME and (B) waveforms for nanogap voltammetry. E_g and E_c are potentials of generator and collector electrodes, respectively. Red dotted line in part A corresponds to the cross section shown in part C for redox cycling of the $Ru(NH_3)_6^{3+/2+}$ couple across the nanogap (red and blue arrows) as well as the reduction of $Ru(NH_3)_6^{3+}$ at the side of the generator electrode far from the nanogap (black arrows).

5.2 Double-Carbon Fiber Ultramicroelectrodes

We obtained double-CF UMEs without extensive nanolithography[5,10] or nanoscale SECM[11,12] by adapting a fabrication procedure established for single-CF UMEs (Supporting Information), which have been widely used for in-vivo electrochemical measurements.[14] In fact, double-CF UMEs were prepared previously by heat-pulling a theta glass capillary filled with CFs, but were further polished to yield double-disk CF UMEs with gap distances of <1 μm.[18] In this work, we obtained ~50 μm-long CFs exposed from the glass capillary (Figure 5-2 A) by milling as-pulled double-CF UMEs using focused ion-beam (FIB) technology to remove the rest of CFs that eventually contacted with each other (Figures 5-7 A and 5-7 B). Importantly, a narrow gap

between the resultant short CFs (Figure 5-2 B) was obtained inherently and was not prepared by FIB. We employed FIB to achieve ~100% success of milling CFs to the desirable length, which is long enough to be manually cut with a lower success rate as demonstrated for the fabrication of single-CF UMEs.[14] The overall yield of good double-CF UMEs was limited by direct contact and subsequent current flow between generator and collector electrodes (Figure 5-8). So far, 72 double-CFM UMEs have been milled by FIB and characterized electrochemically to find that 45 of these devices (62.5%) yielded independent current responses at generator and collector electrodes without contact. It should be noted that we used a double-bore glass capillary with disk-shaped channels instead of a theta glass capillary with semielliptical channels[18] to seal the gap between CF and glass wall without using a glue, which filled the gap between CFs. A wider gap can be obtained by using a capillary with a wider bore–bore separation (Figures 5-7 C and 5-7 D).

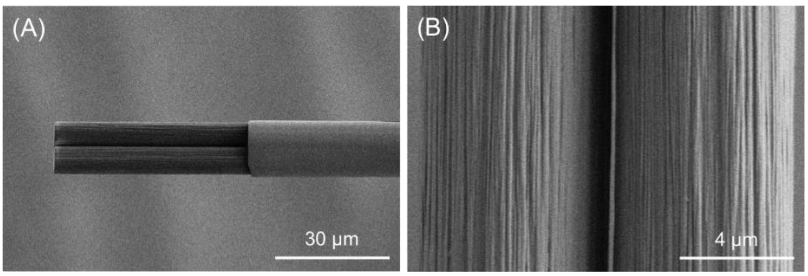

Figure 5-2 Scanning electron microscopy of (A) a double-CF UME sealed in a glass capillary and (B) a nanogap between CFs.

5.3 Results and Discussion

5.3.1 Ruthenium Hexamine Couple

Double-CF UMEs were characterized voltammetrically using a commercial bipotentiostat with some modifications (Supporting Information) to measure both generator and collector responses when the generator potential was cycled at up to 100 V/s (Figure 5-3). As the scan rate was decreased from 100 V/s to 2 V/s, the voltammetric generator response changed from a transient response with a pair of anodic and cathodic peaks to a quasi-steady-state response with a sigmoidal shape and a hysteresis (top panel of Figure 5-3 A). The transient generator response is attributed to a current response based on the diffusion of the $Ru(NH_3)_6^{3+/2+}$ couple from the solution to the side of the generator surface far from the nanogap (black arrows in Figure 5-1 C).[13] By contrast, the corresponding amperometric collector response maintained a sigmoidal dependence on the generator potential even at 100 V/s (bottom panel of Figure 5-3 A), thereby ensuring quasi-steady-state redox cycling across the nanometer-wide gap between generator and collector electrodes[13] (blue and red arrows in Figure 5-1 C). Importantly, the capacitive background of the amperometric collector response was negligible in comparison with that of the voltammetric generator response. Eventually, both generator and collector electrodes gave quasi-steady-state responses with low background to yield high collection efficiencies of ~0.90 as expected for double-cylinder UMEs under steady states[19] when the scan rate of generator potential was lowered to 0.02 V/s (Figure 5-3 B).

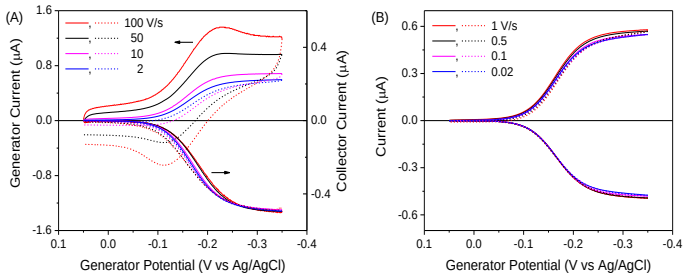

Figure 5-3 Generator (top panel) and collector (bottom panel) current responses of double-CF UMEs at (A) 2–100 and (B) 0.02–1 V/s in 10 mM $Ru(NH_3)_6^{3+}$ and 1 M KCl. Solid and dashed lines represent forward and reverse scans, respectively. Collector potential at –0.05 V.

We analyzed nanogap voltammograms by the finite element method based on a 2D diffusion model of double-cylinder UMEs[13] (Supporting Information) to estimate gap widths of 0.18 ± 0.03 μm with five electrodes. In this analysis, we fixed a CF radius of 3.5 μm to fit experimental nanogap voltammograms at 100 V/s with those simulated by adjusting nanogap width, CF length, and standard electron-transfer rate constant, k^0, at the generator electrode (Figure 5-4 A). The hysteresis of a nanogap voltammogram served as a measure of gap width, whereas the limiting current was based on the convolution of gap width and CF length.[13] The CF length and k^0 value thus determined at 100 V/s yielded good fits of nanogap voltammograms at slower scan rates (Figures 5-4 B, 5-9 A, and 5-9 B) with those simulated by adjusting gap width. In addition, parameters determined from nanogap voltammograms were used to simulate the generator response, which required background subtraction. A comparison of a collector response with a background-subtracted generator response at the switching potential yielded higher collection efficiencies of 0.7 ± 0.1, 0.83 ± 0.05, 0.89 ± 0.04, and 0.91 ± 0.03 with five electrodes as the scan rate decreased from 100 V to 10, 1, and 0.1 V, respectively, as expected theoretically.[13] We also extended the finite element simulation to demonstrate that the gap of the double-CF UMEs

developed in this study is narrow enough to establish quasi-steady-state redox cycling even at 1000 V/s (Figure 5-11). Furthermore, 3D model was used to find that efficient redox cycling across the nanogap enhanced generator responses by a factor of ~2.5 and ~10 at 100 and 0.1 V/s, respectively, in comparison with the corresponding transient responses of single CF UMEs with identical sizes (Figure 5-13).

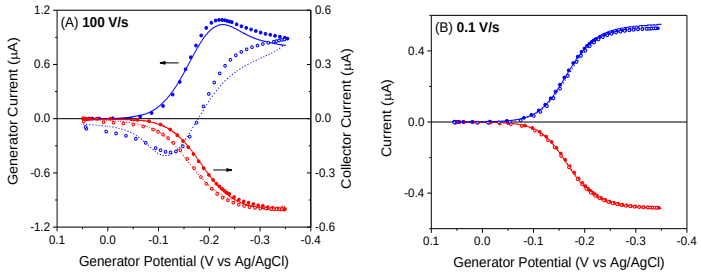

Figure 5-4 Experimental (lines) and simulated (circles) current responses of generator (blue) and collector (red) electrodes in 10 mM $Ru(NH_3)_6^{3+}$ and 1 M KCl at (A) 100 and (B) 0.1 V/s. Only experimental generator responses were background-subtracted. Solid lines and closed circles represent forward scans. Dashed lines and open circles correspond to reverse scans. Simulation employed k^0 = 0.9 cm/s, formal potential of –0.185 V, diffusion coefficient of 7.0×10^{-6} cm^2/s, CF length of 51.1 μm, and gap widths of 0.15 ± 0.02 μm.

Excellent fits between experimental and simulated voltammograms yielded k^0 at the generator electrode in addition to gap width and CF length (~50 μm). Both generator and collector responses were quasi-reversible in 1 M KCl solution of extremely pure water with low total organic carbon (TOC) of 2–3 ppb to yield a k^0 value of 0.9 cm/s, which is close to a k^0 value of 2.2 cm/s predicted for the $Ru(NH_3)_6^{3+/2+}$ couple by Marcus theory for adiabatic outer-sphere electron transfer.[20] By contrast, other electrode materials yielded k^0 values of ≥10 cm/s for the $Ru(NH_3)_6^{3+/2+}$ couple to exceed the theoretical value.[21] These anomalously high k^0 values are attributed to inner-sphere electron transfer as discussed qualitatively in our recent work[21] and quantitatively in thre Supporting Information to estimate k^0 values of 30–46 cm/s, which are

comparable to those measured in low-TOC ultrapure water (e.g., 36 ± 4 cm/s at single Pt nanoparticles[22]). Without the use of such pure water, k^0 values (e.g., 10 ± 5 cm/s at metallic carbon nanotubes[23]) still exceed the value predicted by Marcus theory, but go below the values estimated with inner-sphere electron transfer as attributed to adventitious surface contamination in the supporting information.

5.3.2 Preliminary Dopamine Volumetric Measurement

Preliminarily, we tested double-CF UMEs to detect 50 and 100 μM DA in Tris buffer at pH 7.4 that mimics a cerebellum fluid (Supporting Information). Collector responses at 0.1 V/s were similar to generator responses (Figure 5-5 A), where the large background was subtracted for the latters to yield high collection efficiencies of 0.87 ± 0.03 at forward peak potentials using four electrodes (Figure 5-14). This result indicates that dopamine-*o*-quinone (DOQ) was oxidatively generated from DA at the generator electrode and was reduced to DA at the collector electrode to efficiently complete quasi-steady-state redox cycling. Noticeably, generator and collector responses were lower during the reverse scan than the forward scan. This hysteresis, however, was not due to electrode fouling. Both generator and collector responses during the forward scan of the next cycle were recovered (red and green lines in Figure 5-5 A) to continuously yield nearly identical voltammograms. We estimate quantitatively that the cyclization of DOQ (Figure 5-15) is too slow[24] to produce leucodopaminochrome as the precursor of a blocking polymer film[25] before DOQ is transported far away from the generator electrode or reduced at the collector electrode (Supporting Information).

DA was detectable also at 100 V/s (Figure 5-5 B) to complete redox cycling based on DA oxidation at the generator electrode and DOQ reduction at the collector electrode. DA molecules

adsorbed on the CF surface were oxidized at the generator electrode to yield an enhanced peak-shaped response, which was proportional to the scan rate.[26] The collector response maintained a sigmoidal shape, but also increased significantly in comparison with that at 0.1 V/s owing to the reduction of DOQ desorbed from the generator electrode. The collector response, however, was several times lower than the peak current response of the generator electrode, which suggests that only a small fraction of DOQ was desorbed from the generator electrode during the fast potential cycle. In fact, the time scale of DOQ desorption from the CF surface (sub-seconds[26]) is much slower than the time scale of the potential cycle (~30 ms) at 100 V/s. Noticeably, collector responses were distorted by capacitive coupling with generator responses as observed typically with nanogap-based electrochemical cells.[27] Most clearly, the peak-shaped generator response based on the oxidation of adsorbed DA was coupled with a peak-shaped collector response at 0.45 V. Moreover, a non-zero background collector response with a spike at 1.0 V was coupled with a capacitive background response of the generator electrode. Importantly, the reduction of DOQ at the collector electrode dominated a sigmoidal collector response, which was not observed when the collector potential was too positive to reduce DOQ (Figure 5-18).

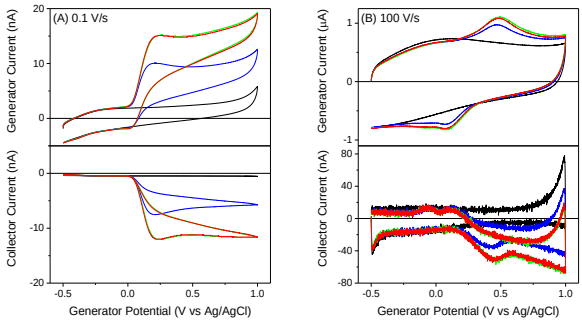

Figure 5-5 Generator and collector current responses of double-CF UMEs at (A) 0.1 and (B) 100 V/s in Tris buffer containing 0 (black), 50 (blue), and 100 (red and green for first and second cycles, respectively) μM DA. Collector potential at –0.3 V.

5.3.3 Dopamine with Ascorbic Acid

We investigated generator and collector responses with DA in the presence of AA (Figure 5-6), which is co-existent with DA in vivo and is oxidized as readily as DA.[14] We employed nanogap voltammetry at 0.1 V/s (bottom panel of Figure 5-6 A) to obtain low collection efficiencies of 0.02 ± 0.01 for 500 μM AA at the switching potential using seven electrodes. In fact, the collector response was largely increased by the addition of 100 μM DA. By contrast, the generator response was much higher for AA and was only slightly increased by the addition of 100 μM DA (top panel of Figure 5-6 A). The collection efficiency of AA is low, because the oxidative product of AA, i.e., dehydroascorbic acid, is irreversibly and immediately hydrolyzed to a redox-inactive species.[28] More quantitatively, a low collection efficiency of 0.02 for 500 μM AA yields 10 μM of dehyroascorbic acid at the collector electrode and corresponds to a high first-order rate constant of 1.2×10^5 s^{-1} for the irreversible hydrolysis of dehyroascorbic acid (Figure 5-16). Interestingly, a short-lived product was barely detectable at the collector electrode owing to the narrow gap. We estimate that a wider gap of ~0.3 μm will lower the collection efficiency of AA to 0.0001 to nearly eliminate the contribution of AA to the collector response (Supporting Information). Importantly, narrow gaps with widths of either 0.18 or 0.3 μm prevent the relatively fast reduction of DOQ by AA[29] (Figure 5-17) to yield a high collection efficiency for DA in the presence of AA (Supporting Information).

We were able to obtain a higher collector response to 100 μM DA than 500 μM AA even at 100 V/s, which is 1000 times faster than employed in the previous study of DA detection in the presence of AA with a nanogap cell.[7] Quantitatively, a collector response with 500 μM AA was ~10 nA with respect to the background at >0.5 V during the forward scan and was much smaller than the corresponding change of ~80 nA in the collector response by the addition of 100 μM DA

(bottom panel of Figure 5-6 B). The collector response with DA and AA yielded peaks capacitively coupled with generator responses to AA at 0.25 V during the forward scan as well as DA at 0.55 V and 0.25 V during forward and reverse scans, respectively (top panel of Figure 5-6 B). Noticeably, sigmoidal generator (0.1 V/s) and collector (0.1 and 100 V/s) responses shifted to more positive potentials in the presence of AA (compare Figure 5-6 with Figure 5-5), which slowed DA oxidation at the generator electrode. Moreover, AA exerted a thermodynamic effect to shift the entire generator voltammogram at 100 V/s to slightly more positive potentials than without AA. These kinetic and thermodynamic effects did not affect the diffusion-limited current of the collector electrode at the generator potential of >0.5 V as a measure of DA concentration.

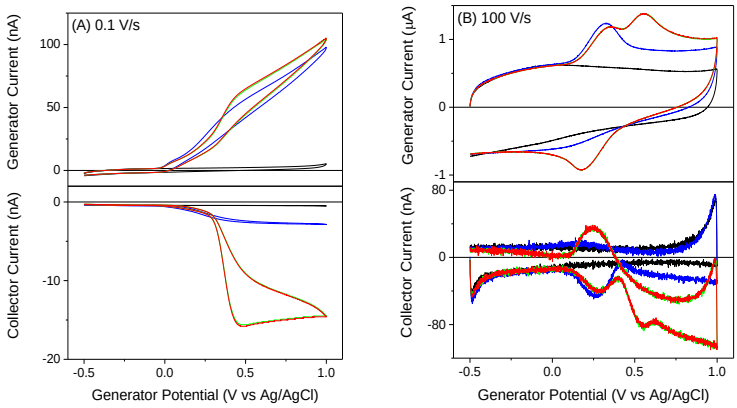

Figure 5-6 Generator and collector current responses of double-CF UMEs at (A) 0.1 and (B) 100 V/s in Tris buffer containing 500 µM AA with (red and green for first and second cycles, respectively) and without (blue) 100 µM DA. Black lines represent background responses in the buffer. Collector potential at –0.3 V.

5.4 Conclusions

In summary, we demonstrated the simple fabrication of double-CF UMEs with nanogaps and their application for quasi-steady-state nanogap voltammetry at high scan rates with the suppressed background. Reproducible gap widths of 0.18 ± 0.03 μm were obtainable without the use of extensive nanolithography[5,10] or nanoscale SECM[11,12] as determined from nanogap voltammograms. The fastest scan rate of 100 V/s in this study far exceeded scan rates of ≤0.1 V/s employed previously for nanogap-based voltammetry[2,3] including the selective detection of DA in the presence of AA.[7] The probe-type design of double-CF UMEs as well as their high DA selectivity against AA is attractive for in-vivo applications, where a wider gap will be useful not only to further reduce AA interference and possibly capacitive coupling, but also to maintain a nanogap without CF–CF contact. Such applications, however, will require us to better understand and optimize the surface-dependent electrochemistry of DA[30] at double-CF UMEs exposed to ion and electron beams as well as to develop a faster bipotentiostat for potential scans at ≥400 V/s as practiced for fast-scan cyclic voltammetry.[14] More generally, the simple fabrication of double-CF UMEs will promote the exploration and application of nanogap-based electrochemical measurements to complement approaches based on nanolithography[5,10] and nanoscale SECM,[11,12] where fast-scan nanogap voltammetry will be also applicable.

5.5 Supporting Information

5.5.1 Chemicals

$Ru(NH_3)_6Cl_3$ was obtained from Strem Chemicals (Newburyport, MA). L-ascorbic acid (AA), dopamine (DA) hydrochloride, 2-amino-2-(hydroxymethyl)-1,3-propanediol (Tris) hydrochloride were purchased from Sigma Aldrich (St. Louis, MO). Milli-Q Advantage A10 water purification system (EMD Millipore, Billerica, MA) was used to obtain UV-treated deionized ultrapure water (18.2 MΩ·cm) with a total organic carbon (TOC) value of 2–3 ppb as measured by using an internal online TOC monitor. The Milli-Q system was fed with the water (15.0 MΩ·cm) purified from tap water by using Elix 3 Advantage (EMD Millipore). DD and AA were dissolved in Tris buffer similar to cerebellum fluids containing 15 mM Tris hydrochloride, 140 mM NaCl, 3.25 mM KCl, 1.2 mM $CaCl_2$, 1.25 mM NaH_2PO_4, 1.2 mM $MgCl_2$ and 2.0 mM Na_2SO_4 at pH 7.4.[31] Sample solutions were freshly prepared just before electrochemical experiments and were used without removing the residual oxygen. A voltammetric response to oxygen was negligible in comparison with that to 10 mM $Ru(NH_3)_6Cl_3$ in 1 M KCl. No significant change in DA and AA responses was observed when the solution was purged with nitrogen.

5.5.2 Fabrication of Double-CF UMEs

Double-CF UMEs were fabricated using 7 μm-diameter CF from Goodfellow (C00572, Coraopolis, PA) or Cytec (T650, Piedmont, SC) for studies of $Ru(NH_3)_6^{3+}$ or DA, respectively. Specifically, an in-house vacuum was used[32] to pull a CF into each channel of a double-bore borosilicate capillary (MBT-015-062-2P with bore diameter of 0.015" and outer diameter of

0.062", Friedrich and Diammock, Millville, NJ). The CF-capillary composite was pulled using a pipet puller with a heating coil (PC-10, Narishige, Amityville, NY) to yield a pair of pulled capillaries with protruded CFs. CFs were cut in the middle by sharp scissors or nippers (Fine Science Tools, Foster City, CA), milled by focused ion beam (FIB) technology with a dual beam FIB/SEM instrument (Scios, FEI, Hillsboro, OR), and imaged by SEM of the dual beam instrument. Figures 5-7 A and 5-7 B show SEM images of double-CF UMEs before and after FIB milling, which was used only to shorten the CFs. We also prepared double-CF UMEs using double-bore capillaries with a wider bore–bore separation (MBT-010-062-2P with bore diameter of 0.010" and outer diameter of 0.062", Friedrich and Diammock) to yield submicrometer-wide gaps (~0.8 µm in Figures 5-7 C and 5-7 D). Double-CF UMEs were cleaned for 20 minutes in isopropyl alcohol purified by activated carbon[33] (Norit SA 2, Thermo Fisher Scientific, Waltham, MA) and were used for a series of electrochemical experiments.

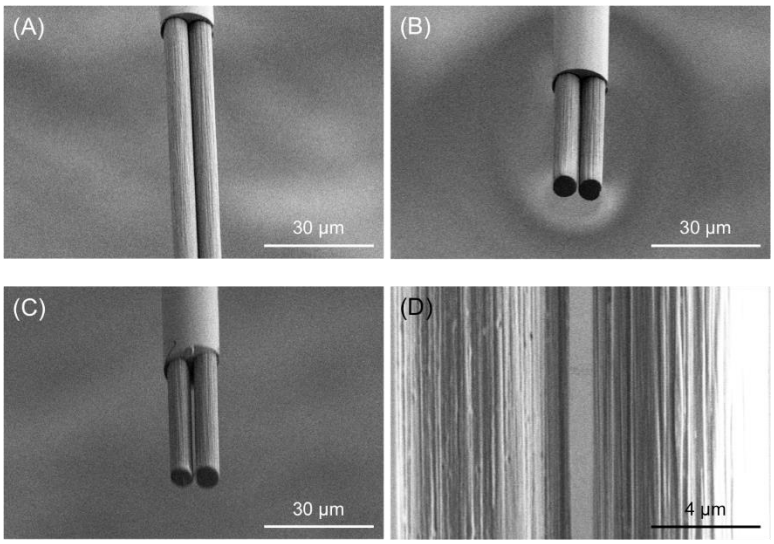

Figure 5-7 SEM images of double-CF UMEs with a ~0.18 µm-wide gap (A) before and (B) after FIB milling or (C) and (D) double-CF UMEs with a ~0.8 µm-wide gap.

5.5.3 Bipotentiostat Modification

A commercial bipotentiostat (CHI 802D, CH Instruments, Austin TX) that was previously modified to eliminate possible causes of damage of sub-micrometer-sized Pt UMEs[34,35] was further modified in this study to enable nanogap voltammetry at scan rates of up to 100 V/s. Specifically, the circuit board was modified to control the generator potential through a fast parallel digital-to-analogue converter (DAC). The generator electrode was connected to the bipotentiostat as the secondary working electrode to cycle its potential against a reference electrode.[36] A slow serial DAC was used to control the potential of the collector electrode, which was virtually grounded as the primary working electrode and biased at a constant potential against the reference electrode.[36] Software and firmware were also modified accordingly. It should be noted that the modified bipotentiostat was used to check by nanogap voltammetry in the background solution whether the generator electrode of double-CF UMEs contacts the collector electrode. Double-CF UMEs with contact yielded a current flow between generator and collector electrodes (Figure 5-8).

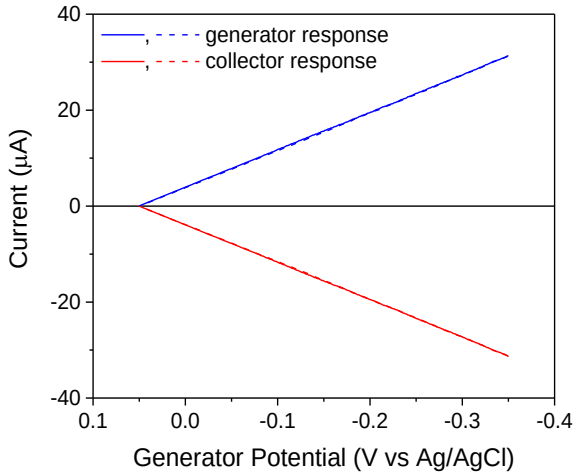

Figure 5-8 Current responses of contacted generator (blue) and collector (red) electrodes in 1 M KCl at 0.02 V/s. Solid and dashed lines represent forward and reverse scans, respectively. The collector potential was set at –0.05 V.

5.5.4 Finite Element Analysis

We employed a 2D model of double-cylinder UMEs reported in the previous study[37] to fit experimental voltammograms (Figures 5-4, 5-9 A, and 5-9 B) as well as to ensure that these voltammograms were kinetically limited to deviate from reversible voltammograms (Figure 5-9 C). We employed Multiphysics 5.3a (COMSOL, Burlington, MA) to perform the finite element simulation. A fit between experimental and simulated generator responses was compromised at a higher scan rate, where the subtraction of a higher background response was required (Figure 5-10).

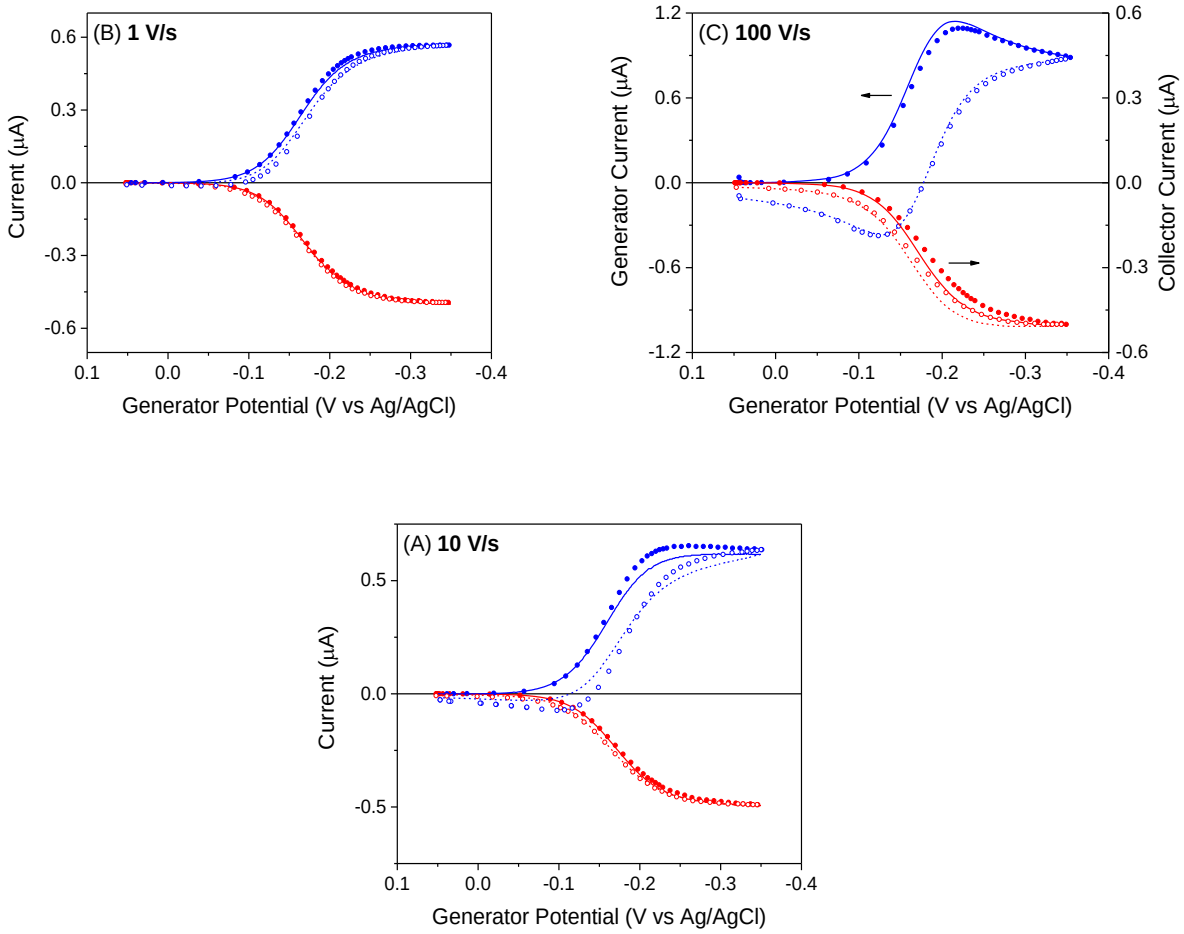

Figure 5-9 Experimental (lines) and simulated (circles) current responses of generator (blue) and collector (red) electrodes in 10 mM $Ru(NH_3)_6^{3+}$ and 1 M KCl at (A) 10 and (B) 1 V/s. Experimental generator responses are background-subtracted. (C) Generator (blue) and collector (red) responses simulated for quasi-reversible (circles) and reversible (lines) ET reactions at 100 V/s. Simulation employed parameters used in Figure 5-4 with the exception of k^0 = 10 cm/s for the reversible case. Solid lines and closed circles represent forward scans. Dashed lines and open circles correspond to reverse scans. The collector potential was set at 0.05 V.

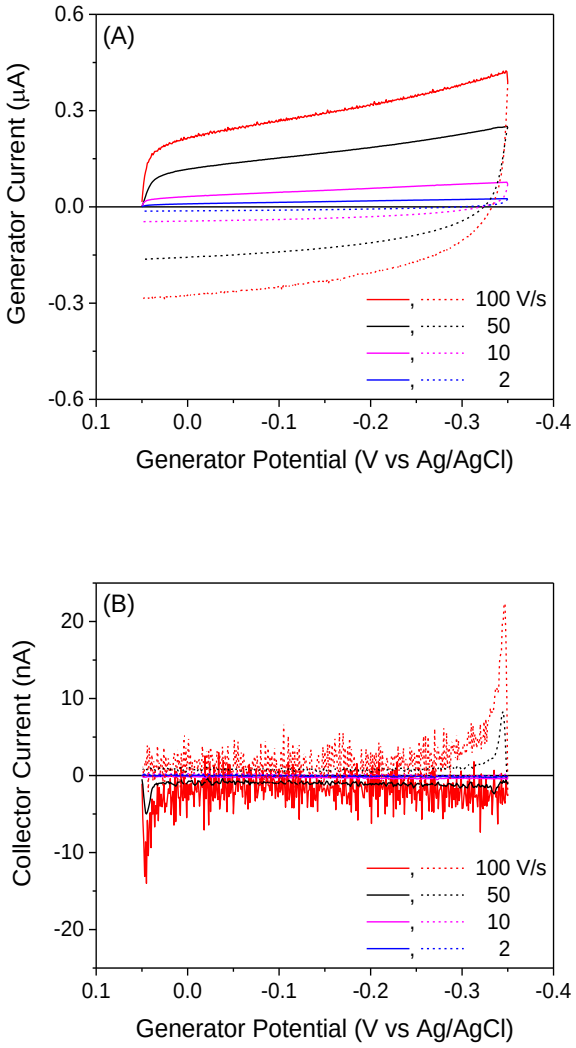

Figure 5-10 (A) Generator and (B) collector responses of double-CF UMEs at 2–100 V/s in 1 M KCl. Solid and dotted lines represent forward and reverse scans, respectively. The collector potential was set at 0.05 V.

It should be noted that the k^0 value was determined more reliably by nanogap voltammetry than by generator voltammetry, not only because the former was obtained under higher mass-transport conditions than the latter at 100 V/s to better resolve a kinetic effect (Figure 5-9 C), but also because the former fitted with simulated voltammograms better (Figure 5-4 A) with smaller contributions from the background response and the current response at the tip end of a CF, which was neglected in the 2D model[37] and was quantified in the 3D model (Figure 5-12; see below).

We extended the finite element simulation to predict that the gap of the double-CF UMEs developed in this study is narrow enough to establish quasi-steady-state redox cycling even at 1000 V/s (Figure 5-11). For this simulation, gap width, CF length, and k^0 were determined from nanogap voltammograms at 100 V/s (Figure 5-4 A). A higher scan rate of 1000 V/s only slightly lowered the collector response and increased its hysteresis (bottom panel of Figure 5-11). This result indicates that a quasi-steady state was achieved ~1000 times faster at the collector electrode (1000 V/s) than at the generator electrode (1 V/s; see Figure 5-10 A), where a transient current at the side of generator electrode far from the nanogap decayed slowly.[37] In fact, transient features of generator response were enhanced at 1000 V/s to yield a higher current response and sharper voltammetric peaks (top panel of Figure 5-11). Specifically, the forward peak current increased from 1.0 μA at 100 V/s to 2.6 μA at 1000 V/s, where the enhancement factor of 2.6 was less than expected from a square-root dependence on scan rate, because of the slightly quasi-steady-state character of the generator response at 100 V/s (Figure 5-4 A).[38] Moreover, the enhanced forward peak current is only comparable to a background current, which is expected to linearly vary with the scan rate[39] by a factor of 10 from ~0.3 μA at 100 V/s (Figure 5-10 A) to ~3 μA at 1000 V/s. By contrast, the capacitive background current at the collector electrode was smaller than a noise level of a few nA at 100 V/s (Figure 5-10 B) and should be still much lower at 1000 V/s than the corresponding limiting current of ~0.4 μA.

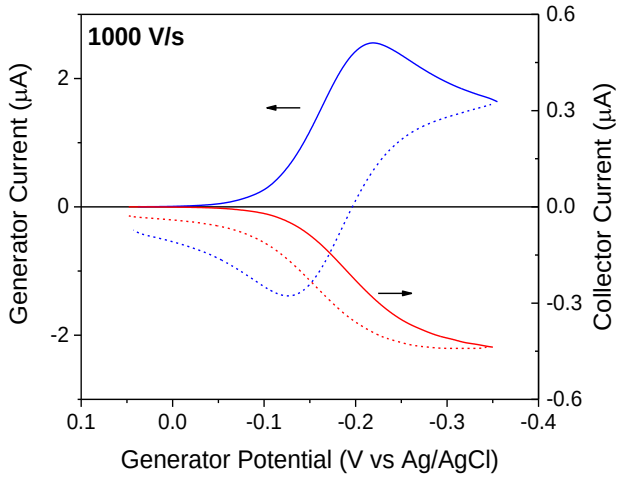

Figure 5-11 Simulated responses of generator (blue) and collector (red) electrodes in 10 mM $Ru(NH_3)_6^{3+}$ and 1 M KCl at 1000 V/s. Simulation employed the parameters determined in part A of Figure 5-4. Solid and dashed lines represent forward and reverse scans, respectively.

5.5.5 3D Simulation

A 2D model of double-cylinder UMEs reported in the previous study[37] was extended to a 3D model by COMSOL Multiphysics (Figure 5-12) to find a small difference in the generator response to $Ru(NH_3)_6^{3+}$ and a negligible difference in the collector response to $Ru(NH_3)_6^{2+}$ between 2D and 3D simulations (Figure 5-13). These results indicate a small contribution of the tip end of generator electrode to its current response as well as negligible redox cycling between tip ends of generator and collector electrodes, which was neglected in the 2D model[7] and was quantified in the 3D model (Figure 5-13). In addition, 3D simulation was performed to calculate the current response of single-CF UMEs (Figure 5-13) by removing the collector electrode from the system (Figure 5-12).

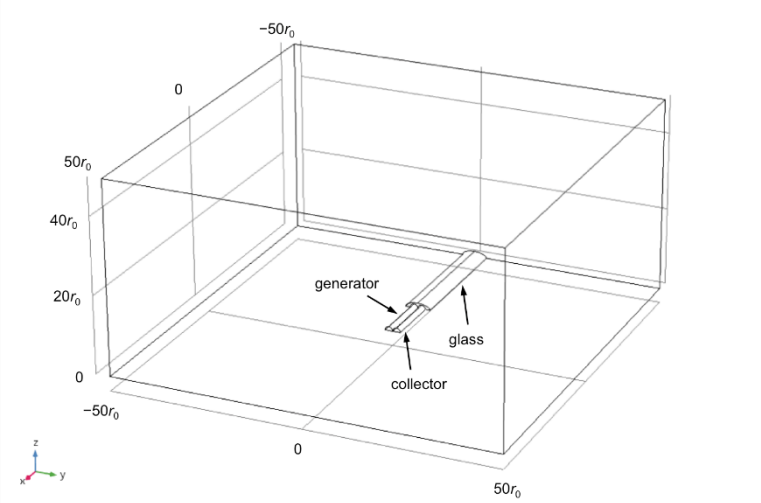

Figure 5- 12 3D geometry of double-CF UMEs simulated for nanogap voltammetry. The CF radius is given by r_0.

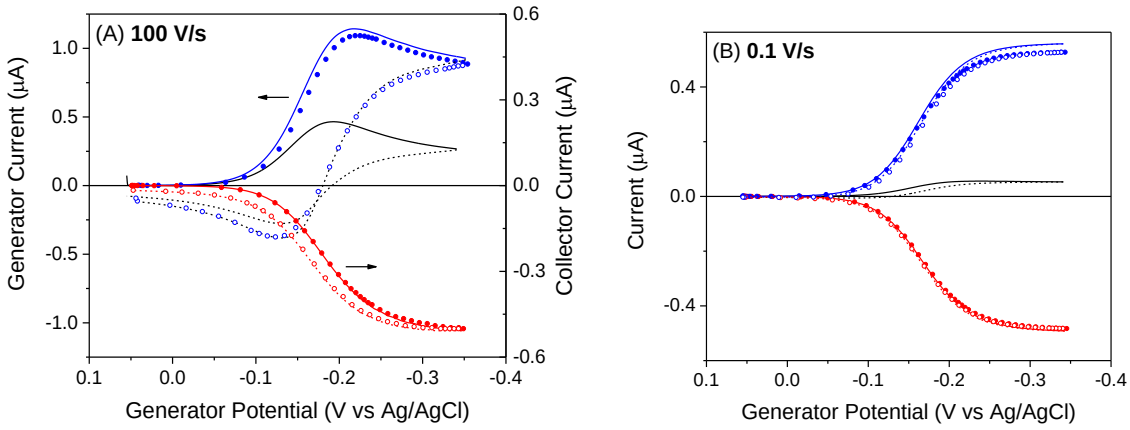

Figure 5-13 Generator (blue) and collector (red) responses based on 2D (circles) and 3D (lines) simulations at (A) 100 and (B) 0.1 V/s. Parameters for the respective scan rates are identical to those used in parts A and B of Figure 5-4. Solid and dashed lines are forward and reverse scans, respectively. Closed and open circles are forward and reverse responses, respectively. Black lines are responses of the corresponding single CF electrode without a collector electrode.

In both 2D and 3D simulations, the solution initially contained a redox species, O (= $Ru(NH_3)_6^{3+}$), which participated in a one-electron transfer reaction as given by

$$O + e \rightleftharpoons R \quad \text{(S-1)}$$

Diffusional mass transport of the reactant was represented by

$$\frac{\partial c_O}{\partial t} = D\left(\frac{\partial^2 c_O}{\partial x^2} + \frac{\partial^2 c_O}{\partial y^2} + \frac{\partial^2 c_O}{\partial z^2}\right) \quad \text{(S-2)}$$

where c_O is the local concentration of the reactant at (x, y, z) in solution. We assumed the identical diffusion coefficient, D, for species O and R so that the diffusion problem needs to be solved only for the reactant. The reactant was voltammetrically electrolyzed at the generator electrode to yield the boundary condition based on the Butler–Volmer kinetics[40]

$$D\left(\frac{\partial c_O}{\partial \boldsymbol{n}}\right) = -v_{et} \quad \text{(S-3)}$$

with

$$v_{et} = k^0\left\{c_O \exp\left[-\frac{\alpha F\left(E_g - E^{0'}\right)}{RT}\right] - \left(c_0 - c_O\right)\exp\left[\frac{\left(1-\alpha\right)F\left(E_g - E^{0'}\right)}{RT}\right]\right\} \quad \text{(S-4)}$$

where $\boldsymbol{n}$ is a unit vector normal to the surface of the generator electrode at the point of interest, v_{et} is the heterogeneous ET rate, k^0 is the heterogeneous standard ET rate constant, α is transfer coefficient, E_g is the potential of the generator electrode, $E^{0'}$ is the formal potential of the redox couple, and c_0 is the bulk concentration of the reactant, O. The boundary condition for the diffusion-limited regeneration of the reactant at the collector electrode was given by

$$c_O = c_0 \quad \text{(S-5)}$$

where the potential of the collector electrode, E_c, is positive enough with respect to $E^{0'}$. Other boundary conditions are identical to those of 2D simulation.[37]

5.5.6 Collection Efficiency of DA

We estimated collection efficiency of DA at 0.1 V/s, where the background generator response was small enough for good subtraction. Peak current responses of generator and collector electrodes with 50 μM DA at 0.2 V were used to calculate collection efficiencies after the background was subtracted from the generator response (Figure 5-14). The background of collector electrode was negligibly small and was not subtracted from the collector response.

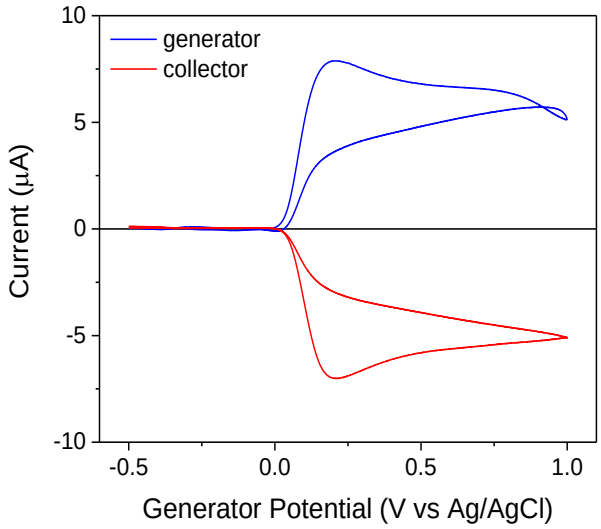

Figure 5-14 Background-subtracted generator response to 50 μM DA at 0.1 V/s as obtained from the corresponding generator voltammograms in Figure 5-5 A. The collector response is not background-subtracted and is identical to that in Figure 5-5 A.

5.5.7 Effect of Following Chemical Reaction on Collector Efficiency

We adapted the theory of nanogap measurement based on scanning electrochemical microscopy[41] to approximately estimate collection efficiencies when an ET reaction at the generator electrode is followed by a chemical reaction in solution. In this estimation, an effective

first-order rate constant, k, was given for the following chemical reaction to yield the concentration of the product of the ET reaction, $c(t)$, at a time, t, and at a diffusion distance, d, from the generator electrode as

$$c(t) = c_g \exp(- kt) \quad \text{(S-6)}$$

with

$$d = \sqrt{2Dt} \quad \text{(S-7)}$$

where c_g is the concentration of the product of the ET reaction at the surface of the generator electrode and D (= ~5 × 10^{-6} cm^2/s) is the diffusion coefficient of the product in solution. A combination of eq 5-12 with eq 5-13 gave a collection efficiency, i.e., $c(t)/c_g$, as

$$\frac{c(t)}{c_g} = \exp\left(- \frac{kd^2}{2D} \right) \quad \text{(S-8)}$$

Eq S-8 is used to estimate collection efficiencies for three cases discussed in the main text.

Cyclization of Dopamine-*o*-Quinone (DOQ). The oxidation of DA at the generator electrode produces DOQ, which can be cyclized to leucodopaminochrome (Figure 5-15) as a precursor of a polymer film to significantly inhibit the surface-dependent redox chemistry of DA.[42] This cyclization reaction, however, is slow as characterized by a low first-order rate constant of 0.147 s^{-1},[43] which yields a collection efficiency of 0.9999955 for a gap width of d = 0.18 μm in eq S-8. Moreover, the cyclization of 1% DOQ to leucodopaminochrome, i.e., $c(t)/c_g$ = 0.99 in eq S-8, yields d = 8.3 μm, which is comparable to the diameter of CF (~7 μm). These results ensure that most DOQ molecules diffuse away from the generator electrode or reach the collector electrode for reduction to DA before cyclization occurs to initiate the formation of an insulating film.

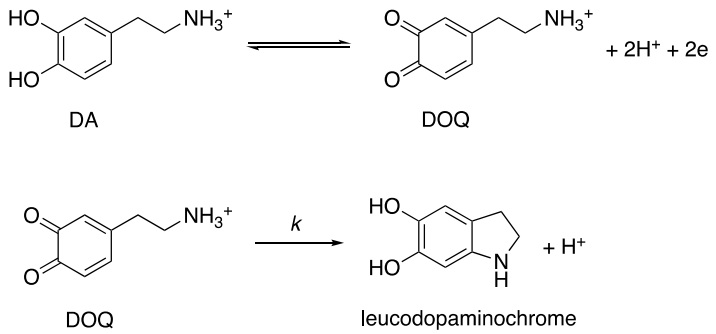

Figure 5-15 Oxidation of DA (top) and cyclization of DOQ (bottom).[42]

Hydration of Dehydroascorbic Acid. The oxidation of AA at the generator electrode produces dehydroascorbic acid, which is quickly hydrolyzed to a redox-inactive product (Figure 5-16).[44,45] In this study, a low collection efficiency of 0.02 was observed experimentally to yield $k = 1.2 \times 10^5$ s^{-1} from eq S-8 with $d = 0.18$ µm. This rate constant is much higher than a k value of 1.3×10^3 s^{-1} at hanging mercury drop electrodes[46] and is comparable to or lower than estimated for a pair of gold electrodes with a 50 nm-wide gap, where no collector response was observed when AA was oxidized at the generator electrode.[47] We used eq S-8 also to predict that a gap width of ~0.3 µm will reduce collection efficiency of AA to 0.0001. With this collection efficiency, 500 µM dehydroascorbic acid produced at the generator electrode yields 50 nM dehydroascorbic acid at the collector electrode to largely eliminate the interference by dehydroascorbic acid.

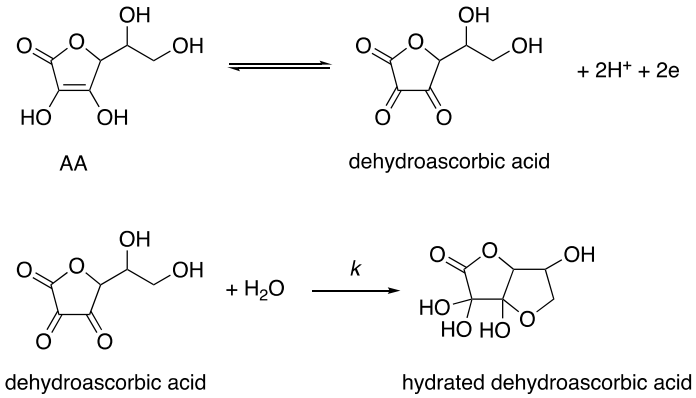

Figure 5-16 Oxidation of AA (top) and hydration of dehydroascorbic acid (bottom).[44,45]

Reduction of DOQ by AA. The oxidation of DA at the generator electrode produces DOQ, which can be reduced to DA by AA[48] (Figure 5-17) to lower the collection efficiency of DA and, subsequently, the collector response to DOQ. We assume a constant concentration of 500 μM AA to yield an effective first-order rate constant, k, of 7.5×10^2 s^{-1} for the bimolecular reaction with a second-order rate constant of 1.5×10^6 $M^{-1} \cdot s^{-1}$.[48] The resultant collection efficiencies of DA with d = 0.18 and 0.30 μm in eq S-8 are 0.98 and 0.94, respectively, thereby indicating a very small loss of DA sensitivity at the collector electrode. Moreover, dehydroascorbic acid thus produced is immediately and irreversible hydrolyzed to give a negligible contribution to the collector response.

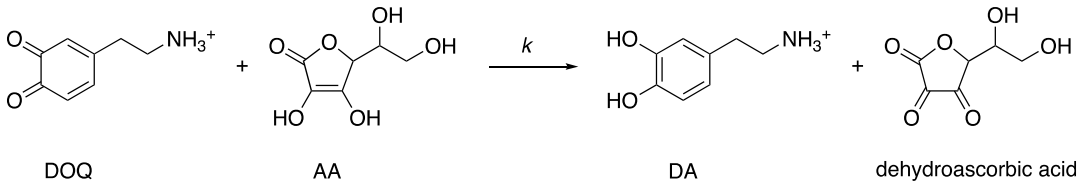

Figure 5-17 Reduction of DOQ by AA.[48]

5.5.8 Effect of Collector Potential on Collector Response with DA

We varied the collector potential to ensure that the reduction of DOQ at the collector electrode contributes to the sigmoidal collector response, which was observed only when the collector potential was negative enough to reduce DOQ (i.e., –0.3 V; see blue line in the bottom panel of Figure 5-18). The collector response was controlled purely by capacitive coupling with the generator response when the collector potential was too positive to reduce DOQ (i.e., 0.25 V; red line in the bottom panel of Figure 5-18). The collector response at the positive collector potential was very similar to the background collector response without DA (black line in the

bottom panel of Figure 5-18). The collector potential did not affect the generator response to DA adsorbed on the CF surface (the top panel of Figure 5-18).

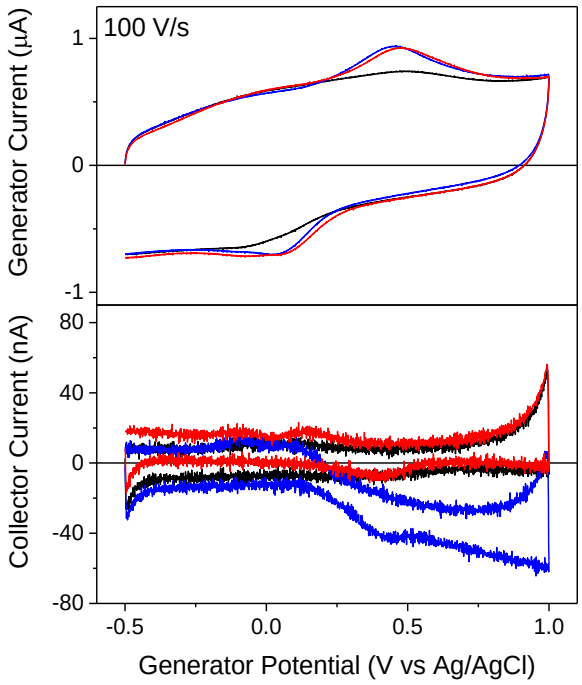

Figure 5-18 Generator and collector responses of double-CF UMEs in Tris buffer containing 100 μM DA at 100 V/s when the collector potential was set at –0.3 (blue) or 0.25 V (red). Black lines are background voltammograms in Tris buffer at the collector potential of 0.25 V.

5.5.9 Outer-Sphere and Inner-Sphere Electron Transfer (ET) of RuHex$(NH_3)_6^{3+}$

We develop a model based on outer-sphere and inner-sphere ET pathways of the $Ru(NH_6)_3^{3+/2+}$ couple (Figure 5-19) to quantitatively support our hypothesis[49] that the ET reaction of this redox couple is mediated through both pathways to exceed a rate predicted by Marcus theory for adiabatic outer-sphere ET. This model demonstrates that the overall standard ET rate

constant, k^0, can be dependent on standard rate constants of outer-sphere and inner-sphere pathways, k_{OS}^0 and k_{IS}^0, respectively, as given by (see below for derivation)

$$k^0 = \frac{1}{1+bc_0}\left(k_{OS}^0 + k_{IS}^0 \Gamma_s b\right) \quad \text{(S-9)}$$

where c_0 is the bulk concentration of $Ru(NH_6)_3^{3+}$ and we assume for simplicity that the diffusion-limited adsorption of $Ru(NH_6)_3^{3+}$ and $Ru(NH_6)_3^{2+}$ at the electrode surface follows the same Langmuir isotherm with identical saturated surface concentration, Γ_s, and equilibrium constant, β, for both species. Under these conditions, the heterogeneous self-exchange reaction is negligible (see below).[50,51]

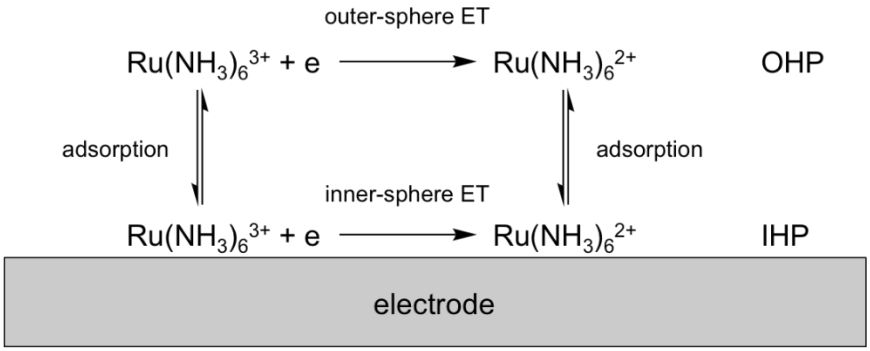

Figure 5-19 Outer-sphere and inner-sphere ET of the $Ru(NH_6)_3^{3+/2+}$ couple at outer and inner Helmholtz planes (OHP and IHP), respectively.[52]

Specifically, we used eq S-9 with c_0 = 0.1–10 mM for $Ru(NH_6)_3^{3+}$ in addition to other parameter values (see below) to estimate k^0 = 30–46 cm/s, which are higher than the value predicted by Marcus theory[53] and are consistent with k^0 values determined by using nanoelectrochemical approaches in extremely pure water with low TOC, i.e., ≥10 cm/s (diffusion limit) at CVD-based carbon nanoelectrodes,[54] ≥6.9 cm/s (diffusion limit) at electron-beam-deposited carbon electrodes,[49] and 36 cm/s at single Pt nanoparticles.[55] Without the use of low-

TOC water, k^0 values at nanoelectrodes are still higher than the value predicted by Marcus theory,[53] but are lowered by adventitious surface contamination[56] to go below the value predicted by eq S-9, i.e., 17.0 ± 0.9 cm/s at Pt nanoelectrodes,[57] 13.5 ± 2 cm/s at Au nanoelectrodes,[58] 10 ± 5 cm/s at metallic single-walled carbon nanotubes.[59] A high k^0 value of 79 ± 44 cm/s that was determined without the use of low-TOC water was overestimated by using recessed Pt nanoelectrodes,[60] which is attributed to damage by electrostatic discharge.[61]

In eq S-9, a theoretical k_{OS}^0 value of 2.2 cm/s for adiabatic outer-sphere ET[53] was used in addition to other parameters reported for Au surfaces to emphasize that the adsorption of a small amount of the $Ru(NH_6)_3^{3+/2+}$ couple results in a large kinetic contribution of the inner-sphere pathway owing to its fast kinetics. For Au surfaces, a contribution of the inner sphere pathway is estimated to $k_{\mathrm{IS}}^0 \Gamma_s \beta / (1 + \beta c_0)$ = 44 and 28 cm/s with c_0 = 0.1 and 10 mM, respectively, by using β = 5.39 × 10^4 cm^3/mol[62] in addition to $k_{\mathrm{IS}}^0 = 5.4 \times 10^6$ k_{IS}^0 = 5.4 × 10^6 s^{-1} and Γ_s = 1.5 × 10^{-10} mol/cm^2 measured for the mixed self-assembled monolayer of $HS(CH_2)_3$(pyridine)$Ru(NH_3)_5^{3+}$.[63] In comparison, a contribution of the outer-sphere pathway is much smaller, i.e., $k_{\mathrm{OS}}^0 / (1 + \beta c_0)$ = 1.6 and 2.5 cm/s for c_0 = 10 and 0.1 mM, respectively. The kinetics of the inner-sphere pathway is extremely fast owing to the large k_{IS}^0 value, whereas the adsorption of the $Ru(NH_6)_3^{3+/2+}$ couple on a Au surface is relatively weak to yield total surface concentrations, $\Gamma_{Ru(NH_3)_6^{3+}} + \Gamma_{Ru(NH_3)_6^{2+}}$, of 8.0 × 10^{-13} and 5.3 × 10^{-11} mol/cm^2 with c_0 = 0.1 and 10 mM, respectively, which correspond to the respective surface coverage of 0.0053 and 0.35 (see eq S-24 below). It should be noted that the inner-sphere pathway requires the adsorption of both $Ru(NH_6)_3^{3+}$ and $Ru(NH_6)_3^{2+}$ at the IHP, which is the case for Au[62] and Pt[64] electrodes.

We derived eq S-9 by considering that the actual ET rate, v, is the sum of the rates of inner-sphere and outer-sphere pathways, v_{OS} and v_{IS}, respectively, i.e.,

$$v = v_{OS} + v_{IS} \quad \text{(S-10)}$$

In our model, an outer-sphere ET reaction occurs over the bare surface of electrode uncovered by the adsorbed $Ru(NH_6)_3^{3+/2+}$ couple to yield a rate given by the Butler–Volmer model as[65-67]

$$v_{OS} = \left(1-\theta_O-\theta_R\right)\left(k_{OS}^{red}c_O - k_{OS}^{ox}c_R\right) \quad \text{(S-11)}$$

with

$$q_i = \frac{\Gamma_i}{\Gamma_{i,s}} \quad \text{(S-12)}$$

$$k_{OS}^{red} = k_{OS}^{0}\exp\left[-\frac{\alpha_{OS}F\left(E_S - E_{OS}^{0'}\right)}{RT}\right] \quad \text{(S-13)}$$

$$k_{OS}^{ox} = k_{OS}^{0}\exp\left[\frac{\left(1-\alpha_{OS}\right)F\left(E_S - E_{OS}^{0'}\right)}{RT}\right] \quad \text{(S-14)}$$

where c_i is the concentration of species i (= O or R) near the electrode surface, θ_i is the surface coverage by species i specifically adsorbed at the IHP, Γ_i is its surface concentration, $\Gamma_{i,s}$ is its saturated surface concentration, k_{OS}^{0} is the standard ET rate constant of the outer-sphere reaction, and α_{OS} and $E_{OS}^{0¢}$ are the corresponding transfer coefficient and formal potential, respectively. By contrast, the rate of inner-sphere ET is given by

$$v_{IS} = k_{IS}^{red}\Gamma_O - k_{IS}^{ox}\Gamma_R \quad \text{(S-15)}$$

with

$$k_{IS}^{red} = k_{IS}^{0} \exp\left[-\frac{a_{IS} F \left(E_S - E_{IS}^{0'} \right)}{RT} \right] \quad \text{(S-16)}$$

$$k_{IS}^{ox} = k_{IS}^{0} \exp\left[\frac{\left(1 - a_{IS}\right) F \left(E_S - E_{IS}^{0'} \right)}{RT} \right] \quad \text{(S-17)}$$

where k_{IS}^{0} is the standard ET rate constant of the inner-sphere pathway, and α_{IS} and $E_{IS}^{0¢}$ are the corresponding transfer coefficient and formal potential, respectively. In addition, we assume that the equilibrium, competitive adsorption of O and R follows Langmuir isotherms as given by[68]

$$\Gamma_O = \frac{b_O \Gamma_{O,s} c_O}{1 + b_O c_O + b_R c_R} \quad \text{(S-18)}$$

$$\Gamma_R = \frac{b_R \Gamma_{R,s} c_R}{1 + b_O c_O + b_R c_R} \quad \text{(S-19)}$$

where β_i is an equilibrium parameter. With eqs S-18 and S-19, $v_{OS} = v_{IS} = 0$ at equilibrium in eqs S-11 ($1 - \theta_O - \theta_R \le 0$) and S-15 yields[69]

$$E_{IS}^{0¢} = E_{OS}^{0¢} - \frac{RT}{F} \ln \frac{b_O \Gamma_{O,s}}{b_R \Gamma_{R,s}} \quad \text{(S-20)}$$

Moreover, we assume $\beta_O = \beta_R = \beta$, $\Gamma_{O,s} = \Gamma_{R,s} = \Gamma_s$, $c_O + c_R = c_0$ to simplify eqs S-18–S-20 to

$$\Gamma_O = \frac{b \Gamma_s c_O}{1 + b c_0} \quad \text{(S-21)}$$

$$\Gamma_R = \frac{b \Gamma_s c_R}{1 + b c_0} \quad \text{(S-22)}$$

$$E_{IS}^{0¢} = E_{OS}^{0¢} = E^{0¢} \quad \text{(S-23)}$$

A sum of eqs S-21 and S-22 yields

$$\frac{\Gamma_O + \Gamma_R}{\Gamma_s} = \theta_O + \theta_R = \frac{bc_0}{1 + bc_0} \quad \text{(S-24)}$$

which was used to estimate $\Gamma_{Ru(NH_3)_6^{3+}} + \Gamma_{Ru(NH_3)_6^{2+}}$ above. A combination of eq S-11 with eqs S-21 and S-22 gives

$$v_{OS} = \frac{1}{1 + \beta c_0}\left(k_{OS}^{red} c_O - k_{OS}^{ox} c_R\right) \quad \text{(S-25)}$$

Moreover, eq S-15 is combined with eqs S-21 and S-22 to yield

$$v_{IS} = \frac{\beta \Gamma_s}{1 + \beta c_0}\left(k_{IS}^{red} c_O - k_{IS}^{ox} c_R\right) \quad \text{(S-26)}$$

A combination of eq S-10 with eqs S-25 and S-26 gives

$$v = \frac{1}{1 + bc_0}\left[\left(k_{OS}^{red} + b\Gamma_s k_{IS}^{red}\right)c_O - \left(k_{OS}^{ox} + b\Gamma_s k_{IS}^{ox}\right)c_O\right] \quad \text{(S-27)}$$

Eq S-27 was combined with eqs S-13, S-14, S-16, and S-17 and simplified by using eq S-20 and $\alpha_{OS} = \alpha_{IS} = \alpha$ to yield

$$v = c_O k^0 \exp\left[-\frac{\alpha F\left(E_S - E^{0\prime}\right)}{RT}\right] - c_R k^0 \exp\left[\frac{(1-\alpha) F\left(E_S - E^{0\prime}\right)}{RT}\right] \quad \text{(S-28)}$$

where k^0 is given by eq S-9.

A few important features of eq S-9 are pointed out here. Eq S-9 indicates that outer-sphere and inner-sphere ET reactions are indistinguishable, i.e., the overall k^0 value is a convolution of k^0 values for outer-sphere and inner-sphere pathways, because adsorption equilibrium is established (eqs S-18 and S-19). This feature is consistent with previous theoretical assessments.[70,71] Moreover, both outer-sphere and inner-sphere ET reactions become slower with a higher bulk concentration of a reactant, c_0, which increases surface coverage. The slower outer-sphere ET

reaction with higher surface coverage is attributed to the lower fraction of the uncovered electrode surface (see eq S-11). The inner-sphere ET reaction becomes also slower with higher surface coverage, where the surface concentration of species i deviates more from proportionality with the bulk concentration (see eqs S-15, S-21, and S-22).

It should be noted that there is no need to consider a heterogeneous self-exchange reaction under the conditions of equilibrium adsorption as represented by eqs S-21 and S-22. The heterogeneous self-exchange reaction of a redox couple at IHP and OHP is described as[70]

$$\mathrm{O(IHP) + R(OHP) \underset{k_b^{ex}}{\overset{k_f^{ex}}{\rightleftharpoons}} R(IHP) + O(OHP)} \quad \text{(S-29)}$$

where k_f^{ex} and k_b^{ex} are forward and reverse rate constants, respectively, and are independent of the substrate potential. The rate of the heterogeneous self-exchange reaction, v_{ex}, is given by

$$v_{ex} = k_f^{ex}\Gamma_O c_R - k_b^{ex}\Gamma_R c_O \quad \text{(S-30)}$$

A combination of eq S-29 with eqs S-21 and S-22 yields

$$v_{ex} = \left(\frac{b\Gamma_s}{1+bc_0}\right)\left(k_f^{ex} - k_b^{ex}\right)c_R c_O \quad \text{(S-31)}$$

This reaction rate is zero at the equilibrium, which yields $k_f^{ex} = k_b^{ex}$. Thus, v_{ex} is always zero.[51]

5.6 Acknowledgements

This work was partially supported by the National Science Foundation (CHE 1608703) and the National Institutes of Health (R01 GM112656). We thank Prof. Adrian C. Michael and

Ms. Elaine M. Robbins for help on electrode fabrication and also Dr. Peixin He for the modification of bipotentiostat.

5.7 References

(1) Bard, A. J.; Fan, F.-R. F. *Acc. Chem. Res.* **1996**, *29*, 572–578.

(2) Amemiya, S.; Chen, R.; Nioradze, N.; Kim, J. *Acc. Chem. Res.* **2016**, *49*, 2007-2014.

(3) White, H. S.; McKelvey, K. *Curr. Opin. Electrochem.* **2018**, *7*, 48-53.

(4) Fan, F.-R. F.; Bard, A. J. *Science* **1995**, *267*, 871–874.

(5) Lemay, S. G.; Kang, S.; Mathwig, K.; Singh, P. S. *Acc. Chem. Res.* **2013**, *46*, 369-377.

(6) Wolfrum, B.; Zevenbergen, M.; Lemay, S. *Anal. Chem.* **2008**, *80*, 972-977.

(7) Ma, C.; Contento, N. M.; Gibson, L. R.; Bohn, P. W. *Anal. Chem.* **2013**, *85*, 9882-9888.

(8) Mirkin, M. V.; Bulhões, L. O. S.; Bard, A. J. *J. Am. Chem. Soc.* **1993**, *115*, 201-204.

(9) Nioradze, N.; Kim, J.; Amemiya, S. *Anal. Chem.* **2011**, *83*, 828-835.

(10) Wolfrum, B.; Kätelhön, E.; Yakushenko, A.; Krause, K. J.; Adly, N.; Hüske, M.; Rinklin, P. *Acc. Chem. Res.* **2016**, *49*, 2031-2040.

(11) Amemiya, S. Nanoscale Scanning Electrochemical Microscopy. In *Electroanalytical Chemistry*, Bard, A. J.; Zoski, C. G., Eds.; CRC Press, 2015, pp 1-72.

(12) Kai, T.; Zoski, C. G.; Bard, A. J. *Chem. Commun.* **2018**, *54*, 1934-1947.

(13) Pathirathna, P.; Balla, R. J.; Amemiya, S. *J. Electrochem. Soc.* **2018**, *165*, G3026-G3032.

(14) Rodeberg, N. T.; Sandberg, S. G.; Johnson, J. A.; Phillips, P. E. M.; Wightman, R. M. *ACS Chem. Neurosci.* **2017**, *8*, 221-234.

(15) Jaquins-Gerstl, A.; Michael, A. C. *Analyst* **2015**, *140*, 3696-3708.

(16) Seddon, B. J.; Wang, C. F.; Peng, W. F.; Zhang, X. J. *J. Chem. Soc. Faraday Trans.* **1994**, *90*, 605-608.

(17) Seddon, B. J.; Girault, H. H.; Eddowes, M. J.; Peng, W.; Zhao, Z. *J. Chem. Soc. Faraday Trans.* **1991**, *87*, 2603-2606.

(18) Baur, J. E.; Miller, H. M.; Ritchason, M. A. *Anal. Chim. Acta* **1999**, *397*, 123-133.

(19) Amatore, C.; Oleinick, A. I.; Svir, I. B. *J. Electroanal. Chem.* **2003**, *553*, 49-61.

(20) Hupp, J. T.; Liu, H. Y.; Farmer, J. K.; Gennett, T.; Weaver, M. J. *J. Electroanal. Chem. Interfacial Electrochem.* **1984**, *168*, 313-334.

(21) Morteza Najarian, A.; Chen, R.; Balla, R. J.; Amemiya, S.; McCreery, R. L. *Anal. Chem.* **2017**, *89*, 13532-13540.

(22) Kim, J.; Bard, A. J. *J. Am. Chem. Soc.* **2016**, *138*, 975-979.

(23) Güell, A. G.; Meadows, K. E.; Dudin, P. V.; Ebejer, N.; Macpherson, J. V.; Unwin, P. R. *Nano Lett.* **2014**, *14*, 220-224.

(24) Tse, D. C. S.; McCreery, R. L.; Adams, R. N. *J. Med. Chem.* **1976**, *19*, 37-40.

(25) Harreither, W.; Trouillon, R.; Poulin, P.; Neri, W.; Ewing, A. G.; Safina, G. *Anal. Chem.* **2013**, *85*, 7447-7453.

(26) Bath, B. D.; Michael, D. J.; Trafton, B. J.; Joseph, J. D.; Runnels, P. L.; Wightman, R. M. *Anal. Chem.* **2000**, *72*, 5994-6002.

(27) McKelvey, K.; Robinson, D. A.; Vitti, N. J.; Edwards, M. A.; White, H. S. *Faraday Discuss.* DOI: 10.1039/c8fd00014j.

(28) Compton, R. G.; Matysik, F.-M. *Electroanalysis* **1996**, *8*, 218-222.

(29) Sopchak, D.; Miller, B. *J. Phys. Chem. A* **2000**, *104*, 7545-7548.

(30) DuVall, S. H.; McCreery, R. L. *J. Am. Chem. Soc.* **2000**, *122*, 6759-6764.

(31) Zachek, M. K.; Hermans, A.; Wightman, R. M.; McCarty, G. S. *J. Electroanal. Chem.* **2008**, *614*, 113.

(32) Zhang, B.; Adams, K. L.; Luber, S. J.; Eves, D. J.; Heien, M. L.; Ewing, A. G. *Anal. Chem.* **2008**, *80*, 1394.

(33) Bath, B. D.; Michael, D. J.; Trafton, B. J.; Joseph, J. D.; Runnels, P. L.; Wightman, R. M. *Anal. Chem.* **2000**, *72*, 5994.

(34) Kim, J.; Renault, C.; Nioradze, N.; Arroyo-Curras, N.; Leonard, K. C.; Bard, A. J. *J. Am. Chem. Soc.* **2016**, *138*, 8560.

(35) Chen, R.; Balla, R. J.; Li, Z. T.; Liu, H. T.; Amemiya, S. *Anal. Chem.* **2016**, *88*, 8323.

(36) Bard, A. J.; Faulkner, L. R. *Electrochemical Methods: Fundamentals and Applications*; 2nd ed.; John Wiley & Sons: New York, 2001, p. 643.

(37) Pathirathna, P.; Balla, R. J.; Amemiya, S. *J. Electrochem. Soc.* **2018**, *165*, G3026.

(38) Bard, A. J.; Faulkner, L. R. *Electrochemical Methods: Fundamentals and Applications*; 2nd ed.; John Wiley & Sons: New York, 2001, p 232.

(39) Bard, A. J.; Faulkner, L. R. *Electrochemical Methods: Fundamentals and Applications*; 2nd ed.; John Wiley & Sons: New York, 2001, p. 16.

(40) Bard, A. J.; Faulkner, L. R. *Electrochemical Methods: Fundamentals and Applications*; 2nd ed.; John Wiley & Sons: New York, 2001, p. 94.

(41) Bi, S.; Liu, B.; Fan, F.-R. F.; Bard, A. J. *J. Am. Chem. Soc.* **2005**, *127*, 3690.

(42) Harreither, W.; Trouillon, R.; Poulin, P.; Neri, W.; Ewing, A. G.; Safina, G. *Anal. Chem.* **2013**,*85*, 7453.

(43) Tse, D. C. S.; McCreery, R. L.; Adams, R. N. *J. Med. Chem.* **1976**, *19*, 37.

(44) Compton, R. G.; Matysik, F.-M. *Electroanalysis* **1996**, *8*, 218.

(45) Karabinas, P.; Jannakoudakis, D. *J. Electroanal. Chem.* **1984**, *160*, 159.

(46) Perone, S. P.; Kretlow, W. J. *Anal. Chem.* **1966**, *38*, 1760.

(47) Wolfrum, B.; Zevenbergen, M.; Lemay, S. *Anal. Chem.* **2008**, *80*, 972.

(48) Sopchak, D.; Miller, B. *J. Phys. Chem. A* **2000**, *104*, 7545.

(49) Morteza Najarian, A.; Chen, R.; Balla, R. J.; Amemiya, S.; McCreery, R. L. *Anal. Chem.* **2017**, *89*, 13532.

(50) Laviron, E.; Roullier, L. *J. Electroanal. Chem.* **1998**, *443*, 195.

(51) Amemiya, S. *Anal. Chem.* **2017**, *89*, 7269.

(52) Klymenko, O. V.; Buriez, O.; Labbe, E.; Zhan, D. P.; Rondinini, S.; Tian, Z. Q.; Svir, I.; Amatore, C. *ChemElectroChem* **2014**, *1*, 227.

(53) Hupp, J. T.; Liu, H. Y.; Farmer, J. K.; Gennett, T.; Weaver, M. J. *J. Electroanal. Chem. Interfacial Electrochem.* **1984**, *168*, 313.

(54) Chen, R.; Hu, K.; Yu, Y.; Mirkin, M. V.; Amemiya, S. *J. Electrochem. Soc.* **2016**, *163*, H3032.

(55) Kim, J.; Bard, A. J. *J. Am. Chem. Soc.* **2016**, *138*, 975.

(56) Yu, Y.; Sun, T.; Mirkin, M. V. *Anal. Chem.* **2016**, *88*, 11758.

(57) Sun, P.; Mirkin, M. V. *Anal. Chem.* **2006**, *78*, 6526.

(58) Velmurugan, J.; Sun, P.; Mirkin, M. V. *J. Phys. Chem. C* **2008**, *113*, 459.

(59) Güell, A. G.; Meadows, K. E.; Dudin, P. V.; Ebejer, N.; Macpherson, J. V.; Unwin, P. R. *Nano Lett.* **2014**, *14*, 220.

(60) Penner, R. M.; Heben, M. J.; Longin, T. L.; Lewis, N. S. *Science* **1990**, *250*, 1118.

(61) Nioradze, N.; Chen, R.; Kim, J.; Shen, M.; Santhosh, P.; Amemiya, S. *Anal. Chem.* **2013**, *85*, 6198.

(62) Smalley, J. F.; Geng, L.; Chen, A.; Feldberg, S. W.; Lewis, N. S.; Cali, G. *J. Electroanal. Chem.* **2003**, *549*, 13.

(63) Smalley, J. F.; Finklea, H. O.; Chidsey, C. E. D.; Linford, M. R.; Creager, S. E.; Ferraris, J. P.; Chalfant, K.; Zawodzinsk, T.; Feldberg, S. W.; Newton, M. D. *J. Am. Chem. Soc.* **2003**, *125*, 2004.

(64) Aoki, K. J.; Chen, J.; Tang, P. *J. Phys. Chem. C* **2018**, *122*, 16727.

(65) Amatore, C.; Savéant, J. M.; Tessier, D. *J. Electroanal. Chem.* **1983**, *147*, 39.

(66) Sliusarenko, O.; Oleinick, A.; Svir, I.; Amatore, C. *ChemElectroChem* **2015**, *2*, 1279.

(67) Sliusarenko, O.; Oleinick, A.; Svir, I.; Amatore, C. *Electroanalysis* **2015**, *27*, 980.

(68) Bard, A. J.; Faulkner, L. R. *Electrochemical Methods: Fundamentals and Applications*; 2nd ed.; John Wiley & Sons: New York, 2001, p. 567.

(69) Bard, A. J.; Faulkner, L. R. *Electrochemical Methods: Fundamentals and Applications*; 2nd ed.; John Wiley & Sons: New York, 2001, p. 590.

(70) Laviron, E. Voltammetric Methods for the Study of Adsorbed Species. In *Electroanalytical Chemistry*; Bard, A. J., Ed.; Marcel Dekker: New York, 1982; Vol. 12, p 53.

(71) Klymenko, O. V.; Svir, I.; Amatore, C. *J. Electroanal. Chem.* **2013**, *688*, 320.